N° d'ordre NNT : 2022LYSEC019

**THESE de DOCTORAT DE L'UNIVERSITE DE LYON**
**opérée au sein de l'Ecole centrale de Lyon**

**Ecole Doctorale** N° 34
**Ecole doctorale Matériaux de Lyon**

**Spécialité de doctorat** :
**Discipline** : Matériaux

Soutenue publiquement le 12/05/2022, par :

**Thomas Dursap**

---

# GaAs nanowires: crystal phase engineering and application for water photoelectrolysis

---

Devant le jury composé de :

| | | |
|---|---|---|
| BAKKERS Erik | Professeur, TU/e Eindhoven | Rapporteur |
| HARMAND Jean-Christophe | Directeur de Recherche CNRS, C2N Palaiseau | Rapporteur |
| BARBIER Antoine | Directeur de Recherche CEA, CEA Saclay | Examinateur |
| PLISSARD Sébastien | Chargé de Recherche CNRS, LAAS Toulouse | Examinateur |
| VINCENT Laetitia | Directrice de Recherche CNRS, C2N Palaiseau | Examinatrice |
| DANESCU Alexandre | Maitre de conférences, INL Ecully | Directeur de thèse |
| BUGNET Matthieu | Chargé de Recherche CNRS, MATEIS Villeurbanne | Invité et co-directeur de thèse |
| PENUELAS José | Maitre de conférences, INL Ecully | Invité et co-directeur de thèse |

# Acknowledgements

The work presented in this manuscript has been achieved after three years and a half of efforts, with the support of many people. I hence want to dedicate the first pages of this manuscript to all the people that get involved during this period.

Firstly, I would like to thanks José Penuelas, Alexandre Danescu and Matthieu Bugnet, for being such nice supervisors over these years of theses, by sharing their positivity and knowledge. It was a real pleasure to work with you and to discuss about science and other things at any time. I would like to thank José and Alex who have followed my work since my first internship of master. Matthieu, for the very good introduction to the electron microscopy world and of course the for all the interesting discussions we had during the many STEM sessions we had together in St-Etienne. Of course, I have to dedicate a special thanks to Michel Gendry. You were the first one to make me think about starting a PhD thesis. I really learnt a lot from your experience and knowledge during all the long discussion we had together in your office. I hope you will enjoy your retirement, full of pastis next to the swimming pool. José, Alex and Matthieu, I really appreciate working with you and I hope we will be able to collaborate again in the future.

I also want to thanks the members of the jury that have accepted to read and evaluate my manuscript and thesis work. Prof. Erik Bakkers, Dr. Jean-Christophe Harmand, Dr. Antoine Barbier, Dr. Sébastien Plissard and Dr. Leatitia Vincent, thanks you for all the feedbacks you gave after the evaluation of my work.

I would like to acknowledge the direction of INL, Catherine Bru-Chevalier, Christian Seassal and Bruno Masenelli for the support provided during this thesis. The help from Sylvie Goncalves and Patricia Dufaut who had to endure a huge amount of stupid questions at all time, and of course Bénédicte André, Raphaël Lopez and Laurent Carrel for the administrative and informatics help.

Of course, I would like to thanks all the members of the Functional Materials and Nanostructures team and Nanolyon staff for all the technical and financial support. Philippe Regreny, for all the help provided during experiments and all the constructive discussions we had together. Jean-Baptiste Goure, you were our savior thanks to whom everything was working nicely. Claude Botella, for the automation of the reactors, the XPS analysis and all the fruitful discussions about RHEED improvements and ideas. Nicolas Chauvin, thank you for the PL measurements and analysis. Solène Brottet, for the fabrication of all the FIB lamella needed for my studies. And of course, Romain Bachelet, Guillaume Saint-Girons, Geneviève Grenet, Céline Chevalier, Jean-Louis Leclercq, Brice Devif, Pierre Cremillieu, Thomas Gehin and Radek Mazurczyk for all the help and assistance provided during these years.

I also would like to thanks Stéphanie Reynaud, Yaya Lefkir and Mimoun Aouine for the help you gave during the TEM sessions made in Saint-Etienne and in Villeurbanne. I really appreciate your kindness and I hope I will be able to meet you again in the future.

This PhD work being supported by the ANR, I would like to thanks the collaborators I had during these years: Vincent Artero, Matthieu Koepf and Mariam Fadel from the LCBM, CEA Grenoble, for all the characterizations and measurements of the photoactivity of our substrates. Hélène Magnan and Antoine Barbier from the CEA Saclay as well as Mathieu Silly and Rachid Belkhou from Synchrotron Soleil, for all the experiments and analysis performed during this collaboration.

Obviously, I have to thank all the PhD students I met during these years. Ali, the official Arak provider of the office. Marco, for your incredible dark humor and for giving me your secret voodoo spells to make the R2 works. Hà My, for all the good jokes and discussion about Asian food we had. Martina, my dear Italian friend and great moral support. Gaby and Marc, with whom it's always a pleasure to talk about anything. Iuliia, for your constant good mood, I hope you'll be a worthy opponent in the quest of the hexagonal SiGe. And of course Eirini, Hélène, Mohamed, Dong, Mayeul, Mohab and all the others, with whom I spent great times during my PhD years. To all of you, I wish the best for your PhD.

I also want to address my infinite gratitude to all my family, to my sisters Layana, Isabelle and Magalie and my father Gérard for the support given during all these years. Finally, my last thought will go to my mother, without whom nothing would have been possible. I'm sure you would have been proud of everything accomplished since.

# Table of contents

# 1 Introduction

## Chapter contents



### 1.1 III-V semiconductors to improve photoelectrochemical cell efficiency for light-driven water splitting

#### 1.1.1 The photoelectrochemical cells for water splitting

Simultaneously to the development of industrialized societies, the use of fossil fuels such as natural gas, oil and coal as primary sources of energy has drastically increased during the last century[1], leading to the release of ever-larger quantities of $CO_2$, recognized to be at least partially responsible of the current global-warming crisis. Due to the evident environmental issues caused by the widespread use of non-renewable energy sources, the exploration of alternative strategies to provide green energy at a large scale has become a critical issue for the scientific community. Among all these alternatives, intense efforts are carried out on

the development of photoelectrochemical cells (PEC), capable to produce carbon neutral photosynthesis using solar energy to drive specific chemical reactions and convert abundant resources such as $H_2O$ or $CO_2$ into energy-rich compounds, such as $H_2$, $CH_3OH$ or $NH_3$ that are stable, can be stored and easily distributed[2,3].

Photoelectrochemical devices for water splitting are typically composed by an anode material where the water is oxidized into $O_2$ and $H^+$ through the oxygen evolution reaction (OER) and by a cathode material, where protons are reduced to $H_2$ thanks to the hydrogen evolution reaction (HER). In the case of PEC, at least one of the two electrodes material has to be able to absorb sunlight to generate the electrochemical potential required to drive the OER and the HER reactions[4]. The first effective photoanode for water splitting was reported in 1972 by A. Fujishima and K. Honda[5]. The $TiO_2$ photoanode proposed in that work triggered an intense effort of the community to improve the efficiency of the solar-to-hydrogen (STH) processes[6]. However, the large bandgap of this material is a limitation of the STH efficiency of $TiO_2$-based devices. Indeed, the 3.2 eV bandgap of $TiO_2$ restricts its light absorption to a small fraction of the solar spectrum ($\lambda$ < 400 nm)[7]. To overcome this difficulty, III-V semiconductors such as GaAs or GaP emerged as advantageous compounds, due to narrower bandgaps (1.4 eV and 2.25 eV for GaAs and GaP, respectively) allowing the collection of a larger portion of the solar spectrum[4,8,9]. As a result, III-V semiconductors attracted large attention for the fabrication of photoelectrodes for solar fuels applications.

### 1.1.2 Semiconductor / electrolyte interface

III-V semiconductors appear as ideal candidates for the fabrication of enhanced PEC for water splitting, because of their narrow bandgaps, which allow the absorption of a larger portion of the solar spectrum collected by the photoelectrodes than for $TiO_2$. Indeed, the semiconductor will absorb photons presenting an equal or higher energy than the bandgap of the material. This absorption leads to the excitation of the electrons from the valence band to the conduction band. A recombination of the charge carriers can occur and determines $\tau_{min}$, the minority carrier lifetime. In the case of an illuminated semiconductor, the electron-hole pair generation compensates their recombination rate, leading to an equal concentration of holes (*p)* and electrons (*n)*.

Subsequently, the semiconductor band structure, represented in Figure 1.1.a can be tuned through *n*- or *p*-doping using foreign elements[10], leading to a shift of the Fermi level $E_F$ as illustrated in Figure 1.1.b and Figure 1.1.c, respectively. In the case of an illuminated semiconductor (e.g. a *p*-doped semiconductor), the concentrations of majority and minority carriers are modified. Indeed, for an illuminated *p*-doped semiconductor, a separation of $E_F$ into two quasi-Fermi energies $E_{qF,h}$ and $E_{qF,e}$ is observed with an increase of the electron concentration, as illustrated in Figure 1.1.d. This splitting of $E_F$ is due to the fast photogeneration of electrons and holes, with a slow recombination rate[11].

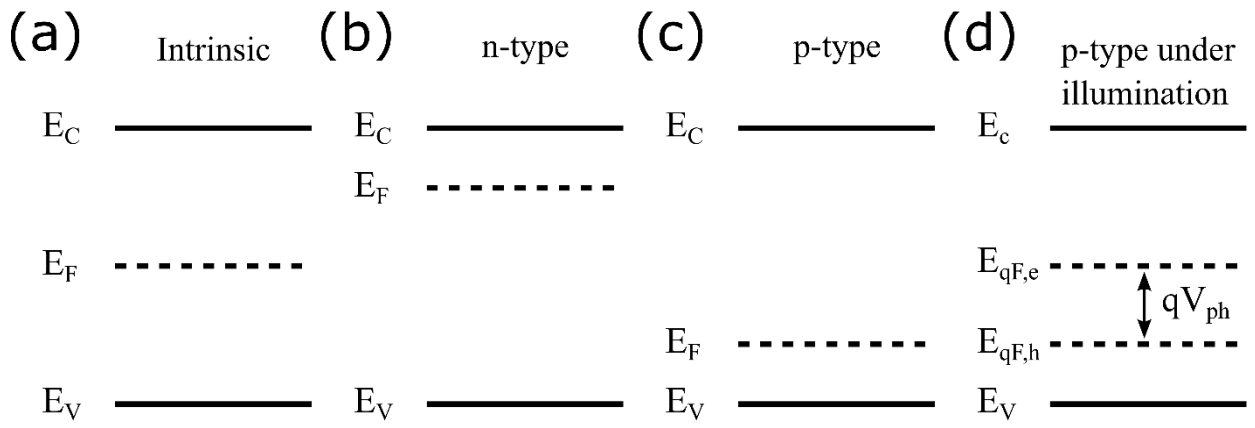


Figure 1.1. Schematic representation of the band diagram in the case of an (a) intrinsic, (b) *n*-doped and (c) *p*-doped semiconductor where the valence and conduction bands, respectively $E_V$ and $E_C$, are represented as well as the Fermi level $E_F$. (d) Splitting of the Fermi level of a *p*-doped semiconductor under illumination into quasi-Fermi levels $E_{qF,e}$ and $E_{qF,h}$.

The quasi-Fermi levels $E_{qF,h}$ and $E_{qF,e}$ can be defined as a function of the carrier concentration:

$$E_{qF,h} = E_i - kTln\left(\frac{p}{p_i}\right), \quad (1.1)$$

$$E_{qF,e} = E_i + kTln\left(\frac{n}{n_i}\right), \quad (1.2)$$

where $E_i$ corresponds to the Fermi level of the intrinsic semiconductor, $k$ is the Boltzmann constant, $T$ the absolute temperature, and $p$, $n$, $p_i$ and $n_i$ correspond to the hole and electron concentration in the doped and intrinsic material, respectively. It should be noted that $n_i$ and $p_i$ are equal due to the nature of an intrinsic semiconductor.

The quasi-Fermi level $E_{qF,h}$ remains almost constant compared to the original Fermi level of the semiconductor in the dark, due to a negligible change of the majority carrier concentration, while the quasi-Fermi level $E_{qF,e}$ drastically increases due to higher electron concentration. The energy difference between $E_{qF,h}$ and $E_{qF,e}$ represents the free energy $\mu_{eh}$ stored in the electron-hole pair, described as follows:

$$\mu_{eh} = \mu_e + \mu_h = E_{qF,e} - E_{qF,h}, \quad (1.3)$$

where $\mu_e$ and $\mu_h$ are the chemical potential of electrons and holes, respectively.

One of the main objectives of the energy conversion based on semiconductor light absorption consists in extracting the largest fraction of the stored free energy. Indeed, this energy is converted to $H_2$ in the case of the PEC water splitting. The potential difference between $E_{qF,h}$ and $E_{qF,e}$ is also referred to as the photovoltage $V_{ph}$.

Once the semiconductor is placed in an electrolyte, in the dark, a quasi-equilibrium is reached between the Fermi level of the semiconductor and the redox pair of the electrolyte, as illustrated in Figure 1.2.a. This equilibrium state induces the bending of the valence and conduction bands near the interface between the semiconductor and the electrolyte. In the case of a *p*-doped semiconductor, the bending produced by the quasi-equilibrium state is favorable to the transfer of the electrons from the semiconductor to the electrolyte, as visible in Figure 1.2.a. Once illuminated, a separation of the Fermi level occurs leading to the formation of the quasi-Fermi energies $E_{qF,h}$ and $E_{qF,e}$, with different photovoltage $V_{ph}$, depending on the illumination intensity[12], as described in Figure 1.1.d. Indeed, a saturated illumination induces a higher photon flux, leading to an increase of the minority carriers, and enhancing the quasi-Fermi level difference, as illustrated in Figure 1.2.b and Figure 1.2.c. The saturated illumination of the semiconductor can lead to a complete disappearance of the band bending as shown in Figure 1.2.c due to the alignment of the quasi-Fermi level $E_{qF,e}$ and $E_{F,\,redox}$, which corresponds to the Femi energy of the redox pair of the electrolyte.

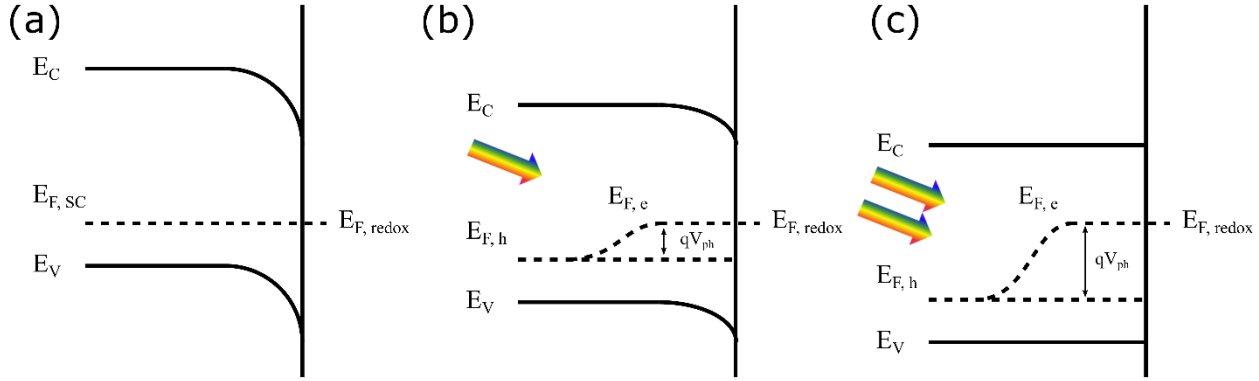


Figure 1.2. Schematic representation of the Fermi level splitting occurring at the interface between a *p*-doped semiconductor and an electrolyte at equilibrium (a) in the dark, (b) under illumination and (c) under saturated illumination.

$E_{F,\,redox}$ represents an equivalent of the Fermi level of a metal in contact with the semiconductor, and can be defined by:

$$E_{F,redox} = \mu_R - \mu_O, \qquad (1.4)$$

where $\mu_R$ and $\mu_O$ represent the chemical potentials of the reduction and oxidation reaction, respectively. Furthermore, the standard electron redox potential $U^0_{redox}$ is defined as the difference of potential between a metal electrode in contact with the electrolyte and a second metal electrode in contact with a solution containing protons (pH = 0) and hydrogen. The second electrode mentioned here is a standard hydrogen electrode (SHE) used as an arbitrary potential zero. Hence, the four most fundamental half reactions of water splitting can be described with their corresponding electrical potentials vs SHE, as presented in Table 1.1.

Table 1.1. Half-reactions and electrode potential vs SHE involved in water splitting for an acidic and base electrolyte.

| | Redox pair | Half-reaction | Potential vs SHE (eV) |
|---|---|---|---|
| Acid pH = 0 | Anode $H_2O$ / $O_2$ | $2\ H_2O \leftrightarrow O_2 + 4\ H^+ + 4\ e^-$ | 1.229 |
| | Cathode $H^+$ / $H_2$ | $2\ H^+ + 2\ e^- \leftrightarrow H_2$ | 0.0 |
| Base pH = 14 | Anode $OH^-$ / $O_2$ | $4\ OH^- \leftrightarrow O_2 + 2\ H_2O + 4\ e^-$ | 0.4 |
| | Cathode $H_2O$ / 2 $e^-$ | $2\ H_2O + 2\ e^- \leftrightarrow H_2 + 2\ OH^-$ | - 0.828 |

The electrical potential of the redox pair is defined versus SHE, while the Fermi level of the semiconductor is expressed versus the vacuum energy level. The redox Fermi energy of SHE, called $E_{F,SHE}$, is commonly accepted as equal to -4.5 eV[13], hence allowing a conversion to the vacuum scale according to the following equation:

$$E^0_{F,redox} = -4.5\ eV - qU^0_{redox}. \qquad (1.5)$$

Therefore, it is possible to position the bandgap of semiconductors as a function of the electrochemical potential of the redox reactions involved in water splitting. Some samples are given in Figure 1.3, taken from ref 14.

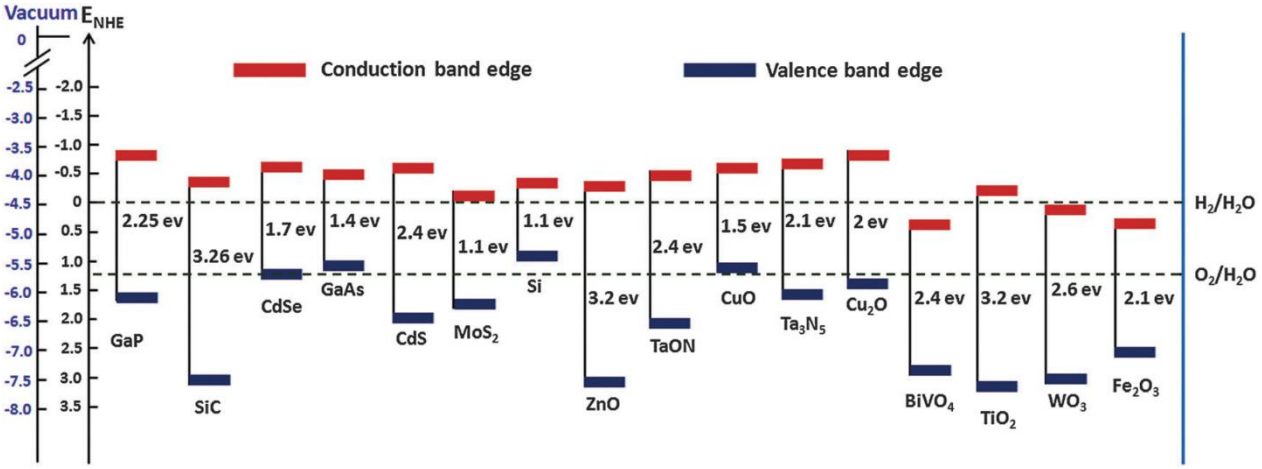


Figure 1.3. Bandgap positions of different semiconductors in contact with an aqueous medium at pH = 0 relative to NHE and the vacuum level. For comparison the HER and OER redox potentials are also presented.[14]

Despite the band bending generated by the illumination of the semiconductor, it is possible to tune the band structure at the electrode / electrolyte interface with the application of a bias $V_{ab}$. Assuming a *p*-doped semiconductor in the dark at a quasi-equilibrium state with the electrolyte redox Fermi energy as represented

in Figure 1.4.a, exhibiting a band bending as described in the previous paragraphs: when a positive bias ($V_{ab} > 0$) is applied to the semiconductor, a shift of the Fermi level is observed toward low energy, inducing a decrease of the band bending, due to an accumulation of holes at the interface between the semiconductor and the electrolyte as illustrated in Figure 1.4.b. On the other hand, a negative bias ($V_{ab} < 0$) leads to an increase of the band bending caused by an accumulation of electron at the interface semiconductor / electrode as showed in Figure 1.4.c. Therefore, the application of a negative bias can enhance the electron transfer from the semiconductor to the electrolyte, thus facilitating the HER.

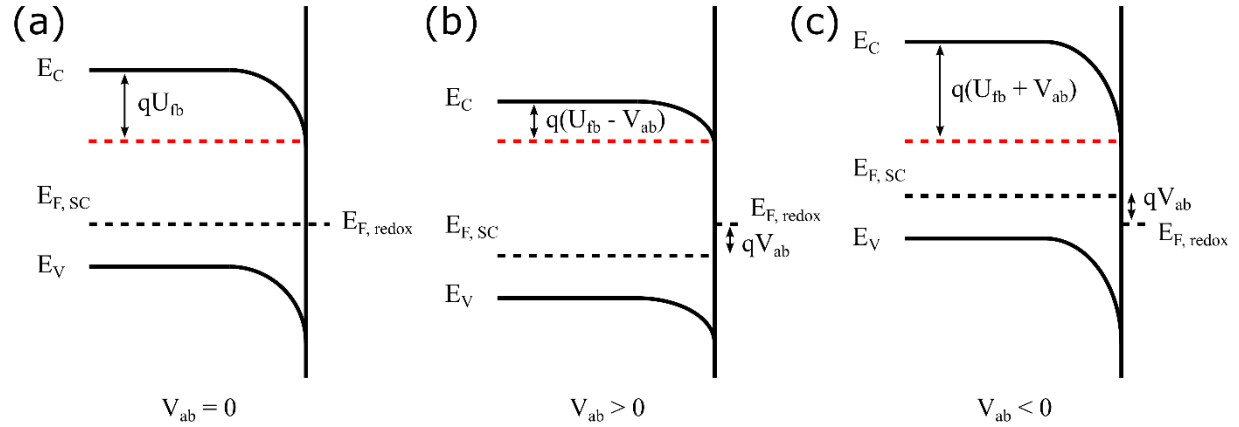


Figure 1.4. Band diagram representations of the band bending at the interface between a *p*-doped semiconductor and an electrolyte in the dark, (a) at equilibrium, (b) under positive bias and (c) under negative bias.

## 1.2 III-V semiconductor nanowires to improve cell efficiency

NW-based photoelectrodes are particularly attractive to enhance the efficiency of PEC for water splitting. Indeed, since the water splitting OER and HER occur at the interface between the electrode and the electrolyte, maximizing the specific surface area in contact with the aqueous medium with the high aspect-ratio of the NW geometry can provide an increase of the cell efficiency. Furthermore, III-V NWs can be easily *n*- or *p*-doped to engineer the band structure and ensure an optimal charge separation resulting from the aforementioned band bending created at the semiconductor / electrolyte interface. A very important characteristic of the NW geometry is its capacity to strongly reduce absorption losses. Indeed, part of the incoming photons can be reflected on the surface of the semiconductor, or transmitted through the semiconductor, thus preventing the charge separation. Focusing on certain types of semiconductors (*i.e.*, GaN, GaAs, GaP or InP) can provide a drastic reduction of the light reflected[15,16]. The NW geometry can also ensure a reduction of the transmission loss, due to its capacity to act as resonant light trap[17,18]. Indeed, NW arrays randomly grown on a substrate can act as scattering or resonance centers[19], hence reducing the absorption losses.

Besides their efficient light trapping capability, NW can also efficiently decouple the light absorption direction and the minority carrier transport direction[20], as illustrated in Figure 1.5. Indeed, the separation and collection of charges can be efficiently improved by the NW geometry in comparison with the planar films.

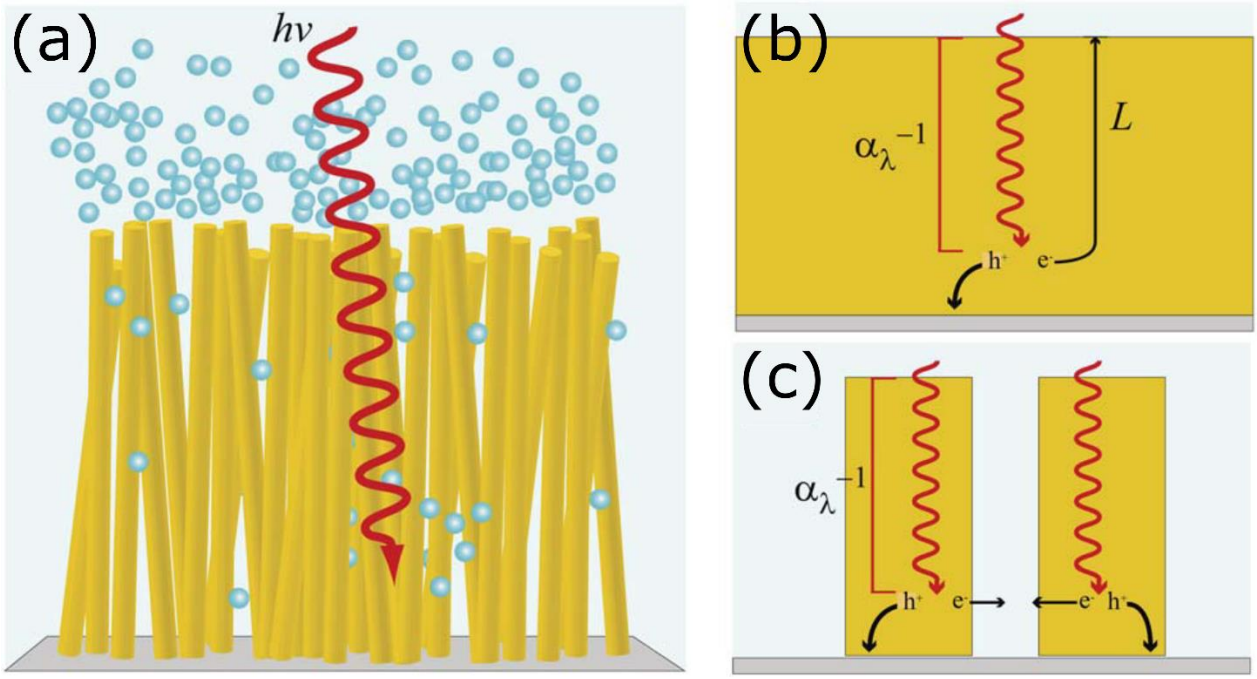


Figure 1.5. (a) Idealized illustration of a NW array functionning as a photoelectrode involved in water splitting. (b) and (c) Comparison of photogenerated charge carrier collection at (b) planar and (c) high aspect ratio photoelectrodes. The grey bottom represents the back contact for majority carrier collection.[20]

Despite their high potential for efficient water splitting, III-V semiconductor NW photoelectrodes suffer from strong corrosion in aqueous medium[21–23] preventing their utilization[24]. However, metal oxide passivation layers have been developed as thin-film protecting shells for semiconductors, compatible with the charge transfer, chemically stable in liquid, and transparent to visible light[25–27]. Many oxides appear as really efficient candidates to reduce or avoid the degradation of the III-V semiconductors, such as $TiO_2$[25,27], $NiO_x$[28], $CoO_x$[29], $SnO_2$[30], $Al_2O_3$[31], $BaTiO_3$[32], or $SrTiO_3$[33].

## 1.3 III-V semiconductor nanowires grown on silicon substrate

In the last decades, III-V semiconductor nanowires (NWs) have attracted many interests in the research community, due to their remarkable properties combining both the advantages of the III-V semiconductors and of the one-dimensionality of NWs. Indeed, III-V NWs can exhibit high aspect-ratios with strong quantum confinements[34], combined with direct bandgaps, high carrier mobility, and an advanced engineering of the band structure. The integration of such one-dimensional nano-objects on silicon wafer has been achieved in 2004 by L. Samuelson's group[35], thus opening the way for novel and complex devices.

Integrating direct bandgap semiconductors such as GaAs in the already well-established silicon industry provides many opportunities for optoelectronic applications such as high-efficiency solar cells[16,36]. Furthermore, the integration of III-V semiconductors can bring new light-emitting properties to materials such as Si or Ge. Indeed, recently E. M. T. Fadaly *et al*. demonstrated that such material could be used as building blocks for direct bandgap emission of hexagonal SiGe alloys[37], hence opening the path toward single chip electronic and the integration of new optoelectronic functionalities.

Furthermore, the introduction of the NW geometry in the silicon industry has overcome one of the main drawbacks of the heteroepitaxial thin film materials, which were the first and most common way to integrate III-V materials on Si substrate[38–40]. Indeed, depending on the value of the lattice mismatch between the semiconductor and the silicon substrate, structural defects appear in the semiconductor. Thin enough films can accommodate the lattice parameter of the substrate, presenting only a small strain. An increase of the film thickness leads to enhanced strain energy, causing the formation of defects to release the stress, such as dislocations, at the interface between the III-V material and the substrate, which in turn induce the recombination of the free carriers generated by the semiconductor. Contrary to thin films, and because of their one-dimensionality, NWs are able to release the stress induced by the lattice mismatch through an elastic relaxation on their lateral surfaces[41,42], also preventing the formation of anti-phase boundaries.

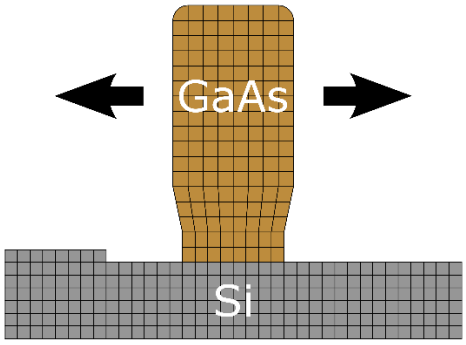


Figure 1.6. Schematic representation of a free-standing GaAs NW on a Si substrate showing the elastic relaxation of the lattice mismatch of about 4.1%[43] between the GaAs NW and the Si substrate, preventing the formation of anti-phase boundaries.

Figure 1.6 shows a schematic representation of the relaxation mechanism, which occurs at the lateral surfaces of a GaAs NW. Ultimately, this geometry can drastically reduce the risks of crack induced by thermal expansion. Despite the fact that several techniques have been developed to reduce the formation of structural defects in the thin film technology, such as substrate miscuts or surface annealing and two-steps growth processes[44–46], the NW geometry remains the optimal choice to obtain crystals free of epitaxy-induced defects such as dislocations or anti-phase boundaries.

Furthermore, III-V semiconductors NWs can observe two different crystal structures: a cubic Zinc Blende (ZB) and a hexagonal Wurtzite (WZ) phases[47]. These two structures exhibit different electronic[48], optical[49–51] and/or mechanical[52] properties, and have attracted a strong interest in the research community since the development of the fundamental basics of their nucleation by F. Glas's group in 2007[53]. The control

of the nucleation of the crystal structure, and thus of the crystalline purity of the material, was a major challenge of the last decade.

## 1.4 Aim of the thesis

The work reported here is part of the ANR (Agence Nationale de la Recherche) – funded project BEEP (Nanowire based electrode engineering for photocatalysis), whose final scope is to integrate III-V NWs in photocathodes and photoanodes combined in a tandem cell for light-driven water splitting. This project involved several academic laboratories such as INL (CNRS), MATEIS (CNRS), ICJ (CNRS), as well as two laboratories of the atomic and alternative energy commission (CEA) SPEC (CEA-Saclay) and LCBM (CEA-Grenoble).

This PhD thesis was dedicated to the growth and the characterization of GaAs and GaP NWs grown by MBE on silicon substrates used as PEC for light-driven water splitting. The VLS growths of self-assisted GaAs NWs and gold-catalyzed GaP NWs by MBE were studied in parallel. The geometry and the morphology of these objects were optimized by changing the growth parameters. Moreover, high homogeneity of the NW morphology on large substrate was achieved. The influence of the geometry and morphology on the PEC activity was investigated, as well as the role of a $TiO_2$ protective shell deposited by atomic layer deposition (ALD). Structural and chemical analysis were performed on the NWs to study the aging and the impact of the reaction on the NWs.

The fundamental aspects of the crystal structure growth mechanism of such NWs were also investigated, and in depth characterizations were performed to understand the growth phenomena and to control the nucleation. For instance, a significant part of this work was devoted to control the formation of the hexagonal or cubic structures on demand, to engineer self-assisted GaAs NWs crystal phases during the VLS growth. Structural analyses using advanced tools such as aberration-corrected scanning transmission electron microscopy and synchrotron radiation nano-beam diffraction were performed on NWs to study their crystal phase as well as their strain at high spatial resolution.

The outline of this manuscript is the following: the principle of the main experimental setups used during this thesis are explained in chapter 2. The basis and concepts behind the growth of self-assisted GaAs NWs and their crystal structure will be discussed in chapter 3. In chapter 4 and 5, my work regarding the control of the growth of self-assisted GaAs using *in situ* characterization tools is discussed, while chapter 6 is dedicated to their advanced *post mortem* characterization. Finally, the reliability of such material applied to the water splitting reaction is discussed in chapter 7.

## 1.5 References

1. Shafiee, S. & Topal, E. An econometrics view of worldwide fossil fuel consumption and the role of US. *Energy Policy* **36**, 775–786 (2008).

2. Lewis, N. S. Introduction: Solar Energy Conversion. *Chem. Rev.* **115**, 12631–12632 (2015).

3. Detz, R. J., Reek, J. N. H. & van der Zwaan, B. C. C. The future of Solar Fuels: When could they become competitive? *Energy Environ. Sci.* **11**, 1653–1669 (2018).

4. Walter, M. G. *et al.* Solar Water Splitting Cells. *Chem. Rev.* **110**, 6446–6473 (2010).

5. Fujishima, A. & Honda, K. Electrochemical Photolysis of Water at a Semiconductor Electrode. *Nature* **238**, 37–38 (1972).

6. Ni, M., Leung, M. K. H., Leung, D. Y. C. & Sumathy, K. A review and recent developments in photocatalytic water-splitting using TiO2 for hydrogen production. *Renewable and Sustainable Energy Reviews* **11**, 401–425 (2007).

7. Sivula, K. & van de Krol, R. Semiconducting materials for photoelectrochemical energy conversion. *Nat Rev Mater* **1**, 15010 (2016).

8. Standing, A. *et al.* Efficient water reduction with gallium phosphide nanowires. *Nat Commun* **6**, 7824 (2015).

9. Alqahtani, M. *et al.* Gallium Phosphide photoanode coated with $TiO_2$ and $CoO_x$ for stable photoelectrochemical water oxidation. *Opt. Express* **27**, A364 (2019).

10. Dubrovskii, V. G., Hijazi, H., Goktas, N. I. & LaPierre, R. R. Be, Te, and Si Doping of GaAs Nanowires: Theory and Experiment. *J. Phys. Chem. C* **124**, 17299–17307 (2020).

11. *Photoelectrochemical Solar Fuel Production*. (Springer International Publishing, 2016). doi:10.1007/978-3-319-29641-8.

12. Walter, M. G. *et al.* Solar Water Splitting Cells. *Chem. Rev.* **110**, 6446–6473 (2010).

13. Xu, Y. & Schoonen, M. A. A. The absolute energy positions of conduction and valence bands of selected semiconducting minerals. *American Mineralogist* **85**, 543–556 (2000).

14. Tamirat, A. G., Rick, J., Dubale, A. A., Su, W.-N. & Hwang, B.-J. Using hematite for photoelectrochemical water splitting: a review of current progress and challenges. *Nanoscale Horiz.* **1**, 243–267 (2016).

15. Tang, Y. B. *et al.* Vertically Aligned p-Type Single-Crystalline GaN Nanorod Arrays on n-Type Si for Heterojunction Photovoltaic Cells. *Nano Lett.* **8**, 4191–4195 (2008).

16. Colombo, C., Heiβ, M., Grätzel, M. & Fontcuberta i Morral, A. Gallium arsenide p-i-n radial structures for photovoltaic applications. *Appl. Phys. Lett.* **94**, 173108 (2009).

17. Kupec, J., Stoop, R. L. & Witzigmann, B. Light absorption and emission in nanowire array solar cells. *Opt. Express* **18**, 27589 (2010).

18. Anttu, N. & Xu, H. Q. Coupling of Light into Nanowire Arrays and Subsequent Absorption. *J. Nanosci. Nanotech.* **10**, 7183–7187 (2010).

19. Muskens, O. L. *et al.* Large Photonic Strength of Highly Tunable Resonant Nanowire Materials. *Nano Lett.* **9**, 930–934 (2009).

20. Foley, J. M., Price, M. J., Feldblyum, J. I. & Maldonado, S. Analysis of the operation of thin nanowire photoelectrodes for solar energy conversion. *Energy Environ. Sci.* **5**, 5203–5220 (2012).

21. Standing, A. *et al.* Efficient water reduction with gallium phosphide nanowires. *Nat Commun* **6**, 7824 (2015).

22. van Vugt, L. K., Veen, S. J., Bakkers, E. P. A. M., Roest, A. L. & Vanmaekelbergh, D. Increase of the Photoluminescence Intensity of InP Nanowires by Photoassisted Surface Passivation. *J. Am. Chem. Soc.* **127**, 12357–12362 (2005).

23. Kim, D. R., Lee, C. H., Rao, P. M., Cho, I. S. & Zheng, X. Hybrid Si Microwire and Planar Solar Cells: Passivation and Characterization. *Nano Lett.* **11**, 2704–2708 (2011).

24. Khaselev, O. & Turner, J. A. A Monolithic Photovoltaic-Photoelectrochemical Device for Hydrogen Production via Water Splitting. *Science* **280**, 425–427 (1998).

25. Hu, S. *et al.* Amorphous $TiO_2$ coatings stabilize Si, GaAs, and GaP photoanodes for efficient water oxidation. *Science* **344**, 1005–1009 (2014).

26. Hu, S. *et al.* Thin-Film Materials for the Protection of Semiconducting Photoelectrodes in Solar-Fuel Generators. *J. Phys. Chem. C* **119**, 24201–24228 (2015).

27. Bae, D., Seger, B., Vesborg, P. C. K., Hansen, O. & Chorkendorff, I. Strategies for stable water splitting via protected photoelectrodes. *Chem. Soc. Rev.* **46**, 1933–1954 (2017).

28. Zhou, X. *et al.* Interface engineering of the photoelectrochemical performance of Ni-oxide-coated n-Si photoanodes by atomic-layer deposition of ultrathin films of cobalt oxide. *Energy Environ. Sci.* **8**, 2644–2649 (2015).

29. Reece, S. Y. *et al.* Wireless Solar Water Splitting Using Silicon-Based Semiconductors and Earth-Abundant Catalysts. *Science* **334**, 645–648 (2011).

30. Azevedo, J. *et al.* Tin oxide as stable protective layer for composite cuprous oxide water-splitting photocathodes. *Nano Energy* **24**, 10–16 (2016).

31. Fan, R. *et al.* Surface passivation and protection of Pt loaded multicrystalline $pn^+$ silicon photocathodes by atmospheric plasma oxidation for improved solar water splitting. *Appl. Phys. Lett.* **109**, 233901 (2016).

32. Toupin, J. *et al.* Engineering n-p junction for photo-electrochemical hydrogen production. *Phys. Chem. Chem. Phys.* **19**, 30675–30682 (2017).

33. Ji, L. *et al.* A silicon-based photocathode for water reduction with an epitaxial SrTiO3 protection layer and a nanostructured catalyst. *Nature Nanotech* **10**, 84–90 (2015).

34. Dick, K. A. & Caroff, P. Metal-seeded growth of III–V semiconductor nanowires: towards gold-free synthesis. *Nanoscale* **6**, 3006–3021 (2014).

35. Samuelson, L. *et al.* Semiconductor nanowires for novel one-dimensional devices. *Physica E: Low-dimensional Systems and Nanostructures* **21**, 560–567 (2004).

36. Mayer, B. *et al.* Lasing from individual GaAs-AlGaAs core-shell nanowires up to room temperature. *Nat Commun* **4**, 2931 (2013).

37. Fadaly, E. M. T. *et al.* Direct Bandgap Emission from Hexagonal Ge and SiGe Alloys. *Nature* **580**, 205–209 (2020).

38. Akiyama, M., Kawarada, Y. & Kaminishi, K. Growth of Single Domain GaAs Layer on (100)-Oriented Si Substrate by MOCVD. *Jpn. J. Appl. Phys.* **23**, L843–L845 (1984).

39. Inoue, T., Yamamoto, Y., Koyama, S., Suzuki, S. & Ueda, Y. Epitaxial growth of $CeO_2$ layers on silicon. *Appl. Phys. Lett.* **56**, 1332–1333 (1990).

40. Golecki, I., Reidinger, F. & Marti, J. Single-crystalline, epitaxial cubic SiC films grown on (100) Si at 750 °C by chemical vapor deposition. *Appl. Phys. Lett.* **60**, 1703–1705 (1992).

41. Ihn, S.-G., Song, J.-I., Kim, Y.-H. & Lee, J. Y. GaAs nanowires on Si substrates grown by a solid source molecular beam epitaxy. *Appl. Phys. Lett.* **89**, 053106 (2006).

42. Paek, J. H., Nishiwaki, T., Yamaguchi, M. & Sawaki, N. Catalyst free MBE-VLS growth of GaAs nanowires on (111)Si substrate. *Phys. Status Solidi (c)* **6**, 1436–1440 (2009).

43. Gerthsen, D., Ponce, F. A., Anderson, G. B. & Chung, H. F. Lattice Mismatch Effects in Gaas Epitaxy on Si and GaP. *MRS Proc.* **122**, 21 (1988).

44. Kroemer, H. Polar-on-nonpolar epitaxy. *Journal of Crystal Growth* **81**, 193–204 (1987).

45. Fang, S. F. *et al.* Gallium arsenide and other compound semiconductors on silicon. *Journal of Applied Physics* **68**, R31–R58 (1990).

46. Nozawa, K. & Horikoshi, Y. Effects of Annealing on the Structural Properties of GaAs on Si(100) Grown at a Low Temperature by Migration-Enhanced Epitaxy. *Jpn. J. Appl. Phys.* **29**, L540–L543 (1990).

47. Yeh, C.-Y., Lu, Z. W., Froyen, S. & Zunger, A. Zinc-blende–wurtzite polytypism in semiconductors. *Phys. Rev. B* **46**, 10086–10097 (1992).

48. Capiod, P. *et al.* Band offsets at zincblende-wurtzite GaAs nanowire sidewall surfaces. *Appl. Phys. Lett.* **103**, 122104 (2013).

49. Spirkoska, D. *et al.* Structural and optical properties of high quality zinc-blende/wurtzite GaAs nanowire heterostructures. *Phys. Rev. B* **80**, 245325 (2009).

50. Ahtapodov, L. *et al.* A Story Told by a Single Nanowire: Optical Properties of Wurtzite GaAs. *Nano Lett.* **12**, 6090–6095 (2012).

51. Vainorius, N. *et al.* Observation of type-II recombination in single wurtzite/zinc-blende GaAs heterojunction nanowires. *Phys. Rev. B* **89**, 165423 (2014).

52. Mante, P.-A., Lehmann, S., Anttu, N., Dick, K. A. & Yartsev, A. Nondestructive Complete Mechanical Characterization of Zinc Blende and Wurtzite GaAs Nanowires Using Time-Resolved Pump–Probe Spectroscopy. *Nano Lett.* **16**, 4792–4798 (2016).

53. Glas, F., Harmand, J.-C. & Patriarche, G. Why Does Wurtzite Form in Nanowires of III-V Zinc Blende Semiconductors? *Phys. Rev. Lett.* **99**, 146101 (2007).

# 2 Experimental techniques of synthesis and characterization

## Chapter contents



### 2.1 Epitaxial growth

The word epitaxy derives from the Greek prefix *epi*, meaning “above” and from *taxis* for “order” or “arrangement”. The epitaxial growth designates the ordered process where thin layers of crystalline material are deposited on a crystalline substrate. The grown layers thus exhibit a well-defined orientation induced by the crystal structure of the substrate. Depending on the grown layer composition, the epitaxial growth can be divided into homoepitaxy or heteroepitaxy, when the substrate and layer compounds are identical or different, respectively.

The epitaxial growth of thin layers can follow three different modes, as illustrated in Figure 2.1. The Frank-van der Merwe mode (Figure 2.1.a), also called the 2D or layer-by-layer growth mode, designates a growth mode where new atomic layers are nucleated only after the complete formation of the underlying one. This case occurs in the particular case where the interactions between the substrate and the growing layer are stronger than the lateral interactions between overlayer atoms. The Volmer-Weber or "island" growth mode (Figure 2.1.b) corresponds to the formation of discontinuous structures of one or more atomic layers, the so-called "islands". These formed islands can then eventually merge together, forming a single epitaxial layer. In this growth mode, the interactions between the deposited atoms are stronger than with the substrate. The third so-called Stranski-Krastanov mode (Figure 2.1.c) designates the mix of the two previous modes. Indeed, in this mode, the deposition of entire atomic layers is followed by the formation of islands until the surface is completely covered.

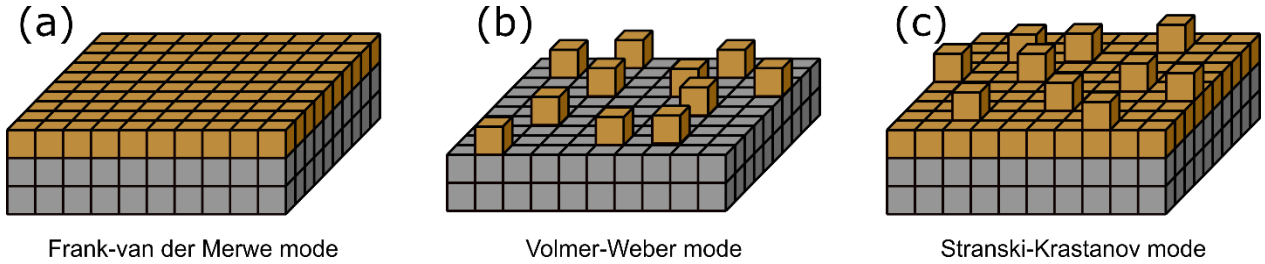


Figure 2.1. Schematic comparison of the three thermodynamic modes of epitaxial growth.[1]

The atoms or molecules arriving on the substrate with an incident flux $F$, can be adsorbed and interdiffused in the first atomic layers of the substrate, or can diffuse on the surface to form a new nucleation site when in contact with other groups of atoms. These mechanisms are dependent on the nature and temperature of the substrate. The diffusion process is governed by the diffusion coefficient $D_{at}$ defined by the following equation:

$$\boldsymbol{D_{at} = D_0 e^{-\frac{E_d}{k_B T}},} \qquad (2.1)$$

where $D_0$ represents the diffusion constant related to the atom, $E_d$ corresponds to the energy needed to move on the surface, $k_B$ the Boltzmann constant, and $T$ the temperature of the substrate. Hence, two major contributions can be identified to have strong influence on the diffusion coefficient $D_{at}$. Indeed, an increase of the substrate temperature $T$ implies an expansion of the diffusion coefficient, and subsequently of the diffusion length of the atoms on the surface. On the contrary, the increase of the energy $E_d$ leads to the diminution of the diffusion length of the atoms. The energy $E_d$ can be increased due to defect on the surface of the substrate (e.g. dislocations, atomic steps).

Typically, the epitaxial growth can be performed through different techniques, such as chemical vapor deposition (CVD), metalorganic chemical vapor deposition (MOCVD) and molecular beam epitaxy (MBE) which will be discussed more into details in the next paragraph. In this work, the epitaxial growth were used

to synthetize NWs using MBE. The growth mechanism implied in such process will be discussed in details in the next chapter.

## 2.2 Molecular beam epitaxy

The epitaxial growth achieved by MBE consists in exposing a substrate to localized beams of atoms (or molecules) under an ultra-high vacuum (UHV) environment, which corresponds to pressures in the $10^{-9}$ to $10^{-11}$ Torr range. This technique is used to synthetize materials such as semiconductors, metals or oxides. A schematic representation of the top view of a MBE chamber (also called reactor) is provided in Figure 2.2. The UHV condition needed for the epitaxial growth are obtained by employing ionic and turbomolecular pumps, cryogenic panels (cryoshield) and titanium sublimation. The atomic or molecular beams are thermally produced using effusion cells heated and regulated using PID controllers and thermocouple feedback. Heated cells are directed toward the sample holder, providing the vapor flux necessary for the epitaxial growth.

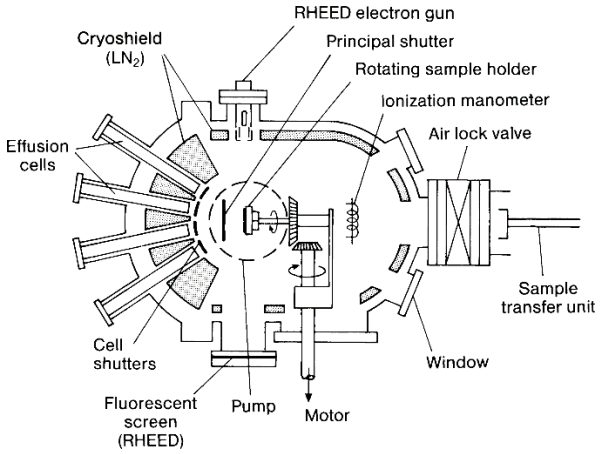


Figure 2.2. Illustration of the UHV chamber of a MBE reactor.[2]

In the case of III-V semiconductor MBE growth, two kinds of cells are used. On the one hand, group V elements sees their fluxes tuned using valves, at constant cell temperature. On the other hand, group III elements fluxes are controlled by varying the temperature of the effusion cell. In the latter case, the incoming vapor flux *J* of a specific compound *i* reaching a unit area of the substrate per second is related to the cell temperature $T_i$ though the following equation[1]:

$$\boldsymbol{J_i = \sqrt{\frac{N_A}{2k_B\pi}} * \frac{p_i}{\sqrt{M_i T_i}}}, \qquad (2.2)$$

where $N_A$ is the Avogadro number, $k_B$ the Boltzmann constant, $p_i$ the pressure measured by a flux ion gauge, also called the beam equivalent pressure (BEP) and $M_i$ the atomic (or molecular) mass. The atomic

or molecular vapor flux can be provided on demand on the substrate through the controlled opening and closing of mechanical cell shutters.

The crystalline substrates used for the epitaxial growth are fixed on molybdenum disks called molyblocks, using tungsten pins or molten indium. The molyblock can then be introduced in the reactor and placed on the sample holder. The sample can be heated once in place in the sample holder using a heating filament, and the temperature can be controlled via a thermocouple located on the sample holder, below the molyblock.

All the MBE growth presented in this manuscript were performed in a clean room environment, using two different MBE reactors. A Riber R32 MBE reactor (Figure 2.3.a), connected under UHV to an oxide MBE reactor and to an XPS chamber, was used to grow samples on 1 × 1 cm² substrates. A Riber C21 MBE reactor (Figure 2.3.b), connected under UHV to a PECVD ECR reactor, was used to grow samples on 2" substrates. The PECVD ECR reactor was equipped with an atomic layer deposition[3] (ALD) module, allowing the deposition of $TiO_2$ layers.

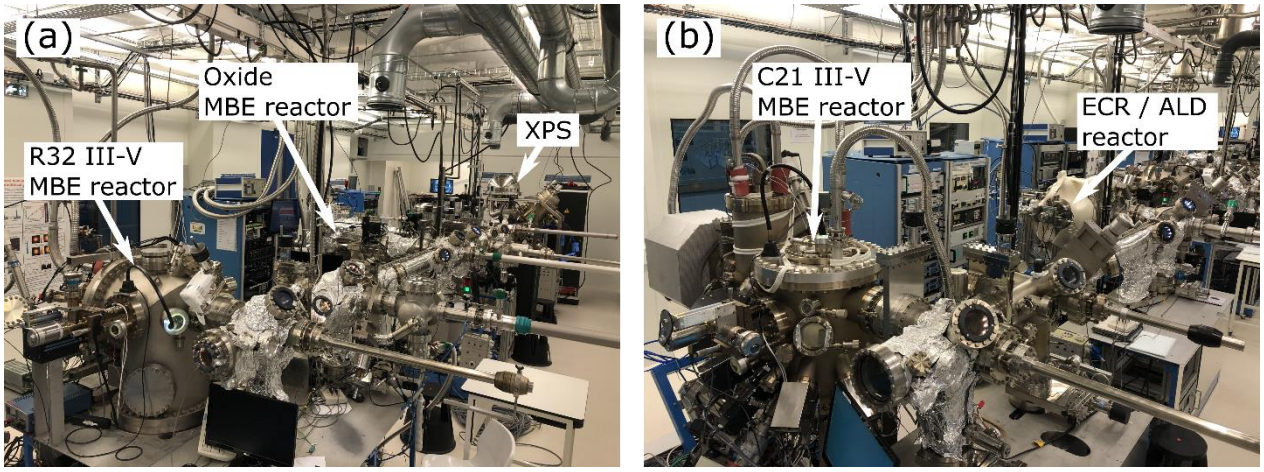


Figure 2.3. Images of the clean room facilities showing (a) the R32 MBE reactor connected under UHV to an oxide reactor and to an XPS chamber, and (b) the C21 MBE reactor connected under UHV to the PECVD ECR reactor.

## 2.3 Reflective high energy electron diffraction

Reflective high energy electron diffraction (RHEED) is an *in situ* and non-destructive characterization tool used to analyze the surface of the substrate inside the MBE chamber. This surface analysis technique provides important information on the structural quality of the surface in real time, all along the epitaxial growth process.

RHEED analysis is performed using a high-energy electrons beam (20 – 30 keV) hitting the substrate surface with a low incident angle (1° – 3°) with respect to the surface. The electrons diffracted by the crystal structure of the sample are then observed through a diffraction pattern on a fluorescent screen placed in front the electron gun, on the opposite side of the reactor, as illustrated on Figure 2.2. The low incidence angle of

the electron beam leads to a relative limited probed depth, hence providing information on the first monolayers (MLs) of the surface only.

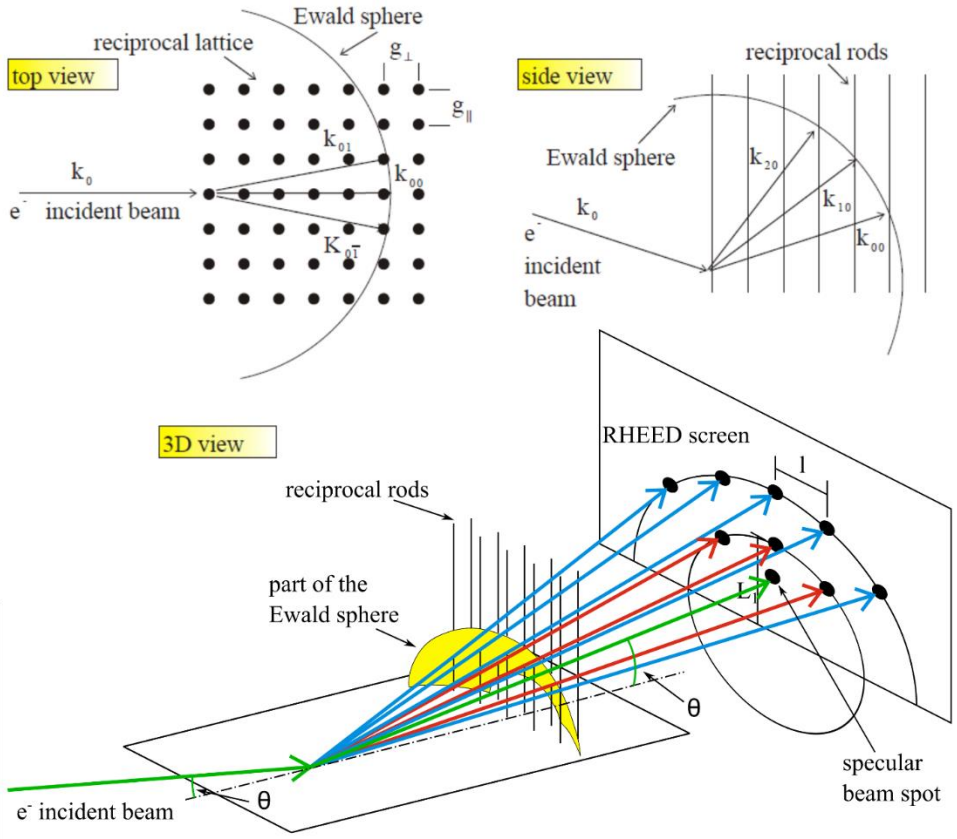


Figure 2.4. Schema showing the principle of the RHEED diffraction on a 2D surface. Figure adapted from Ref [4].

In the ideal case of a sample with a smooth surface, the direct lattice can be approximate to a 2D thin layer. The reciprocal lattice can degenerate into a set of 1D rods along the normal to the surface[4]. These rods will then intersect the Ewald sphere, as shown in Figure 2.4, leading to the formation of spots projected on the fluorescent RHEED screen and semi-circularly arranged along Laue's rings. However, the non-monochromatic nature of the electron beam and the slight roughness of the sample usually lead to a Ewald sphere and 1D rods with a certain thickness, thus inducing lines instead of spots. Hence, observing 2D surface with RHEED usually leads to the appearance of a set of lines.

However, the RHEED can be used as an important tool to understand the growth mechanisms, and especially to determine the epitaxial growth rate of the process. Indeed, RHEED pattern can be used to measure the so-called RHEED oscillations, leading to an indirect observation of the layer forming speed by measuring the intensity evolution of the specular beam spot during the growth. Figure 2.5 provides an illustration of the RHEED intensity evolution during the formation of a new ML. In the case of a 2D growth, the surface can be intended as a smooth layer with a coverage $\theta = 0$. This will lead to the diffusion of all the incident electrons in the same direction, inducing a maximum value for the intensity of the specular beam spot. As soon as a new ML starts to form, the coverage starts to increase (i.e. up to 25 %), leading to the

diffusion of part of the electrons in a different direction, inducing a decrease of the RHEED intensity. Hence, a minimum intensity is observed once the coverage reaches 50%. The intensity then starts to rise again up to a new maximum when a full coverage is observed, as a result of the growth of a complete ML. Consequently the growth rate in ML/s can be measured through the period of the oscillations.

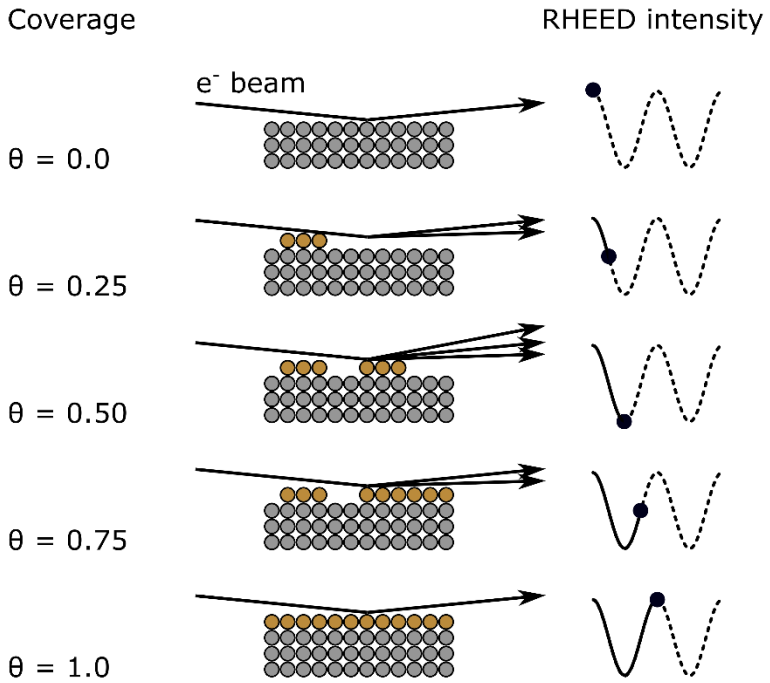


Figure 2.5. Illustration of the RHEED intensity evolution during the 2D growth of 1 ML.

Therefore in the case of III-V materials, the growth rate measured using the RHEED oscillations can be used to determine the fluxes of groups III and V elements, expressed in unit of equivalent 2D growth rates of the III-V materials[5]. In the following parts, we will consider the case of the growth of GaAs as an example.

When growing GaAs 2D layers in an As rich atmosphere, the Ga flux can be expressed in Å/s, corresponding to the growth rate of the GaAs 2D layers measured by RHEED oscillations. In a similar way, the As flux can be express in Å/s when growth is limited by the As flux. Indeed, by progressively increasing the Ga flux under As-limiting conditions (fixed As pressure $P_{As}$), a saturation of the growth rate was reached[5], as illustrated by the black squares, red circles and blue triangles of the plot shown in Figure 2.6.a. The saturation of the growth rate indeed occurs once all the incoming As atoms are incorporated to the forming GaAs layer. Hence, to each $P_{As}$ corresponds a saturated GaAs 2D layer growth rate in Å/s. It is therefore possible to correlate the As flux in Å/s to the As pressure $P_{As}$, as shown in Figure 2.6.b.

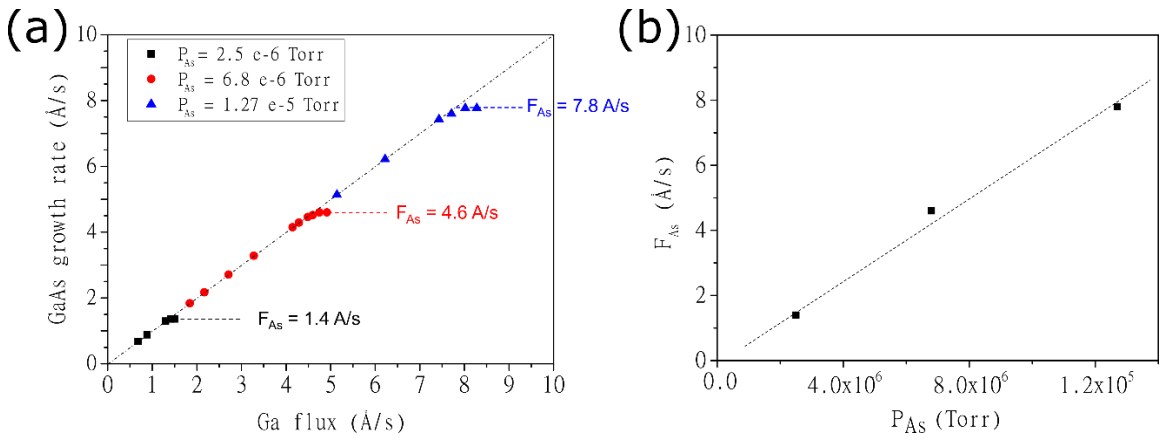


Figure 2.6. (a) Ga-As flux measurements obtained by monitoring RHEED oscillations, showing the saturation of the growth rate. (b) As flux as a function of the As BEP.

## 2.4 Characterization tools

### 2.4.1 Photoelectrochemical characterization

Because of their particular geometry, NWs are particularly attractive for the light-driven water splitting. The photoelectrochemical performances of the photoanodes and photocathodes were measured at the LCBM-CEA Grenoble, by V. Artero's group, using a three electrode (photo)electrochemical cell, filled with a pH 7, 0.1 M phosphate buffer or with a pH 13, 0.1 M potassium hydroxide buffer as electrolyte for the HER or OER, respectively. A titanium wire was used as a counter electrode (CE) and a Ag/AgCl (3 M KCl) electrode acted as a reference electrode (RE). The generated photocurrent was measured from the FTO part, connected to samples with conductive silver paste.

The illumination of the samples was provided by a 280 W Xe lamp. The illumination intensity of the lamp was calibrated using a reference silicon solar cell, leading to an irradiation of 100 mW/cm². A 1.5 atmospheric mass (AM) filter was used to simulate the irradiation of 1 sun.

### 2.4.2 X-ray characterization

#### 2.4.2.1 X-ray photoelectron spectroscopy

The X-ray photoelectron spectroscopy (XPS) consists of a characterization techniques using soft X-rays to excite core and valence electrons at the surface of the material, emitting thus photoelectrons as illustrated in Figure 2.7.a. X-rays are used to irradiate a sample with an energy *hv*, transmitting energy to bound electrons, defined by their binding energy $E_B$, of the compounds present in the sample. The ejected photoelectron can be characterized by its kinetic energy $E_K$.

$$\boldsymbol{E_K = h\nu - E_B - \phi_{sample}}. \qquad (2.3)$$

In order to be detected, photoelectrons need to penetrate into the material to reach the vacuum level $E_{vacuum}$. A minimum energy $\phi$, corresponding to the difference between the Fermi and vacuum levels is needed. The Fermi levels of the material and spectrometer are aligned with by electric contact, implying two energies $\phi_{sample}$ and $\phi_{spectrometer}$, as illustrated in Figure 2.7.b.

Since every element exhibits a corresponding photoelectron binding energy, it is possible to identify XPS peaks obtained during analysis, based on the binding energies. However, ejected photoelectrons create remaining holes at the surface of the material, inducing a positive charge effect in the case of low-conductive materials. Subsequently, a deceleration of the ejected photoelectrons can be observed, leading to a reduction of their kinetic energies, and to a shift of the XPS spectrum towards higher binding energy side. To overcome these effects, a referential photoemission peak, such as $C_{1s}$ peak at 284.6 eV, is used to estimate the energy shift.

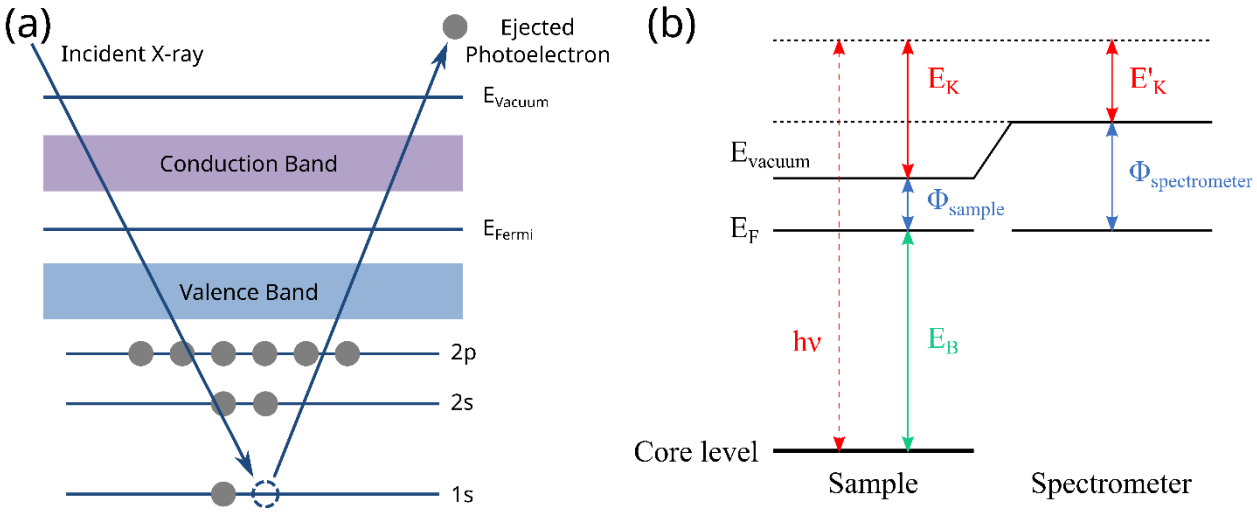


Figure 2.7. Schematic illustration of (a) the photoemission process occurring in a XPS surface analysis, (b) the energy levels of a sample and spectrometer implied in the photoemission process[6].

The probability for a generated photoelectron to escape the sample surface can then be approximate using the Beer-Lambert law:

$$\boldsymbol{I_d = I_0 e^{-\frac{d}{\lambda}}}, \qquad (2.4)$$

where $I_d$ designates the photoelectron intensity originating from atoms at a given depth $d$, $I_0$ denotes the signal emanating from the surface atoms and $\lambda$ is the electron inelastic mean free path, representing the average distance that a photoelectron can travel before undergoing an inelastic scattering. The mean free path is dependent on the material properties and electron kinetic energy. A simplified schematic representation of an XPS instrument is provided in Figure 2.8.

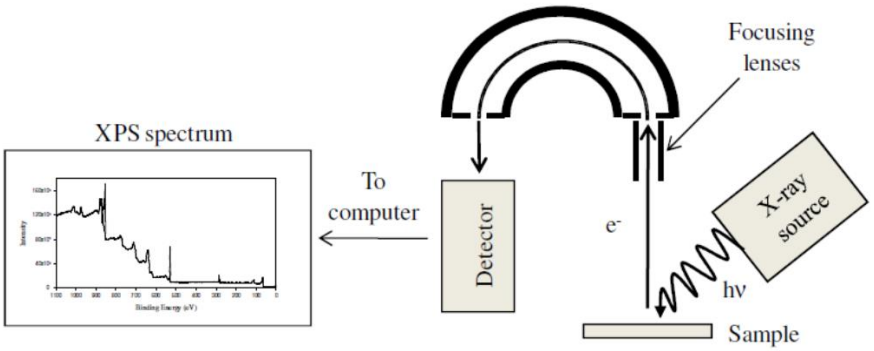


Figure 2.8. Simplified schematic of the XPS instrumental setup.[7]

During this work, XPS facilities available at the TEMPO beamline of the SOLEIL synchrotron[8] were used. TEMPO beamline provides soft X-rays used to study the electronic and magnetic properties of materials. Photon energies in the 50-1500 eV range are accessible, and beam size of about 10 × 40 µm² to 100 × 100 µm². The flux obtained on the sample is about $4 \times 10^{13}$ photons/sec.

### 2.4.2.2 X-ray diffraction

X-ray diffraction (XRD) is a widespread characterization technique capable to give qualitative and quantitative information about the crystalline phases of a material. XRD is based on the interaction of X-rays with matter. A monochromatic X-ray beam is used to illuminate a sample with an incident angle $\theta$ as illustrated in Figure 2.9, and is reflected with the same angle $\theta$ by each atomic plane. Therefore, if the Bragg's law $n\lambda = 2dsin\theta$ is verified, a diffraction occurs through constructive interferences.

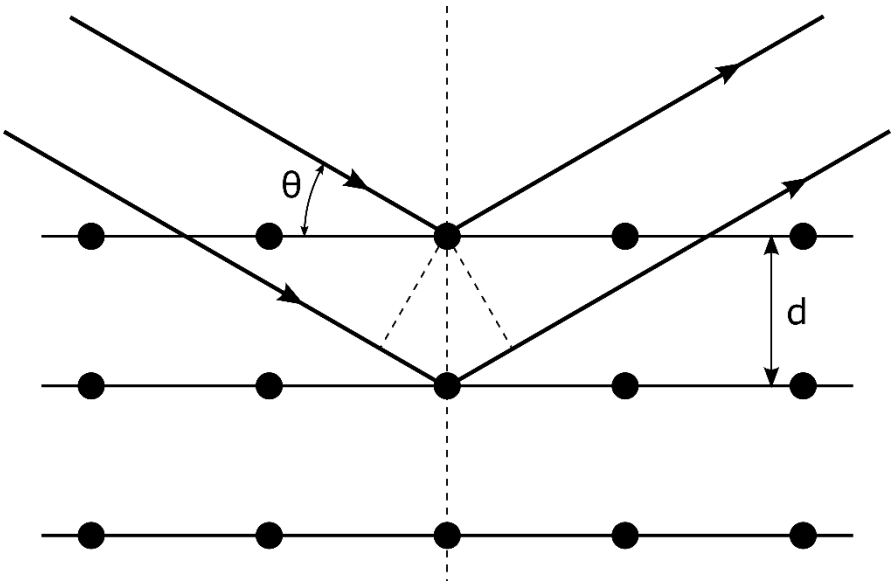


Figure 2.9. Illustration of the Bragg condition implied in XRD.

Bragg's law can be used to determine the inter-reticular distance $d_{hkl}$ in the crystalline direction perpendicular to the *hkl* planes by measuring the diffraction angle $\theta$. In this work, the hard X-ray nano-

diffraction provided by the 26-ID-C beamline[9] of the Advanced Photon Source synchrotron (Argonne, Illinois, USA) was used. The beamline uses X-rays with an energy range of 7-12 keV and a focused beam size of about $0.03 \times 0.03$ µm² with a flux of about $1 \times 10^9$ photons/sec at 10 keV.

### 2.4.3 Electron microscopy characterization

#### 2.4.3.1 Scanning electron microscopy

Scanning electron microscopy (SEM) is a technique in which a beam of electrons is focused on a sample to produce an image by scanning its surface. Most commonly, SEM images are produced using the secondary electrons emitted by the interaction of the electron beam exciting the atoms of the sample. A secondary electron detector is used to produce a secondary electron image (SEI) of the sample. The majority of the SEM images presented in this work were obtained using the secondary electron detector of a JEOL JSM 7401F SEM with an acceleration voltage of 10 kV.

#### 2.4.3.2 Transmission electron microscopy

Transmission electron microscopy (TEM) is a technique in which a beam of electrons is accelerated at kinetic energies of typically few tens to hundreds of keV, and transmitted through a specimen. The transmission electron microscope is made of an electron source (gun) generating an electron beam, travelling through several blocks of lenses and deflection coils to guide and manipulate the beam.

Conventional optical microscopes suffer from a bottleneck on their maximal resolution due to the wavelength of the incoming light illuminating the samples. However, the use of an electron beam instead of light overcomes this issue, making atomic resolution possible. Indeed, a 200 kV electron beam induces an extremely short wavelength of about 2.5 pm, leading to a theoretical sub-angström resolution.

The characterizations performed in this work were carried out using scanning transmission electron microscope (STEM) in high angle annular dark-field mode (HAADF) mode. The principle of STEM is illustrated in the simplified schematic in Figure 2.10. In this technique, the signal obtained can be approximated to the summed intensities of the elastic Rutherford scattering from the nucleus of the atoms irradiated by the electron beam. Contrary to conventional TEM, the STEM technique uses a focused electron beam (typically 0.05-0.2 nm) scanned over a sample using deflection scan coils, as illustrated in Figure 2.10. The intensity in the images obtained is proportional to $Z^2$, where Z corresponds to the atomic number of the atom. In practice, atomic-resolution is achieved with a STEM probe corrected of geometrical aberrations, leading to a sub-angström probe size.

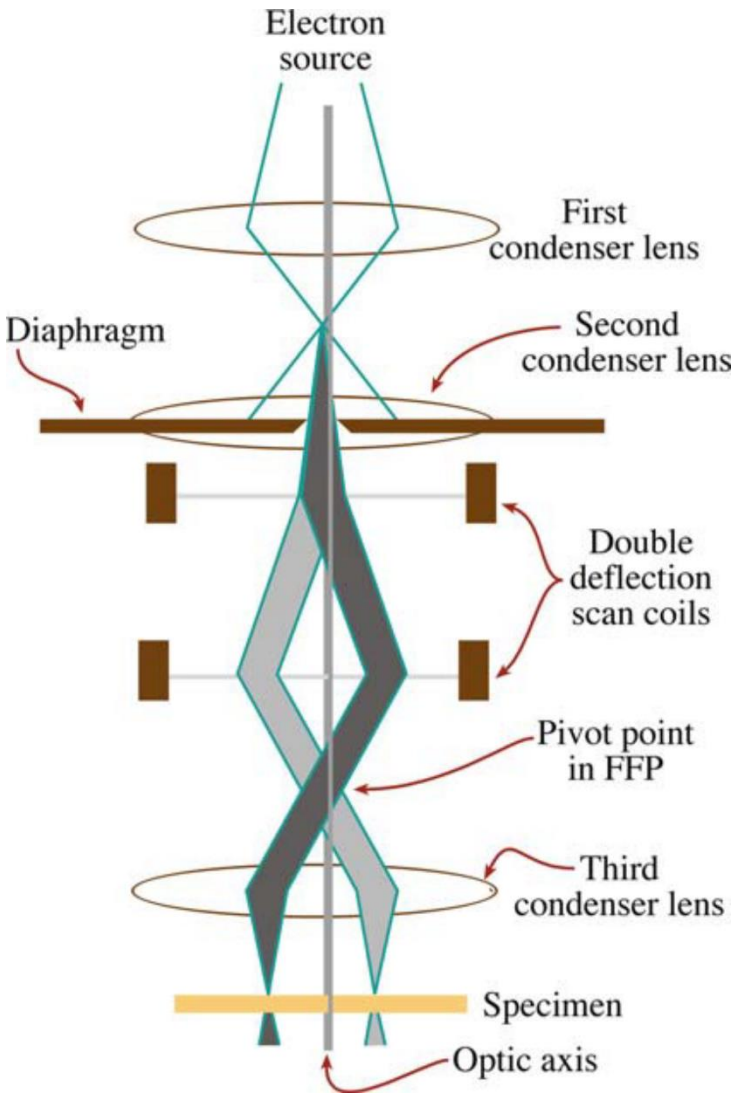


Figure 2.10. Simplified schematic illustration of the STEM imaging system.[10]

The reader interested in STEM is encouraged to refer to books dedicated to TEM and associated techniques such as the ones of D. B. Williams and C. B. Carter[10], of M. D. Shannon for the introduction to aberration-corrected STEM[11].

The majority of the images presented in this work were obtained in STEM-HAADF. These characterizations were carried out at the Consortium Lyon Saint-Etienne de Microscopie (CLYM) facilities in a JEOL-ARM200F NeoARM. This microscope is equipped with a high brightness cold-FEG, a last generation aberration-corrector (CEOS ASCOR) of the condenser lenses, and a Gatan GIF Quantum for electron energy-loss spectroscopy. The microscope was operated at 200 kV.

Additional experiments for selected area electron diffraction and bright-field TEM imaging were carried out in a Jeol JEM2100 with a LaB6 gun at Institut Lumière Matière, UMR5306 UCBL–CNRS.

### 2.4.3.3 Electron energy-loss spectroscopy

Electron energy-loss spectroscopy (EELS) in the TEM is a technique of characterization, which analyses the energy distribution of transmitted electrons after they have interacted with a sample. Fast incident electrons, which are typically accelerated at 60-300 kV, pass through the sample while interacting with the atoms constituting the material through Coulomb forces. A portion of the incident electrons is inelastically scattered, losing energy and changing the direction of their momentum, leading to multiple excitations in the sample, such as plasmons, interband transitions, ionization edges, etc.

The electrons transmitted through the sample are collected into an EEL spectrometer, separating them accordingly to their kinetic energy. An electron energy-loss spectrum shows the electron counts as a function of their energy lost during the process. Figure 2.11 displays a typical electron energy-loss spectrum recorded over a range of 1000 eV in $YBa_2Cu_3O_7$. The zero-loss peak visible on the left corresponds to the signal of the electrons transmitted without any measurable energy loss, i.e. elastically scattered. In the region of high energy-losses (>100 eV), or core losses, the elements present in the sample can be determined from their ionization edges, corresponding to the excitation of their specific core levels. The electrons of these atoms are excited up to the conduction band. Since the energy-loss is approximately the binding energy of the scattering atom, it is possible to determine the species present in the sample using the energy-loss spectrum.

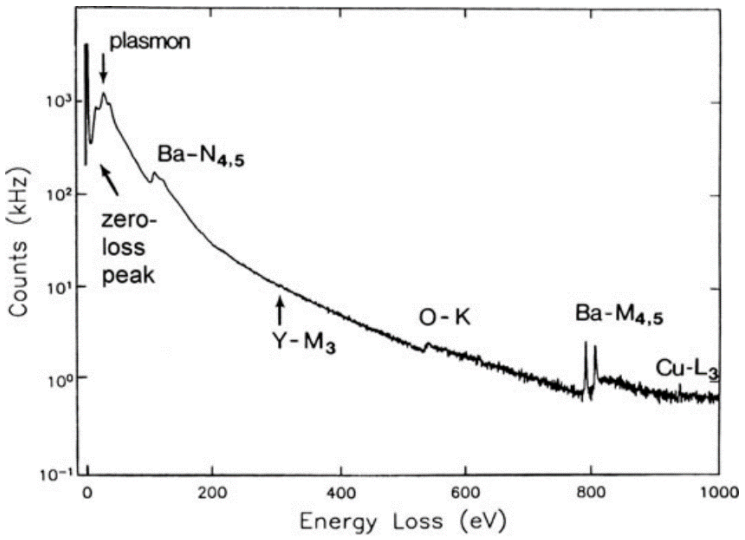


Figure 2.11. Typical electron energy-loss spectrum of a superconductor ($YBa_2Cu_3O_7$) sample, showing the electron intensity as a function of the electron energy-loss. The zero-loss and plasmon peaks, as well as the ionization edges of each elements are visible.[12]

In this work, EELS in STEM mode was used to create elemental mapping at the atomic-scale in our specimens. The spectrum-image technique in STEM-EELS was used as implemented in the Gatan Digital Micrograph software.

The reader interested in more details about EELS is encouraged to refer to books dedicated to this technique such as the one of R. F. Egerton[12].

## 2.5 References

1. Herman, M. A. & Sitter, H. *Molecular beam epitaxy: fundamentals and current status*. (Springer, 1996).

2. Ibach, H. & Lüth, H. *Solid-State Physics*. (Springer Berlin Heidelberg, 2009). doi:10.1007/978-3-540-93804-0.

3. George, S. M. Atomic Layer Deposition: An Overview. *Chem. Rev.* **110**, 111–131 (2010).

3 J. Klein, Epitaktische Heterostrukturen Aus Dotierten Manganaten, Universität zu Köln, **2001**.

5. Rudolph, D. *et al.* Direct Observation of a Noncatalytic Growth Regime for GaAs Nanowires. *Nano Lett.* **11**, 3848–3854 (2011).

6. Fouquat, L. Étude par photoémission d'interfaces métal/oxyde et métal/semiconducteur élaborées par épitaxie par jet moléculaire. 166.

7. Payne, B. P. X-ray Photoelectron Spectroscopy Studies on the Oxidation Processes of Nickel, Chromium and their Alloys. (2011).

8. Polack, F. *et al.* TEMPO: a New Insertion Device Beamline at SOLEIL for Time Resolved Photoelectron Spectroscopy Experiments on Solids and Interfaces. in 185–188 (2010). doi:10.1063/1.3463169.

9. Hruszkewycz, S. O. *et al.* Coherent Bragg nanodiffraction at the hard X-ray Nanoprobe beamline. *Phil. Trans. R. Soc. A.* **372**, 20130118 (2014).

10. Williams, D. B. & Carter, C. B. *Transmission electron microscopy: a textbook for materials science*. (Springer, 2008).

11. Shannon, M. D. Applications of Aberration-Corrected Scanning Transmission Electron Microscopy. in *Aberration-Corrected Analytical Transmission Electron Microscopy* (ed. Brydson, R.) 211–240 (Wiley, 2011). doi:10.1002/9781119978848.ch8.

12. Egerton, R. F. *Electron Energy-Loss Spectroscopy in the Electron Microscope*. (Springer US, 2011). doi:10.1007/978-1-4419-9583-4.

# 3 Molecular beam epitaxy growth of GaAs nanowires

## Chapter contents



### 3.1 Introduction

Nowadays III-V semiconductors are used as building block materials for numerous commercial and high-end electronic and optoelectronic devices[1–4]. Integrating highly efficient III-V semiconductors such as GaAs on low cost silicon thus appears as an important milestone for applications and has been intensively investigated in the last decades. However, the presence of a lattice mismatch between silicon and III-V semiconductors represents a limiting factor for the fabrication and performances of such heterostructures. A reduction of the luminescence properties of 2D layers of GaAs on Si, induced by a lattice mismatch of 4.1%, was highlighted by Gerthsen *et al* in 1988[5]. Nonetheless, the presence of such defects has recently been used to enhance the efficiency of photoelectrodes for the water oxidation and reduction reactions[6].

To overcome the lattice mismatch consequences, Mårtensson *et al* first reported the fabrication of epitaxially grown III-V NWs on Si substrates, showing luminescence at room temperature[7]. Indeed, the

nanometric scale and geometry of these nano-objects induce an elastic relaxation on their surface, thus minimizing the constraints due to the lattice mismatch[8,9]. These nano-objects have been heavily studied, in particular for energy harvesting and for their high potential for photovoltaics[10–16] and light-driven water splitting[17–22] applications, as a result of their high aspect ratio, efficient charge carrier separation[23] and high light-trapping capabilities, which reduce the reflection of light[10,11].

In this chapter, we investigate the mechanism implied in the MBE growth of NWs, and the impact of the growing parameters on the morphology of self-assisted GaAs NWs grown on silicon substrates.

All the MBE growths, SEM characterizations and result interpretations presented in the parts 3.2.3, 3.2.4 and 3.2.5 of this chapter were realized by myself during this thesis work.

## 3.2 Self-assisted GaAs nanowires grown on silicon substrates

### 3.2.1 Vapor liquid solid mechanism

To synthesize the III-V NWs by MBE, the most commonly used method is the vapor-liquid-solid (VLS) mechanism. The sources of elements used for the growth are heated in effusion cells attached to the MBE reactor, each producing a vapor flux. The growth process is illustrated in Figure 3.1 and can be described as followed. Firstly, an atomic or molecular vapor flux (the vapor phase) is used to create molten metal droplets (the liquid phase) randomly dispersed on a substrate (Figure 3.1.a). These metallic droplets act as a catalyst for the growth and are exposed to vapor fluxes of elements III and V. Secondly, the solid phase nucleates at the interface between the liquid droplet and the substrate once a supersaturation of incoming species is reached inside the droplets. The NWs (the solid phase) then grow monolayers per monolayer, lifting up the liquid droplets (Figure 3.1.b). This process continues until the interruption of the incoming vapor fluxes, effectively ending the growth process (Figure 3.1.c).

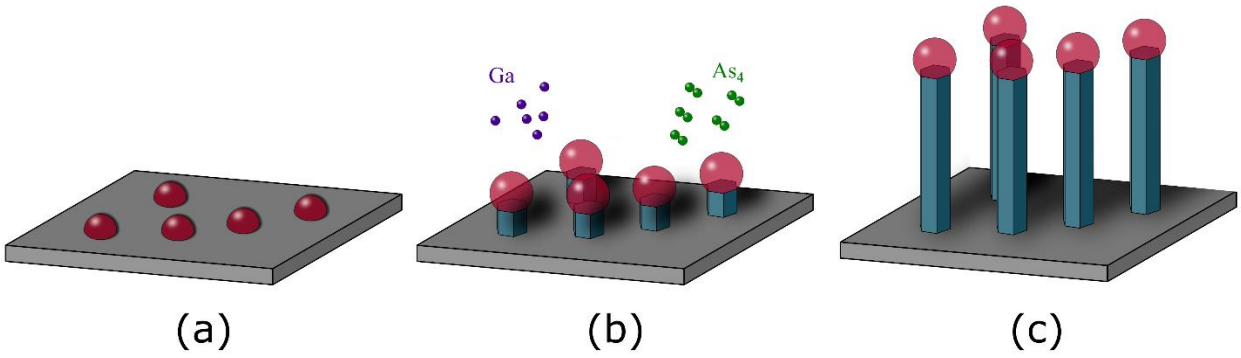


Figure 3.1. Schematic illustrations of the VLS growth mechanism, showing (a) the liquid catalyst droplets on the substrate, (b) the nucleation and growth of the nanowires exposed to Ga and $As_4$ fluxes and (c) the final nanowires array at the end of the growth.

The VLS growth mechanism of NWs can be classified in two different types. Indeed, the liquid droplets used as catalysts for the VLS growth can be formed either with an element constituting the NWs, or with a

foreign element. On the one hand, the crystalline growth using a foreign element, such as Ni, Pd, Pt, or Mn as catalysts is widely used in all epitaxial techniques to synthetize group II-VI, III-V and IV NWs. Still, the most common foreign metal used in the growth of semiconductors NWs is gold. However, over the last few years Au-catalyzed growth progressively lost its interest regarding device fabrication processes. Besides the fact that using gold, a noble metal, is against the cost-reduction principle in device fabrication, a degradation of the devices' performances was observed due to gold-doping of the semiconductors[24,25]. Furthermore, gold impurities introduced in the material by such growth process and are detrimental to the complementary metal-oxide-semiconductor (CMOS) industry.

On the other hand, the crystalline growth catalyzed from droplets made of an element constituting the NWs, called self-assisted (or self-catalyzed) growth, is mainly used in the case of III-V NWs grown by MBE. For instance, Ga is used in the self-assisted growth of GaAs or GaP NWs while In composes the catalyzer of InAs and InP NWs. However, even if the self-assisted growth seems more suitable for the silicon industry, it has to be mentioned that a stronger dependence of the morphology on the growth parameters has been reported[26,27], in comparison with their Au-catalyzed analogues.

### 3.2.2 Theoretical model and introduction to ZB and WZ structures

The cubic Zinc Blende (ZB) and the hexagonal Wurtzite (WZ) are the most common crystal structures observed in III-V semiconductors[28]. However, while only the ZB phase is observed in the case of bulk GaAs for instance, a coexistence of the ZB (Figure 3.2.a and Figure 3.2.b) and WZ (Figure 3.2.c and Figure 3.2.d) phases can be observed for its NWs counterparts, grown using the VLS process.

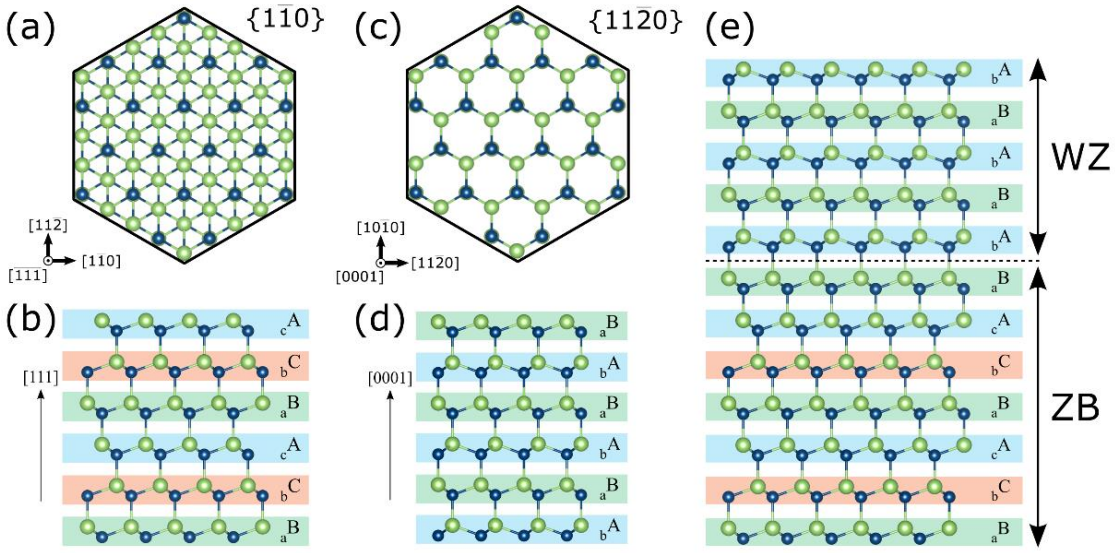


Figure 3.2. Models representing the position of the Ga (green spheres) and As (blue spheres) atoms in III-V semiconductors along the (a) [111] and (b) [1-10] azimuth for the cubic ZB structure, and along the (c) [0001] and (d) [11-20] azimuth for the hexagonal WZ structure. The model shown in (e) illustrates the interface between the ZB and WZ structures, observed along a [1-10] / [11-20] azimuth. Uppercase and lowercase letters on (b), (d) and (e) designate the Ga and As atoms, respectively. The facet orientations are given for the case of self-assisted GaAs NWs. The atomic models represented in this figure were made using the VESTA software[37].

Tuning the nucleation of these crystal structures to control the phase purity of NWs thus appears as one of the main challenges for the fabrication of III-V NWs, and has been intensively studied during the last decades[29–36].

The physical phenomenon at the origin of the nucleation of the ZB and the WZ phases in Au-catalyzed GaAs NWs has been studied intensively and a fundamental model was proposed in 2007 by F. Glas *et al.*[38]. In this work, the cases of a nucleation inside the liquid droplet at the solid-liquid (SL) interface (Figure 3.3.a), and at the triple phase line (TPL) (Figure 3.3.b) are discussed. The nucleation at the SL interface is here presented with the formation of a 2D nucleus island of height *h*, perimeter *P* and upper surface *A*. The change in free enthalpy $\Delta G$ induced by the nucleation process of this 2D nucleus is then equal to:

$$\Delta G = -Ah\Delta\mu + Ph\gamma_{lL} + A(\gamma_{NL} - \gamma_{SL} + \gamma_{SN}), \quad (3.1)$$

where $\Delta\mu$ is the difference of chemical potential for the III-V pairs between the liquid and the solid phases, $\gamma_{lL}$ corresponds to the energy per unit area of the lateral interface between the nucleus and the liquid, and $\gamma_{NL}$, $\gamma_{SL}$ and $\gamma_{SN}$ are the energies per unit area of the upper nucleus-liquid, solid-liquid and solid-nucleus interfaces, respectively (Figure 3.3.a).

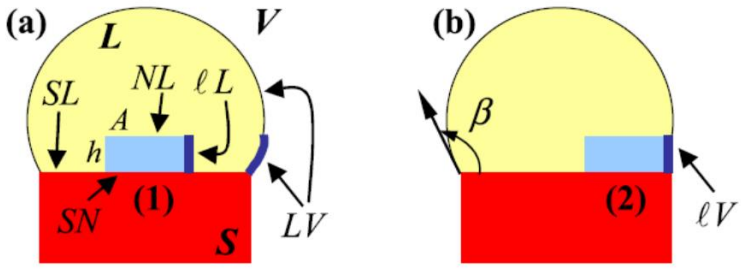


Figure 3.3. (a) Nucleus at the nanowire-liquid interface, with interfaces of interest. (b) Transferring the nucleus to the triple phase line eliminates and creates interfacial areas, indicated by thick lines in, respectively, (a) and (b).[38]

In the case of nucleation inside the liquid droplet, $\gamma_{NL}$ is equal to $\gamma_{SL}$, and the energy $\gamma_{lL}$ remains the same for the ZB and the WZ structures. Only the energy $\gamma_{SN}$ will vary, depending on the surface orientation of the nucleus. Indeed, if the orientation of the solid phase is the same as the nucleus (i.e. ZB-ZB), then $\gamma_{SN}$ = 0, while in the case of different orientations (i.e. WZ-ZB) $\gamma_{SN}$ > 0. These assumptions result in a difference of free enthalpy between ZB and WZ equal to:

$$\Delta G^{WZ} - \Delta G^{ZB} = A\gamma_{SN} > 0. \quad (3.2)$$

The ZB free enthalpy in this case is thus lower than the WZ one, meaning that the ZB structure formation is preferred when the nucleation occurs inside the liquid catalyst droplet. On the other hand, when the nucleation takes place at the TPL, a portion of the nucleus will be in contact with the vapor phase, as shown in Figure 3.3.b. The interface energy contribution of this portion will then switch from $\gamma_{lL}$ to $\gamma_{lV}$, thus

replacing a part $\tau s$ of the liquid-vapor interface by the nucleus-vapor interface of surface *s*. The difference in formation enthalpies between nucleation at the TPL and inside the liquid droplet in therefore express as:

$$\Delta G(\alpha) - \Delta G(0) = \alpha Ph(\gamma_{lV} - \gamma_{lL} - \tau\gamma_{LV}). \quad (3.3)$$

where $\alpha$ corresponds to the fraction of the island perimeter in contact with the vapor phase. The energies per unit area of the nucleus-vapor and liquid-vapor interfaces are designated by $\gamma_{lV}$ and $\gamma_{LV}$, respectively. The case of a nucleus located inside the liquid droplet corresponds to a fraction $\alpha = 0$.

Furthermore, Figure 3.3.b introduces the notion of contact angle $\beta$, which corresponds to the angle between the top facet of the NW and the droplet. This new parameter is used to define the parameter $\tau$ as $\tau = \sin(\beta)$. Consequently, a favorable nucleation at the TPL provides the following inequality:

$$\gamma_{lV} - \gamma_{lL} - \sin(\beta)\,\gamma_{LV} < 0. \quad (3.4)$$

Assuming that $\gamma_{lL} \approx \gamma_{lV}$, and considering $\gamma_{LV}$ as a positive value, it appears that the difference in formation enthalpies is only determined by $\sin(\beta)$. In the case of Au-catalyzed GaAs NWs, a contact angle $90° \leq \beta \leq 125°$ was experimentally observed, leading to $\sin(\beta) \geq 0.82$, hence satisfying the above inequality, confirming the nucleation at the TPL.

Therefore, it is possible to determine the preferable structure, knowing the relative orientation of the nucleus and a certain edge. Indeed, the formation of the WZ structure is favored when the nucleation occurs at the TPL, and when the supersaturation in the droplet exceed a critical value. Inspired by this work, newer and more accurate models were developed based on experimental data, obtained by prototypical growth reactors built inside a TEM[39–41] (Figure 3.4).

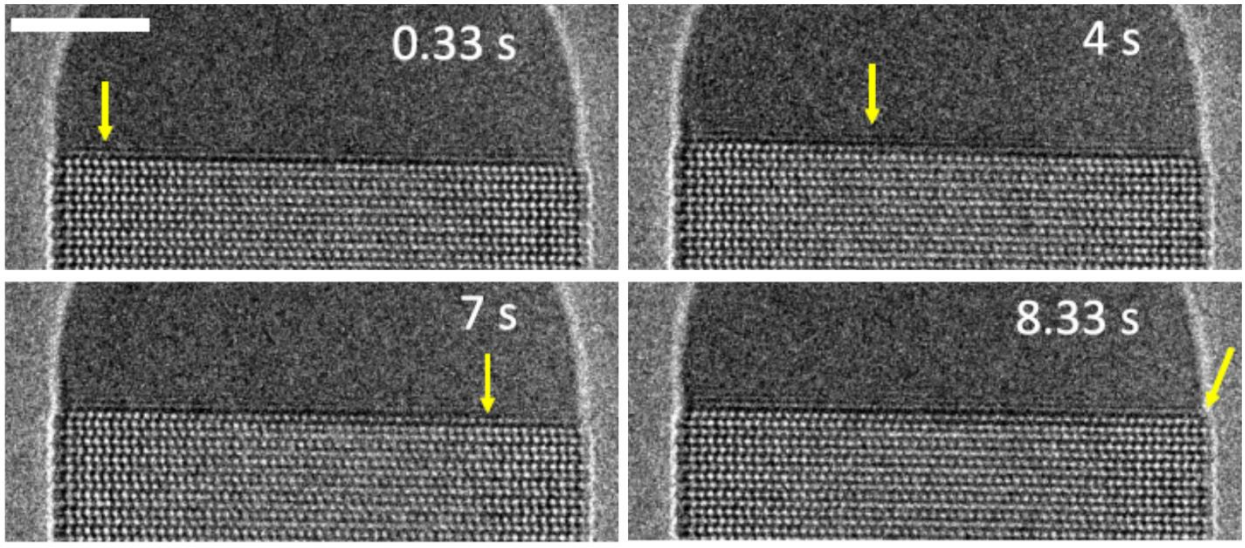


Figure 3.4. Images from an epitaxial growth of NW inside a TEM showing the flow of a single ML step (arrows) during the growth of a GaAs NW with WZ structure. Scale bar is 5 nm. Figure taken and adapted from ref 40.

Thanks to this novel characterization technique, the real-time and real-space observation of the nucleation and growth of single monolayers of GaAs was possible, and confirmed the important dependence of the crystal phase on the droplet volume, and more particularly on its contact angle. Jacobsson *et al* first observed the existence of big droplets with high contact angles $\beta > 125°$ for Au-catalyzed GaAs NWs, in As-poor atmosphere. The presence of a truncated SL interface with the edge facet was then determined, allowing the nucleation of a GaAs monolayer at the position N, inside the droplet, thus leading to the formation of the ZB structure (as shown in Figure 3.5.a and e). Smaller droplets, therefore with low contact angles, were observed in As-rich atmosphere. In this case, a sharp SL interface was reported (Figure 3.5.d), leading to the nucleation at the TPL, and thus to the formation of the WZ phase.

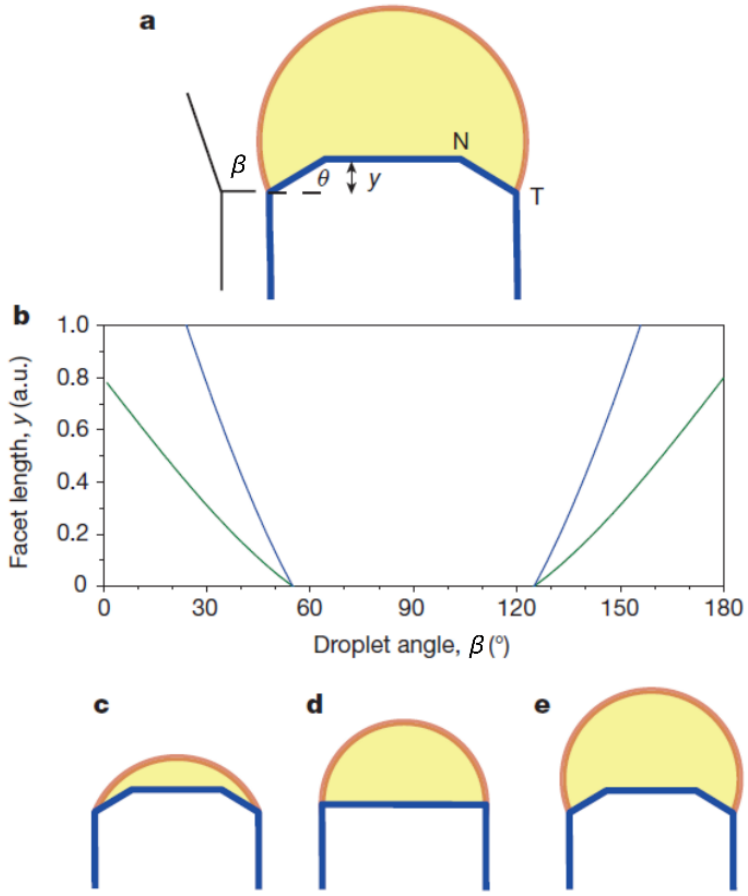


Figure 3.5. (a) Schematic of the NW/droplet interface profile, defining the nucleation site *N*, the triple phase line *T*, the edge facet length *y*, the edge facet angle $\theta$ and the droplet contact angle $\beta$. (b) Graphic representing the edge facet length *y* as a function of the droplet contact angle. The blue and green curves correspond to the low and high supersaturations, respectively. Schematics showing the droplet size and interface profiles with (c) $\beta < 55°$, (d) $55° < \beta < 125°$ and (e) $\beta > 125°$. Figure adapted from ref.[39].

These recent experimental studies reported the existence of a critical angle $\beta_{c1}$ of around 125° in the case of Au-catalyzed GaAs NWs[39,40], above which a transition from the WZ phase to the ZB phase occurs.

#### 3.2.2.1 The self-assisted GaAs nanowire growth

In 2008, Fontcuberta i Morral *et al* reported the first case of self-assisted (Ga-assisted) GaAs NWs, obtained by MBE on GaAs(111) substrates[42] and later on Si substrates. In the case of the growth of self-assisted GaAs NWs on epi-ready Si(111) substrate covered by a thin $SiO_2$ layer, the exposure to a Ga flux tends to form Ga droplets on the oxide layer surface. Then, at high temperature (around 600°C), the Ga droplets start to interact with the $SiO_2$ layer accordingly to the following reactions[43]:

$$SiO_2 + 4\,Ga \rightarrow Si + 2\,Ga_2O, \quad (3.5)$$

$$SiO_2 + Si \rightarrow 2\,SiO, \quad (3.6)$$

$$SiO_2 + 2\,Ga \rightarrow SiO + Ga_2O. \quad (3.7)$$

It is assumed that $Ga_2O$ and SiO desorb at around 600°C, forming holes in the oxide layer and exposing the bare silicon surface of the substrate. Then, Ga droplets are formed in the newly formed holes and act as nucleation seeds to initiate the epitaxial growth of the self-assisted GaAs NWs, as described in the previous paragraphs.

While their Au-catalyzed counterparts exhibit mainly a WZ phase, it has been shown that self-assisted GaAs NWs nucleate mostly in the ZB phase. Nevertheless, it is important to mention that the fundamental model proposed by Glas's group in 2007[38] is still well adapted to the self-assisted growth of NWs. Moreover, recent studies also demonstrate the existence of a critical angle $\beta_{c1}$ in the 125°-127° range above which a transition from the WZ phase to the ZB phase is observed[31,41], and confirmed the presence of truncated facets in self-assisted GaAs NWs with *in situ* TEM measurements[41]. The evidence of a second critical angle $\beta_{c2} \approx 90°$ has also been highlighted[41], below which a transition from the WZ to the ZB phase occurs.

### 3.2.3 The growth protocol

In this section, the experimental process used in our group at INL to grow NWs will be explained. Most of the self-assisted GaAs NWs samples were grown on 1x1 cm² epi-ready Si(111) substrates and tuned via the homemade software EPISURE, ensuring a precise control of the shutters and valves opening, and of the cells and substrate temperatures. The substrates are generally fixed on a molybdenum disks, called molyblocks, with tungsten pins.

The growth protocol used consists of a first step to pre-deposit Ga on the surface of the substrate. During this phase, Ga droplets are formed on the substrate progressively heated at a slope of about 30°C/minute, to a thermocouple temperature $T_{pre\text{-}dep}$ of 400 – 500 °C. The surface of the substrate is then exposed to a Ga flux of 0.5 ML/s for few seconds. The flux of Ga is here quoted in units of equivalent growth rate of GaAs 2D layers, measured by RHEED oscillations on a GaAs(001) substrate[44], as discussed in chapter 2. The substrate temperature is then increased up to a growth temperature $T_{Growth}$ of 500 – 600°C with a slop of around 10 – 15°C/minute. This slow rise of the temperature allows the reduction of the $SiO_2$ by the Ga droplets, thus exposing the bare silicon through holes in the oxide layer. Each increase in temperature is followed by a stabilization phase of 2 minutes aiming at a good thermalization of the substrate. The NW

growth is then initiated with the simultaneous opening of the Ga and $As_4$ shutters. Ga and $As_4$ fluxes of 0.5 ML/s and 1.2 ML/s were used to grow the NWs, respectively, corresponding to a V/III flux ratio of 2.4. The growth was ended by a rapid decreasing of the temperature to preserve the As desorption from the NWs and by closing the $As_4$ and Ga shutters at the same time, to maintain the Ga droplets at the tip of the NWs. The liquid droplet can also be removed through a droplet consumption, occurring under As atmosphere. This last mechanism will be discussed more in depth in the next chapter. A summary of the temperature instruction is provided in Figure 3.6.

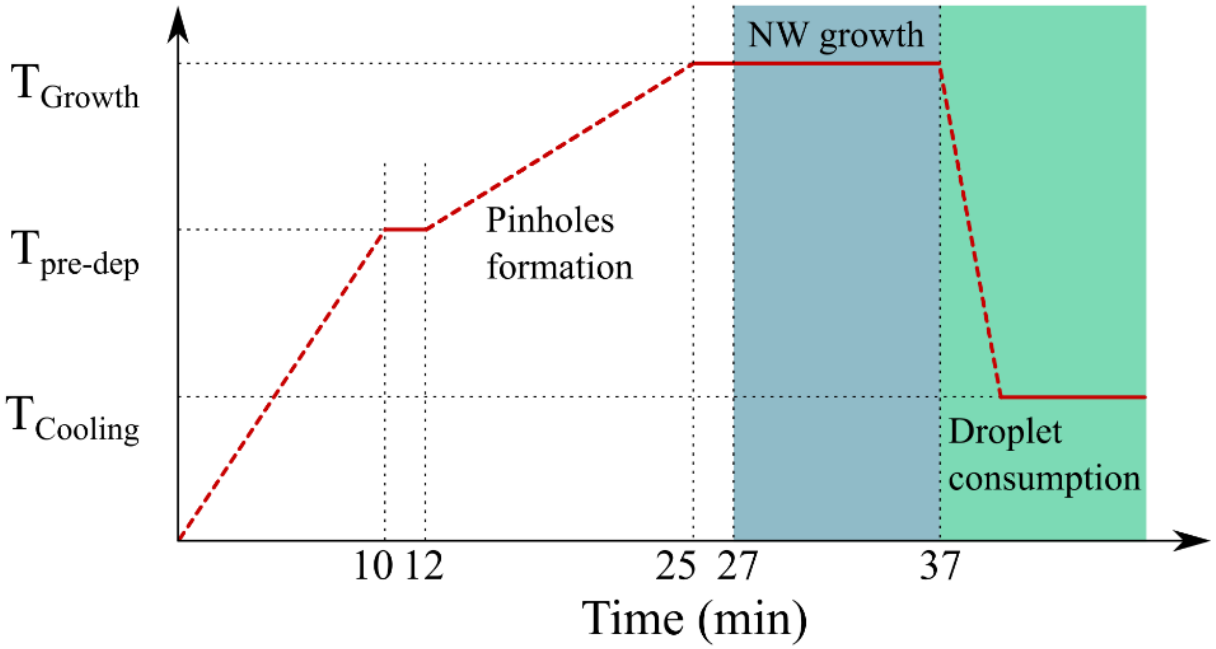


Figure 3.6. Plotted representation of the temperature instruction used for the growth protocol. Blue and green areas highlight the NW growth under Ga and As flux and the droplet consumption under As flux, respectively.

The whole NW growth process is monitored using *in situ* RHEED. Despite its almost exclusive use for the characterization of 2D layers, RHEED can give important information on the crystallinity of NWs. Indeed, electron diffraction can be observed through NW arrays leading to different diagram depending on the incident orientation of the electron beam, as illustrated in Figure 3.7.a – c. The azimuth orientation regarding the NW geometry is illustrated on the simplified schematic of the NW's top view in Figure 3.7.d. An indexed RHEED diagram will be discussed in the following chapter.

For each growth, the Si(111) substrate was sonicated for 5 minutes in acetone and ethanol, dried under nitrogen flow and degassed at 200°C in UHV. The native $SiO_2$ layer was systematically preserved to enable the self-assisted growth[45].

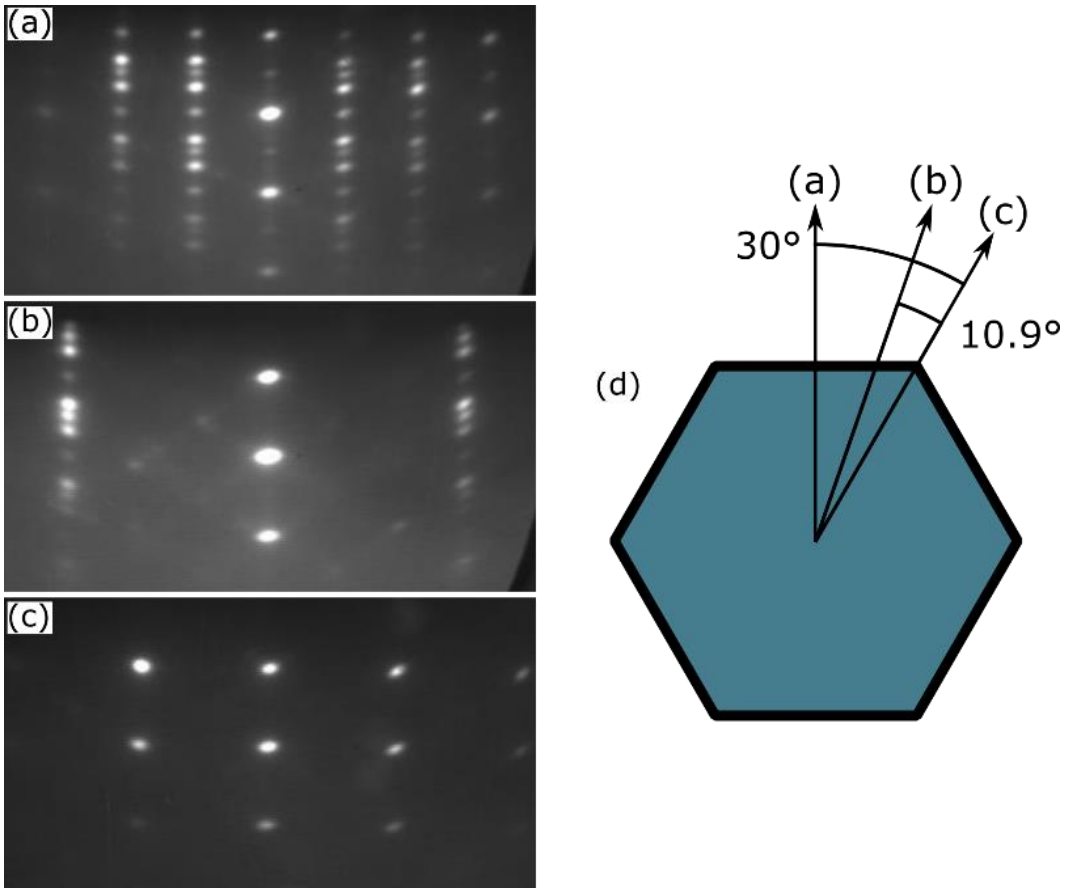


Figure 3.7. RHEED diagrams obtained at the end of the self-assisted GaAs NWs growth along the (a) $[1\bar{1}0]$, (b) $[11\bar{2}]$ and (c) $[12\bar{3}]$ azimuths. (d) Schematic illustration of the top view of a NW, showing the orientation of the different azimuths shown in (a), (b) and (c).

### 3.2.4 Optimization of the growth parameters on the nanowires' morphology

In order to find the most favorable parameters to obtain a high density of NWs and low 2D parasitic crystals, we investigated the role of the growth temperature, as well as of the pre-deposition step on the morphology of NWs. Each growth was characterized by SEM, to measure the lengths, diameters and densities obtained.

#### 3.2.4.1 The impact of the growth temperature

The influence of the growth temperature was first investigated by growing a series of samples at different $T_{Growth}$ from 520°C to 600°C during 10 minutes, with an interval of 20°C. The Ga droplets were pre-deposited at a substrate temperature of 450°C, during 2 seconds with a Ga flux of 0.5 ML/s. The results obtained with this series are reported in the curves Figure 3.8.a – c and shown with SEM images in Figure 3.8.d – m. A large decrease of the parasitic structures can be observed with the increase of the growing temperature (Figure 3.8.i – m). Therefore, after SEM characterization on about twenty NWs for each samples, a slight decrease of the length from about 1.4 µm to about 0.85 µm, as well as a minor increase of the diameters (from 55 nm to 75 nm) and densities (from 1.5 NWs/µm² to 2.6 NWs/µm²) were measured

with the increasing growth temperature. The highest NWs density (about 2.6 NWs/µm²) was obtained with a growth temperature $T_{Growth}$ = 600°C, leading to short NWs (0.8 – 0.9 µm) with high verticality and low parasitic GaAs crystal structures density, exposing quasi-fully the silicon substrate. We thus selected this growth temperature as a reference for the rest of this work.

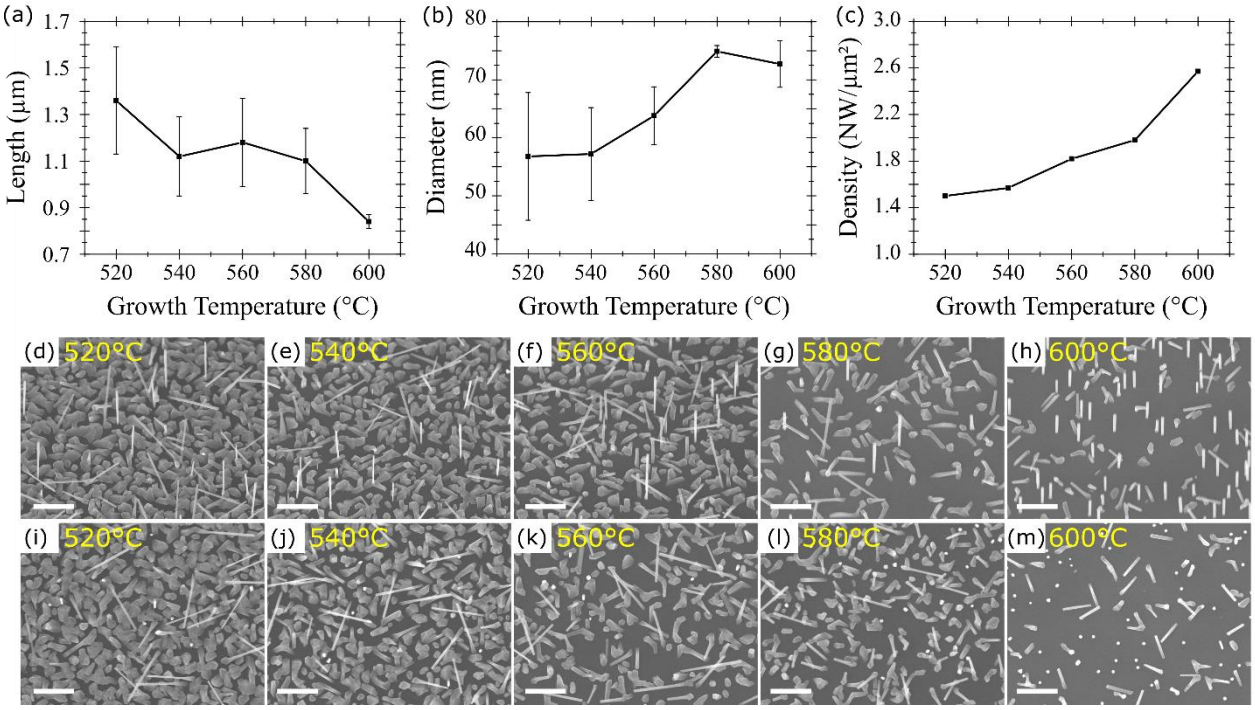


Figure 3.8. Plots showing the evolution of the (a) length, (b) diameter and (c) density of the nanowires as a function of the growth temperature. (d – h) 30° tilted and (i – m) top view SEM images of the nanowires after the growth for different growth temperatures, indicted in yellow. Scales bar are 1 µm. Ga droplets were pre-deposited at a rate of 0.5 ML/s during 2 s at 450°C. The nanowires were grown with a V/III flux ratio of 2.4 with a Ga flux of 0.5 ML/s during 10 min at different growth temperatures.

### 3.2.4.2 The influence of the pre-deposition process

We then investigated the impact of the Ga pre-deposited quantity used to form the Ga droplets on the substrate surface by growing a series of samples with different pre-deposition times, using constant Ga and As fluxes, pre-deposition and growing temperatures. To initiate the growth of this series, we pre-deposited 0.5, 1, 2, 4 and 6 MLs of Ga with a flux of 0.5ML/s at a substrate temperature of 450°C. NWs were grown for 10 minutes at a growth temperature of 600°C. All the samples were then characterized by SEM, with 30°-tilted and top view images, as shown in Figure 3.9.d – h and Figure 3.9.i – m, respectively. The measured lengths, diameters and densities of the NWs are reported in Figure 3.9.a, b, c, respectively. An increase of the NW density, as well as the parasitic structure density, was observed with increasing the Ga quantity pre-deposited. Nonetheless, thinner and shorter NWs were observed for the highest amount of Ga pre-deposited. Indeed, by characterizing the samples using SEM, a decrease of the lengths and diameters from about 1.0 µm to 0.7 µm and from 70 nm to 50 nm, respectively was measured on tens of NWs. This change in morphology could be due to the higher density of holes in the $SiO_2$ oxide layer, leading to a higher

density of NWs once the growth starts. Taking into account the NW morphologies and the density of parasitic structures, we selected a pre-deposition step of 1 ML of Ga deposited in 2 seconds at a rate of 0.5 ML/s.

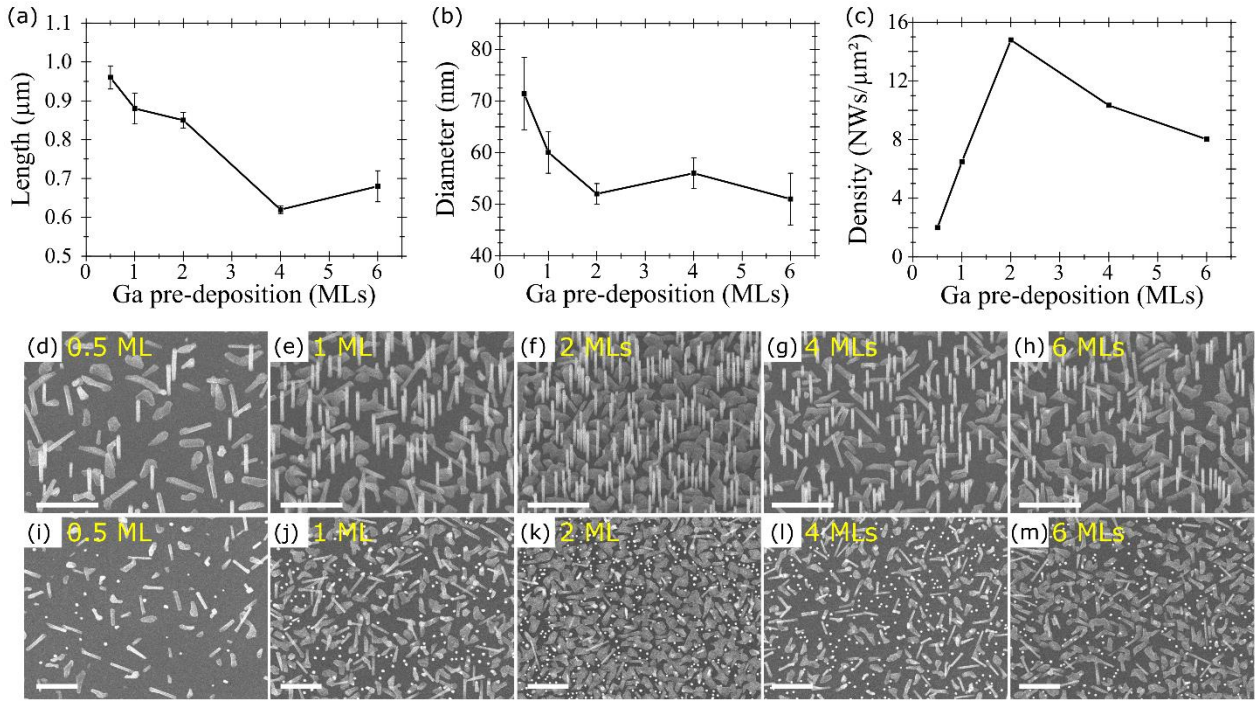


Figure 3.9. Plots showing the evolution of the (a) length, (b) diameter and (c) density of the nanowires as a function of the amount of Ga pre-deposited on the substrate before the growth. (d – h) 30° tilted and (i – m) top view SEM images of the nanowires after the growth for different Ga quantity pre-deposited, indicted in yellow. Scales bar are 1 µm. The Ga droplet were pre-deposited at a rate of 0.5 ML/s during different times, at 450°C. The nanowires were grown with a V/III flux ratio of 2.4 with a Ga flux of 0.5 ML/s during 10 min at 600°C.

Furthermore, after investigating the impact of the amount of Ga pre-deposited on the NW morphology, we studied the influence of the substrate temperature of this step. A series of growths were carried out for 10 minutes each by changing the substrate temperature of the pre-deposition step from 410°C to 490°C, with a 20°C intervals. 1 ML of Ga was pre-deposited and the substrate was heated to a growth temperature of 600°C. After characterization, a low density of NWs (0.5 NW/µm²) was observed for the highest pre-deposition temperature of 490°C (Figure 3.10.g and Figure 3.10.l). This could be explained by a low density of holes in the oxide layer, due to the weak sticking of the Ga atoms on the surface, causing only few Ga droplets. On the contrary, a lower pre-deposition of 410°C led to a high NW density of 8 – 9 NWs/µm² (Figure 3.10.c and Figure 3.10.h), as a result of the high density of smaller Ga droplet on the surface. The low quantity of parasitic structures and the high density of NWs led us to perform the 1 ML Ga pre-deposition at a temperature of 410°C.

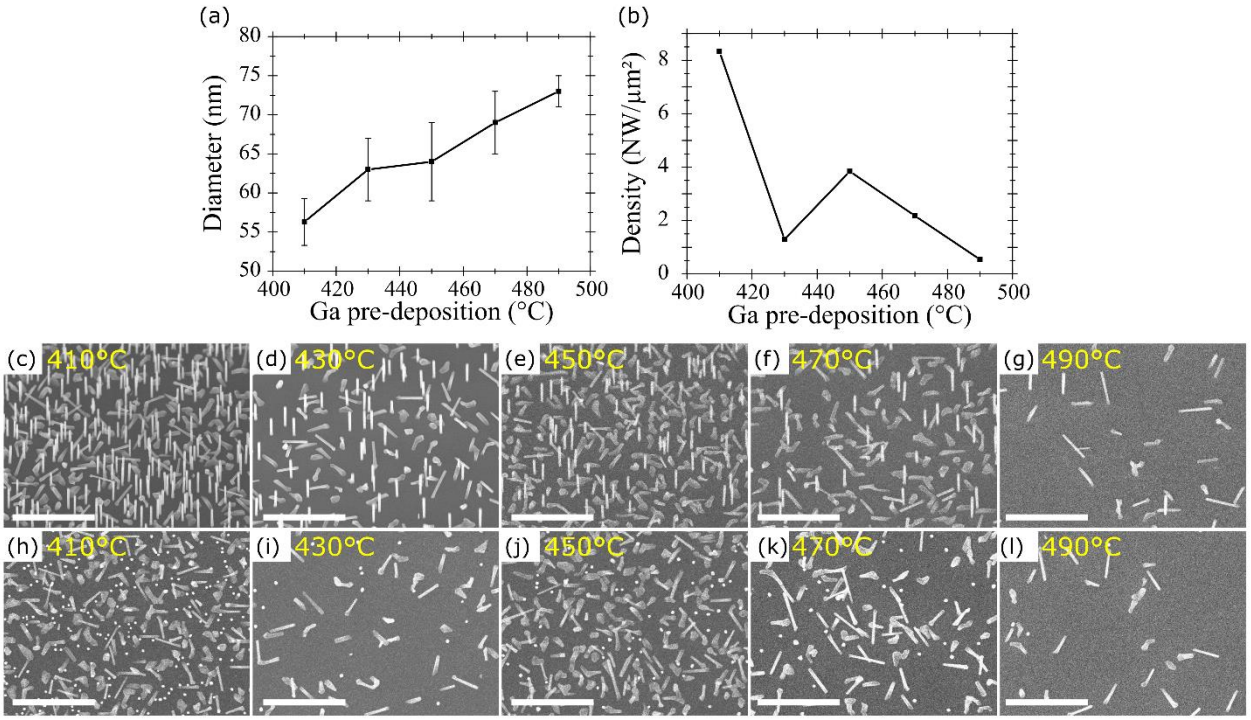


Figure 3.10. Plots showing the evolution of the (a) diameter and (b) density of the nanowires as a function of the pre-deposition temperature. (e – g) 30° tilted and (h – l) top view SEM images of the nanowires after the growth for different Ga pre-deposited temperatures, indicted in yellow. Scales bar are 1 µm. The Ga droplet were pre-deposited at a rate of 0.5 ML/s during 2 s at different pre-deposition temperatures. The nanowires were grown with a V/III flux ratio of 2.4 with a Ga flux of 0.5 ML/s during 10 min at 600°C.

A quick summary of the different series is provided in Table 3.1, highlighting the growth parameters leading to the optimal morphology of NWs, aiming a NW growth rate of about $\nu = 1.7$ nm/s and to the lowest number of parasitic GaAs structures.

Table 3.1. Reported values of the lengths, diameters and densities measured for the different growth parameters. Characterizations performed by SEM on about twenty NWs for each cases. Blue columns highlight the optimal growth parameters.

| | Growth temperature (°C) | | | | | Ga pre-deposition (MLs) | | | | | Ga pre-deposition (°C) | | | | |
|---|---|---|---|---|---|---|---|---|---|---|---|---|---|---|---|
| | 520 | 540 | 560 | 580 | 600 | 0.5 | 1.0 | 2.0 | 4.0 | 6.0 | 410 | 430 | 450 | 470 | 490 |
| Length (µm) | 1.4 | 1.1 | 1.1 | 1.1 | 0.9 | 0.95 | 0.9 | 0.85 | 0.6 | 0.7 | 0.9 | 0.9 | 0.9 | 0.9 | 0.9 |
| Diameter (nm) | 57 | 57 | 60 | 72 | 70 | 70 | 60 | 52 | 55 | 50 | 55 | 62 | 65 | 67 | 72 |
| Density (NWs/µm²) | 1.4 | 1.5 | 1.8 | 2 | 2.6 | 2 | 6 | 14 | 10 | 8 | 8 | 1 | 4 | 2 | 0.5 |
| GaAs crystallites | Very High | High | Few | Few | Almost none | Almost none | Few | High | Few | Few | Few | Almost none | Few | Few | Almost none |

### 3.2.5 Homogeneity on 2 inches' wafers

All the samples discussed in the previous paragraphs were grown on 1 x 1 cm² Si substrates. However, we also decided to investigate the growth on larger 2 inches Si wafers, needed to perform reproducible growth on a larger scale. As explained in 3.2.3 the growth protocol, each increase in temperature is followed by a stabilization of 2 minutes. Repeating the same process in the case of the growth on 2 inches' substrates led to a very high inhomogeneity of the NW morphology and density along the wafer surfaces. Figure 3.11.a – d show 30°-tilted and top view SEM images taken from (a) the edge of the wafer to (d) its center, with 5 mm steps (b) and (c). Indeed, very short 300 nm long NWs with a density of about 4 NWs/µm² was observed at the center of the wafer (Figure 3.11.d), while NWs with a length of about 1.6 µm for a density of around 16 NWs/µm² was obtained on the edge of the wafer (Figure 3.11.a). The maximum density was obtained 5 mm away from the edge, reaching a value of about 32 NWs/µm² (Figure 3.11.b). This huge inhomogeneity was assumed to be the result of a non-optimal thermalization of the substrate, induced by the large surface of the wafer. Furthermore, the molyblock employed for the growth on 1 x 1 cm² consists of a 2 inch' In-free molyblock covered with GaAs with a cavity to receive a 1 x 1 cm² substrate. In this case, it is admitted that the surface of the molyblock thermally interact with the substrate. In the case of the 2 inches' wafer growth, the substrate is only heated *through* the thermocouple filament. To overcome this issue, we decided to increase the stabilization steps from 2 minutes to 15 – 20 minutes. By reproducing the identical growth recipe, with 15 minutes of stabilization before the pre-deposition and the growth, we obtained a high homogeneity on the whole wafer, as shown in the SEM images Figure 3.11.e – h.

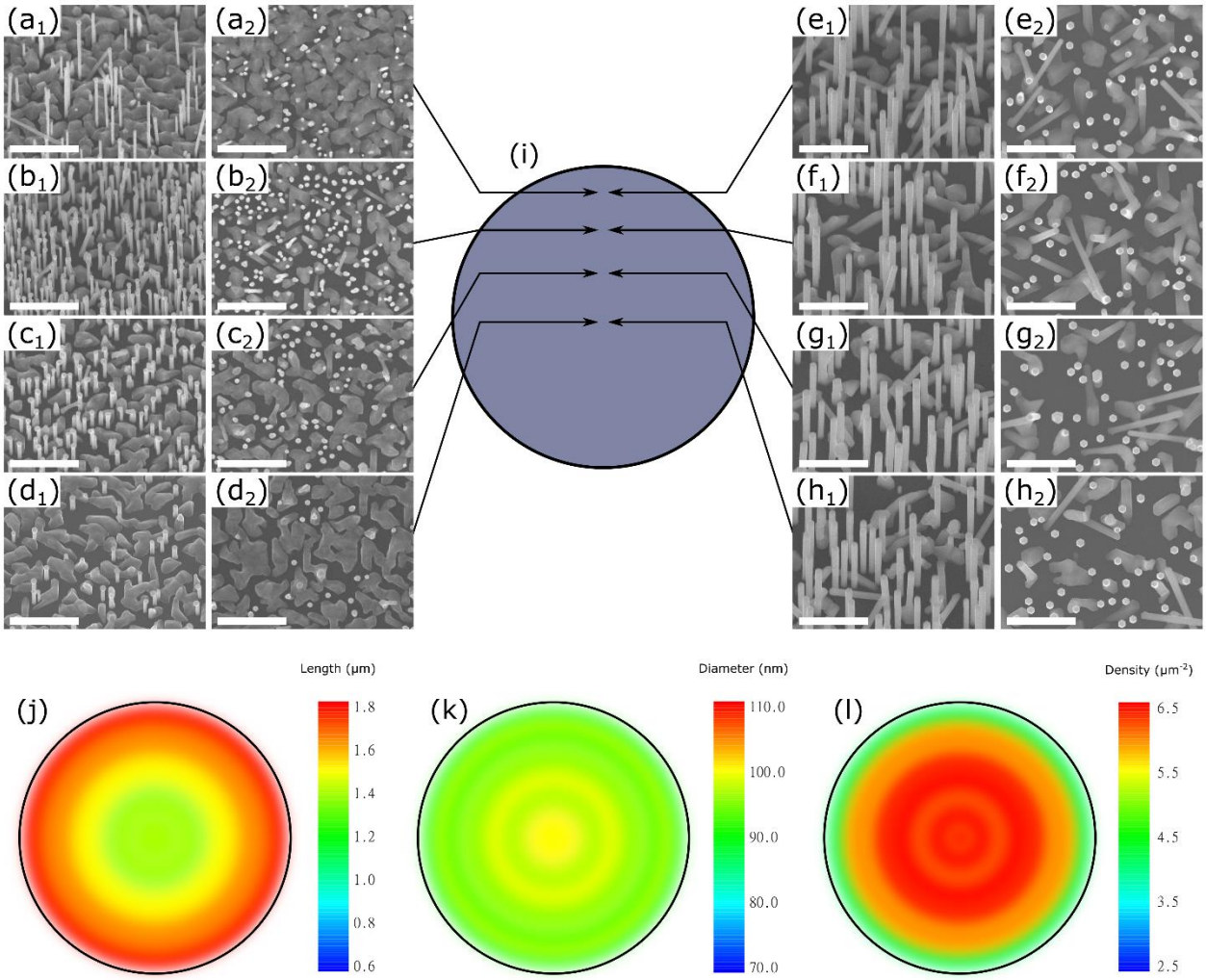


Figure 3.11. SEM images taken from ($a_1$) – ($h_1$) a 30° tilted view and ($a_2$) – ($h_2$) a top view for the samples grown (a) – (d) without and (e) – (h) with the thermalization process. (i) Simplified schema used to indicate the location of the SEM images. Color maps representation of the (j) length, (k) diameter and (l) density distribution of the nanowires on a 2 inches Si wafer using the thermalization process.

In order to obtain a precise information on the length, diameter and density distribution on the 2 inches' wafer, the sample was characterized from the center to the edge, and several 30°-tilted and top view images were taken every millimeter. The results of these characterizations are shown on the color maps displayed in Figure 3.11.j – l. We reduced the length variation down to 200 nm difference between the center and the edge, compared to the 1.3 µm difference obtained without the long stabilizations. In the same way, the density only varies from about 6.5 NWs/µm² on the center to 5 NWs/µm² at the edge.

## 3.3 Conclusion

In this chapter, the growth conditions of the GaAs NWs were studied. Moreover, the fabrication of self-assisted GaAs NWs on Si(111) substrate by MBE was optimized, and the growth parameters were selected to obtain an optimal morphology and density of NWs with length, diameter and density of about 850 nm, 60 nm and 8 NWs/µm², respectively. The impact of different experimental parameters involved during the growth was systematically investigated through several series of self-assisted GaAs NWs growth. Nevertheless, other parameters such as the growth time, the radial growth of shells or the NW growth on patterned substrates were not discussed here, but were well studied, notably in our group[46,47]. An optimization of the growth on 2 inches-large wafers was also performed, allowing to obtain larger homogeneous areas, which can be divided in smaller pieces for further characterizations. Finally, we highlighted the relevance of *in situ* RHEED on the growth of NWs by MBE, thus allowing the real-time distinction between the zinc-blend and wurtzite crystal structures of the III-V NWs. This approach opens a way to control the crystalline phase of the self-assisted GaAs NWs, which will be the subject of Chapter 4.

## 3.4 References

1. Vurgaftman, I., Meyer, J. R. & Ram-Mohan, L. R. Band parameters for III–V compound semiconductors and their alloys. *Journal of Applied Physics* **89**, 5815–5875 (2001).

2. Tanabe, K. A Review of Ultrahigh Efficiency III-V Semiconductor Compound Solar Cells: Multijunction Tandem, Lower Dimensional, Photonic Up/Down Conversion and Plasmonic Nanometallic Structures. *Energies* **2**, 504–530 (2009).

3. *Fundamentals of III-V Semiconductor MOSFETs*. (Springer US, 2010). doi:10.1007/978-1-4419-1547-4.

4. Standing, A. *et al.* Efficient water reduction with gallium phosphide nanowires. *Nat Commun* **6**, 7824 (2015).

5. Gerthsen, D., Ponce, F. A., Anderson, G. B. & Chung, H. F. Lattice Mismatch Effects in Gaas Epitaxy on Si and GaP. *MRS Proc.* **122**, 21 (1988).

6. Chen, L. *et al.* Epitaxial III–V/Si Vertical Heterostructures with Hybrid 2D-Semimetal/Semiconductor Ambipolar and Photoactive Properties. *Adv. Sci.* 2101661 (2021) doi:10.1002/advs.202101661.

7. Mårtensson, T. *et al.* Epitaxial III−V Nanowires on Silicon. *Nano Lett.* **4**, 1987–1990 (2004).

8. Ihn, S.-G., Song, J.-I., Kim, Y.-H. & Lee, J. Y. GaAs nanowires on Si substrates grown by a solid source molecular beam epitaxy. *Appl. Phys. Lett.* **89**, 053106 (2006).

9. Paek, J. H., Nishiwaki, T., Yamaguchi, M. & Sawaki, N. Catalyst free MBE-VLS growth of GaAs nanowires on (111)Si substrate. *Phys. Status Solidi (c)* **6**, 1436–1440 (2009).

10. Fan, Z. *et al.* Three-dimensional nanopillar-array photovoltaics on low-cost and flexible substrates. *Nature Mater* **8**, 648–653 (2009).

11. Zhu, J. *et al.* Optical Absorption Enhancement in Amorphous Silicon Nanowire and Nanocone Arrays. *Nano Lett.* **9**, 279–282 (2009).

12. Muskens, O. L., Rivas, J. G., Algra, R. E., Bakkers, E. P. A. M. & Lagendijk, A. Design of Light Scattering in Nanowire Materials for Photovoltaic Applications. *Nano Lett.* **8**, 2638–2642 (2008).

13. Tsakalakos, L., Balch, J. & Fronheiser, J. Silicon nanowire solar cells. *Appl. Phys. Lett.* 4.

14. Tang, Y. B. *et al.* Vertically Aligned p-Type Single-Crystalline GaN Nanorod Arrays on n-Type Si for Heterojunction Photovoltaic Cells. *Nano Lett.* **8**, 4191–4195 (2008).

15. Colombo, C., Heiβ, M., Grätzel, M. & Fontcuberta i Morral, A. Gallium arsenide p-i-n radial structures for photovoltaic applications. *Appl. Phys. Lett.* **94**, 173108 (2009).

16. Vettori, M. *et al.* Growth optimization and characterization of regular arrays of GaAs/AlGaAs core/shell nanowires for tandem solar cells on silicon. *Nanotechnology* **30**, 084005 (2019).

17. Hwang, Y. J., Boukai, A. & Yang, P. High Density n-Si/n-$TiO_2$ Core/Shell Nanowire Arrays with Enhanced Photoactivity. *Nano Lett.* **9**, 410–415 (2009).

18. Foley, J. M., Price, M. J., Feldblyum, J. I. & Maldonado, S. Analysis of the operation of thin nanowire photoelectrodes for solar energy conversion. *Energy Environ. Sci.* **5**, 5203–5220 (2012).

19. Kamimura, J., Bogdanoff, P., Ramsteiner, M., Geelhaar, L. & Riechert, H. Photoelectrochemical properties of InN nanowire photoelectrodes for solar water splitting. *Semicond. Sci. Technol.* **31**, 074001 (2016).

20. Liu, S., Han, C., Tang, Z.-R. & Xu, Y.-J. Heterostructured semiconductor nanowire arrays for artificial photosynthesis. *Mater. Horiz.* **3**, 270–282 (2016).

21. Xie, G. *et al.* GaP/GaPN core/shell nanowire array on silicon for enhanced photoelectrochemical hydrogen production. *Chinese Journal of Catalysis* **41**, 2–8 (2020).

22. Cui, F. *et al.* Robust Protection of III–V Nanowires in Water Splitting by a Thin Compact $TiO_2$ Layer. *ACS Appl. Mater. Interfaces* **13**, 30950–30958 (2021).

23. Lewis, N. S. Developing a scalable artificial photosynthesis technology through nanomaterials by design. *Nature Nanotech* **11**, 1010–1019 (2016).

24. Tchernycheva, M., Harmand, J. C., Patriarche, G., Travers, L. & Cirlin, G. E. Temperature conditions for GaAs nanowire formation by Au-assisted molecular beam epitaxy. *Nanotechnology* **17**, 4025–4030 (2006).

25. Breuer, S. *et al.* Suitability of Au- and Self-Assisted GaAs Nanowires for Optoelectronic Applications. *Nano Lett.* **11**, 1276–1279 (2011).

26. Krogstrup, P. *et al.* Structural Phase Control in Self-Catalyzed Growth of GaAs Nanowires on Silicon (111). *Nano Lett.* **10**, 4475–4482 (2010).

27. Dayeh, S. A., Yu, E. T. & Wang, D. III−V Nanowire Growth Mechanism: V/III Ratio and Temperature Effects. *Nano Lett.* **7**, 2486–2490 (2007).

28. Yeh, C.-Y., Lu, Z. W., Froyen, S. & Zunger, A. Zinc-blende–wurtzite polytypism in semiconductors. *Phys. Rev. B* **46**, 10086–10097 (1992).

29. Yu, X. *et al.* Evidence for Structural Phase Transitions Induced by the Triple Phase Line Shift in Self-Catalyzed GaAs Nanowires. *Nano Lett.* **12**, 5436–5442 (2012).

30. Dubrovskii, V. G. *et al.* New Mode of Vapor−Liquid−Solid Nanowire Growth. *Nano Lett.* **11**, 1247–1253 (2011).

31. Kim, W. *et al.* Bistability of Contact Angle and Its Role in Achieving Quantum-Thin Self-Assisted GaAs nanowires. *Nano Lett.* **18**, 49–57 (2018).

32. Krogstrup, P. *et al.* Structural Phase Control in Self-Catalyzed Growth of GaAs Nanowires on Silicon (111). *Nano Lett.* **10**, 4475–4482 (2010).

33. Ambrosini, S., Fanetti, M., Grillo, V., Franciosi, A. & Rubini, S. Vapor-liquid-solid and vapor-solid growth of self-catalyzed GaAs nanowires. *AIP Advances* **1**, 042142 (2011).

34. Krogstrup, P. *et al. In-situ* x-ray characterization of wurtzite formation in GaAs nanowires. *Appl. Phys. Lett.* **100**, 093103 (2012).

35. Rieger, T., Lepsa, M. I., Schäpers, T. & Grützmacher, D. Controlled wurtzite inclusions in self-catalyzed zinc blende III–V semiconductor nanowires. *Journal of Crystal Growth* **378**, 506–510 (2013).

36. Munshi, A. M. *et al.* Crystal phase engineering in self-catalyzed GaAs and GaAs/GaAsSb nanowires grown on Si(111). *Journal of Crystal Growth* **372**, 163–169 (2013).

37. Momma, K. & Izumi, F. *VESTA 3* for three-dimensional visualization of crystal, volumetric and morphology data. *J Appl Crystallogr* **44**, 1272–1276 (2011).

38. Glas, F., Harmand, J.-C. & Patriarche, G. Why Does Wurtzite Form in Nanowires of III-V Zinc Blende Semiconductors? *Phys. Rev. Lett.* **99**, 146101 (2007).

39. Jacobsson, D. *et al.* Interface dynamics and crystal phase switching in GaAs nanowires. *Nature* **531**, 317–322 (2016).

40. Harmand, J.-C. *et al.* Atomic Step Flow on a Nanofacet. *Phys. Rev. Lett.* **121**, 166101 (2018).

41. Panciera, F. *et al.* Phase Selection in Self-catalyzed GaAs Nanowires. *Nano Lett.* **20**, 1669–1675 (2020).

42. Fontcuberta i Morral, A., Colombo, C., Abstreiter, G., Arbiol, J. & Morante, J. R. Nucleation mechanism of gallium-assisted molecular beam epitaxy growth of gallium arsenide nanowires. *Appl. Phys. Lett.* **92**, 063112 (2008).

43. Madsen, M. H., Aagesen, M., Krogstrup, P., Sørensen, C. & Nygård, J. Influence of the oxide layer for growth of self-assisted InAs nanowires on Si(111). *Nanoscale Res Lett* **6**, 516 (2011).

44. Rudolph, D. *et al.* Direct Observation of a Noncatalytic Growth Regime for GaAs Nanowires. *Nano Lett.* **11**, 3848–3854 (2011).

45. Fontcuberta i Morral, A. *et al.* Prismatic Quantum Heterostructures Synthesized on Molecular-Beam Epitaxy GaAs Nanowires. *Small* **4**, 899–903 (2008).

46. Xin, G. Growth of semiconductor (core) / functional oxide (shell) nanowires: application to photoelectrochemical water splitting. 171.

47. Vettori, M. *et al.* Growth optimization and characterization of regular arrays of GaAs/AlGaAs core/shell nanowires for tandem solar cells on silicon. *Nanotechnology* **30**, 084005 (2019).

# 4 The monitoring of crystal phases in self-assisted GaAs nanowire growth by *in situ* RHEED

## Chapter contents



### 4.1 Introduction

Since the establishment of the fundamental model proposed by F. Glas's group in 2007[1] on the nucleation of the cubic ZB and hexagonal WZ phases occurring during the growth of Au-catalyzed GaAs NWs, and the first growth of self-assisted ZB GaAs NWs achieved by A. Fontcuberta i Morral's team in 2008[2], a wide interest has been paid to the real-time observation of the nucleation of these phases in order to control their formation in NWs, which exhibit different electronic[3], optical[4–6], mechanical[7], thermoelectric[8] and piezoelectric[9,10] properties. These physical properties, tunable through the control of the ZB and WZ crystal

structures of the self-assisted GaAs NWs, thus open the way to the development of a wide range of NW heterostructures without foreign elements, which is particularly attractive for the fabrication of devices.

The hexagonal WZ structure is often observed for Au-catalyzed III-V NWs, while the cubic ZB phase is mostly obtained in the case of self-assisted ones. However, the formation of a small WZ segment is usually observed at the top of the NWs, when the catalyst droplets are consumed at the end of the growth, by exposing them to an As flux[11–17]. The ability to control and form on-demand the WZ phase in self-assisted GaAs NWs has thus become a major challenge in the NW community. As discussed in chapter 3, the formation of the ZB or WZ phases in GaAs NWs is dictated by the nucleation of the new ML, and more particularly by its localization, either inside the liquid droplet or at the TPL, respectively[12,15,18–20]. The localization of nucleation depends on the size of the catalyst droplet, and thus on its contact angle $\beta$ formed regarding the top facet of the NW[21–24]. The existence of two critical angles $\beta_{c1}$ and $\beta_{c2}$, between which the formation of WZ is observed and equal to about 125° and 90°, respectively, was then reported. The ZB nucleation occurs when the droplet size leads to angles larger than $\beta_{c1}$ or smaller than $\beta_{c2}$.

However, most of the *in situ* and real time tools used to characterize and tune the crystal structures of the self-assisted GaAs NWs during the growth are often unique and only available in few selected laboratories, such as *in situ* XRD[25] or *in situ* TEM[21,23,24]. The aforementioned prototypical instruments are undeniably primordial for the experimental understanding of the growing mechanisms involved on individual objects, but are not adaptable to the case of the MBE growth on large substrates. Nevertheless, the RHEED technique presented in chapter 2 is commonly coupled with MBE reactors and can be used as a powerful tool to characterize and follow the structural evolution during the growth of NWs using the distinct ZB and WZ diffraction diagrams, as discussed in chapter 3. Despite this capability, only a few recent studies reported RHEED observations applied to self-assisted GaAs NWs growth[17,26–28]. Hence, we decided to investigate the use of the RHEED technique to monitor in real time the growth of the cubic ZB and hexagonal WZ phases in self-assisted GaAs NWs.

This chapter will be dedicated to the results obtained in the framework of our already-published studies[29] and will be divided in two main parts. Firstly, our experimental results showing the RHEED analysis and control operated to form the WZ structure will be presented, while the second part will be focused on the growth model developed to approximate the value of the contact angle $\beta_{c1}$.

The MBE growths and RHEED interpretations presented in this chapter were realized by myself. The TEM images were obtained by Gilles Patriarche from the Centre de Nanosciences et de Nanotechnologies, Palaiseau. The growth model was developed in collaboration with Michel Gendry from INL.

## 4.2 RHEED applied to the nanowire growth

All the NWs presented in this chapter were synthetized on 1 x 1 cm² Si(111) substrates, and were grown following the growth procedure described in chapter 3. The whole growth process was systematically monitored used *in situ* RHEED. Indeed, a RHEED diagram can provide a pattern showing distinctly the

contribution of both ZB and WZ phases, along the appropriate azimuth. Figure 4.1 shows the typical RHEED pattern measured along the $[1\bar{1}0]$ azimuth of self-assisted GaAs NWs. The indexed WZ and ZB (including the twinned ZB) spots are superimposed on the image, highlighted with the red squares and green circles, respectively. The position of each spots is in agreement with the epitaxial growth of NWs on Si(111). Indeed, the GaAs [111] and $[1\bar{1}0]$ axes for the ZB and the GaAs [0001] and $[10\bar{1}0]$ axes for the WZ are parallel to the Si [111] and $[1\bar{1}0]$ axis, respectively.

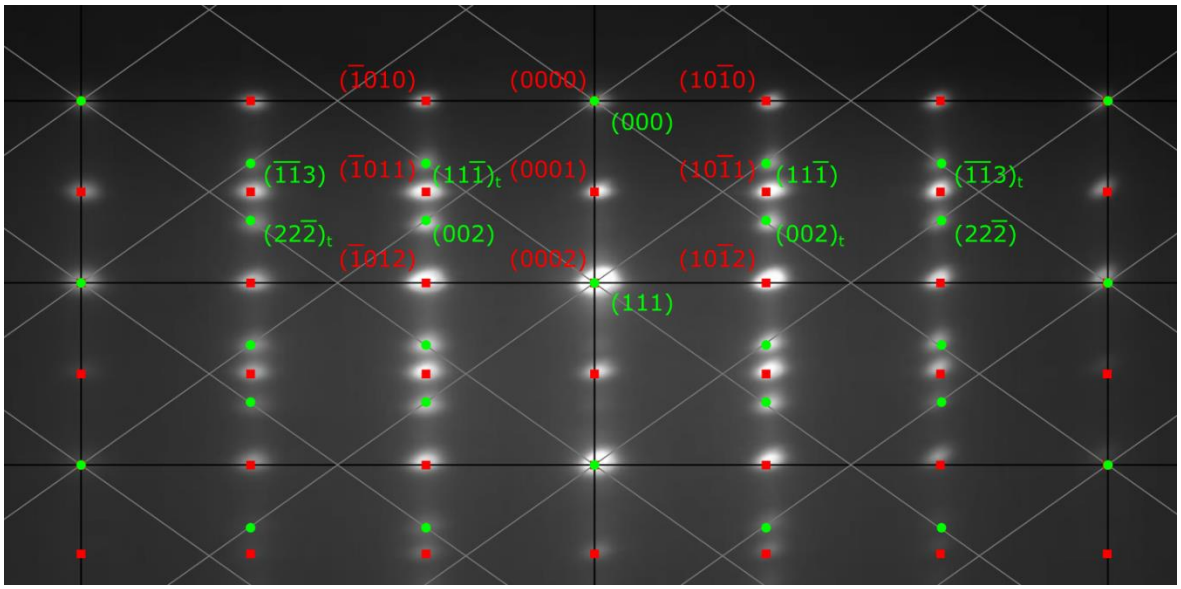


Figure 4.1. RHEED pattern of GaAs NWs recorded along the $[1\bar{1}0]$ azimuth, where the ZB and WZ spots are visible. An indexed diagram is surimposed on the RHEED pattern, showing the two ZB variants plans (green circles) and the WZ plans (red squares).[29]

Despite the fact that self-assisted GaAs NWs grow in the ZB phase, it has to be noticed that a contribution of the WZ structure is visible on the RHEED diagram shown in Figure 4.1. Indeed, a short WZ segment responsible of the RHEED WZ spots, can be synthetized at the end of the growth by consuming the liquid catalyst. This Ga droplet consumption occurs when the Ga shutter is closed, supplying only the As flux, thus leading to a progressive diminution of the droplet size and of the contact angle, as illustrated in the simplified schematic in Figure 4.2.a. The formation of this small WZ segment is visible in the RHEED diagram. This phenomenon is illustrated in Figure 4.2.c and Figure 4.2.d, showing the patterns obtained during the growth (where only the ZB spots are visible), and after the droplet consumption (where the WZ and ZB spots are observed), respectively.

Therefore, by observing the evolution of this RHEED diagram during the entire growth of self-assisted GaAs NWs using a framerate of 30 images per seconds, the real-time detection of the WZ formation becomes accessible. Indeed, stopping the rotation of the sample during the growth allows the measurement of the intensities evolution of specific diffraction spots, namely the $(10\bar{1}2)$ WZ and $(002)_t$ ZB spots, providing information about the structural evolution of the self-assisted GaAs NWs, using the RHEED patterns.

Figure 4.2.b shows the evolution of the $\frac{I_{ZB}}{I_{ZB}+I_{WZ}}$ (black curve) and $\frac{I_{WZ}}{I_{ZB}+I_{WZ}}$ (red curve) intensity ratios (IRs) as a function of the growth time. The parameters $I_{ZB}$ and $I_{WZ}$ represents the ZB and WZ measured spot intensities, respectively. These IRs will be respectively referred as $IR_{ZB}$ and $IR_{WZ}$ in the rest of this chapter. The blue area corresponds to the standard growth, under Ga and As fluxes, associated to the stages (i) of Figure 4.2.a.

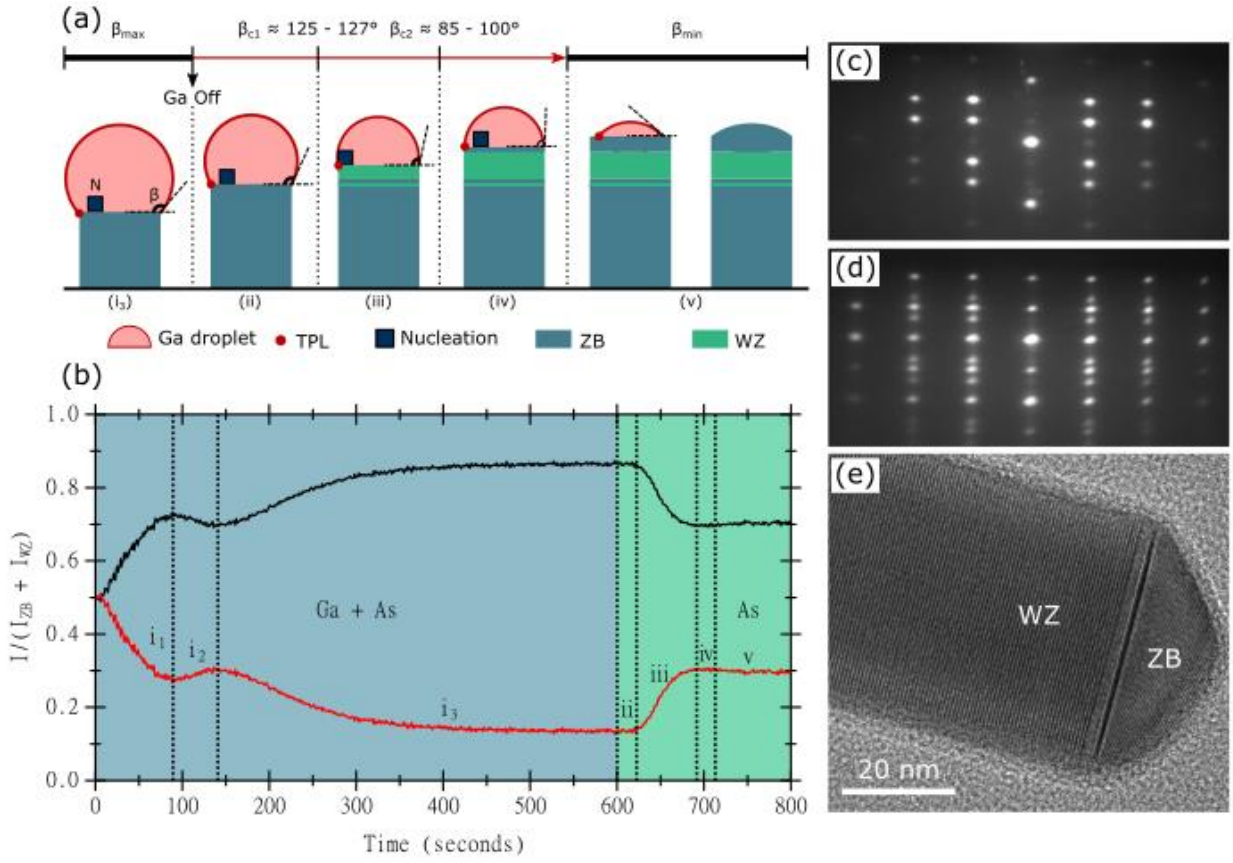


Figure 4.2. (a) Schematic of the Ga catalyst droplet evolution: ($i_3$) during the growth of the GaAs NWs, with a constant amount of Ga and As supplied to the droplet, leading to a wetting angle $\beta = \beta_{max}$ larger than $\beta_{c1}$. The ZB phase is nucleated during this period. After interrupting the Ga flux, a decrease of the droplet volume is observed, leading first to (ii) a nucleation inside the droplet (ZB phase), until (iii) the wetting angle $\beta$ became lower than $\beta_{c1}$, leading to a nucleation at the TPL and thus to a transition zone *t* with a ZB/WZ phase mixing, followed by a pure-WZ section. Then, the wetting angle continues to decrease, becoming lower than $\beta_{c2}$, inducing (iv) a nucleation inside the droplet (short ZB segment) until (v) it reached $\beta_{min}$, thus ending the growth with the final consumption of the droplet. (b) $IR_{ZB}$ (black curve) and $IR_{WZ}$ (red curve) as a function of the growth time. The growth under Ga and As flux is shown in blue while the consumption of the Ga droplet is shown in green. RHEED pattern recorded along the $[1\bar{1}0]$ azimuth (c) during the NW growth and (d) after ending the growth by interrupting the Ga flux. The RHEED diagrams in (c) and (d) show the ZB pattern and the mixed ZB / WZ pattern, respectively. (e) TEM image of the top of a nanowire along the $[1\bar{1}0]$ zone axis, showing the WZ and ZB structure induced by the consumption of the Ga catalyst droplet.

Due to the absence of NWs at the time $t$ = 0 sec, $IR_{ZB}$ and $IR_{WZ}$ are equal to 0.5. At this moment, the intensities measured correspond to the diffraction lines of the Si(111) substrate surface. As soon as the Ga and As fluxes are supplied to the surface, an increase of $IR_{ZB}$, and subsequently a decrease of $IR_{WZ}$ is observed, mainly due to the growth of parasitic nanocrystals, in the ZB phase. After about 10-20 seconds[26], the nucleation and growth of the NWs starts (zone ($i_1$)). After about 400 seconds of growth, the IRs tend to stabilize to values close to 1 and 0 for $IR_{ZB}$ and $IR_{WZ}$, respectively (zone ($i_3$)). This stabilization indicates that the probed parts of the NWs are entirely or quasi-entirely in the ZB phase (stage ($i_3$) in Figure 4.2.a).

The growth was then interrupted after 600 seconds by closing the Ga shutter. The consumption of the droplet under As atmosphere was then observed, leading to the sequence schematized in stages (ii) to (v) of Figure 4.2.a. A delay was observed, highlighted by zone (ii), between the closing of the Ga shutter and the beginning of the $IR_{WZ}$ increase. Indeed, this delay of about 20 seconds, can be attributed to the time needed for the droplet contact angle to reach its critical value $\beta_1$ = 125°–127 °, responsible for the WZ phase nucleation (stage (ii) in Figure 4.2.a). An increase of the $IR_{WZ}$ was then observed for about 70 seconds (zone (iii), corresponding to stage (iii) in Figure 4.2.a) associated first to the growth of a mixed-ZB/WZ segment, followed by a pure-WZ segment. Finally, a slight increase of the $IR_{ZB}$ (zone (iv), corresponding to stage (iv) in Figure 4.2.a) is observed, and is the consequence of a final short ZB segment growth. This portion is induced by a contact angle lower than the critical value $\beta_2$ of about 90°, as illustrated in stage (v) of Figure 4.2.a. It should be noted that this final transition from the WZ to the ZB phase is abrupt without any structural defects, as shown on the HRTEM image provided in Figure 4.2.e. The zone (v) plotted at the very end of the graphic is associated with the end of the NW growth, when $\beta = \beta_{min}$, with the final consumption of the Ga droplet. These measurements obtained *via* RHEED analysis are perfectly in line with the structural evolution commonly observed on NWs by TEM characterizations. Therefore, we can safely associate these IR variations with the size and contact angle modifications occurring on the Ga droplets, as illustrated in Figure 4.2.a.

We note here that the density and the length of the NWs, as well as the incidence angle of the electron beam regarding the substrate surface, can affect the RHEED diagram obtained during the growth due to shadowing effects. Indeed, the depth probed by the electron beam could be modified by all these different parameters. However, in our specific configuration, the NWs were characterized after a 10-minute growth, which corresponds to a length of about 1.0 – 1.1 µm and a diameter of about 50 nm, for a density of 1 NW/µm², and led to an estimated probed depth around 400 to 500 nm. We estimated this depth using the IR curves obtained during the growth. Indeed, an increase of the $IR_{WZ}$ was observed 100 seconds after the beginning of the growth, during about 40 seconds (zone ($i_2$) in Figure 4.2.a), induced by the formation of short mixed-ZB/WZ and pure-WZ segments. These short segments could then be used to estimate the depth probed by the electron beam. Indeed, the $IR_{WZ}$ peak reached a maximum once the WZ segment ended, and when the ZB to WZ transition occurred (Figure 4.3.a). Then these WZ spots slowly vanished (Figure 4.3.b) until their complete disappearance once the segment was no longer probed by the electron beam (Figure 4.3.c). Approximatively 290 seconds were needed to observe a complete disappearance of the RHEED WZ spots induced by this segment, corresponding to about 400 to 500 nm, given the NW growth rate.

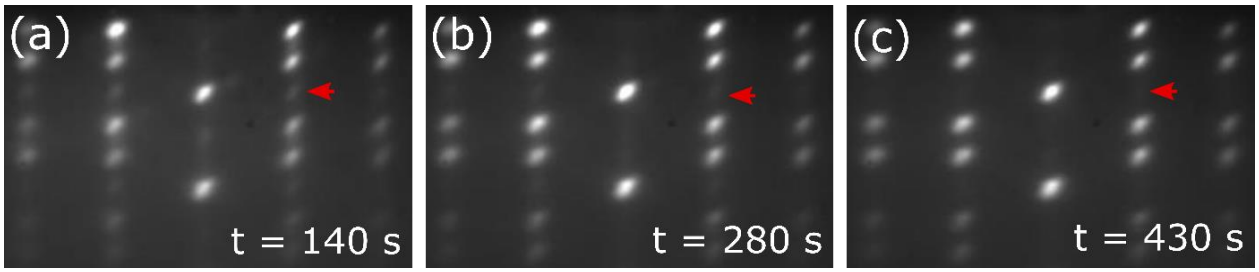


Figure 4.3. RHEED snapshots taken during the growth at (a) *t* = 140 seconds, (b) *t* = 280 seconds and (c) *t* = 430 seconds. Red arrows point the $(10\bar{1}2)$ WZ spot.

However, the purpose of this study was to monitor the evolution of the RHEED diagram during the MBE growth of self-assisted GaAs NWs. In particular, we aimed to correlate the time dependence of the RHEED spots with the nucleation of the different crystal phases. Hence, the shadowing effects have only a slight influence on our analysis.

### 4.2.1 The Zinc Blende / Wurtzite alternation

After demonstrating that RHEED patterns provide real-time information on the crystal structure evolution of the self-assisted GaAs NWs during growth, we used this possibility to control the formation of a WZ segment, inside ZB NWs. To do so, we decided to mimic the droplet consumption phenomenon, by interrupting the incoming Ga flux for a short period. The purpose here was to estimate an appropriate time to reduce the size of the Ga droplets, inducing the nucleation of a WZ phase, without totally consuming the catalysts. Based on the previous results, the Ga flux was interrupted for 60 seconds after about 240 seconds of growth, in order to avoid the complete consumption of the droplets. The expected modifications of the Ga droplet are depicted in Figure 4.4.a, and the IR curves obtained during this growth are reported Figure 4.4b, showing $IR_{ZB}$ and $IR_{WZ}$ with the black and red curves, respectively.

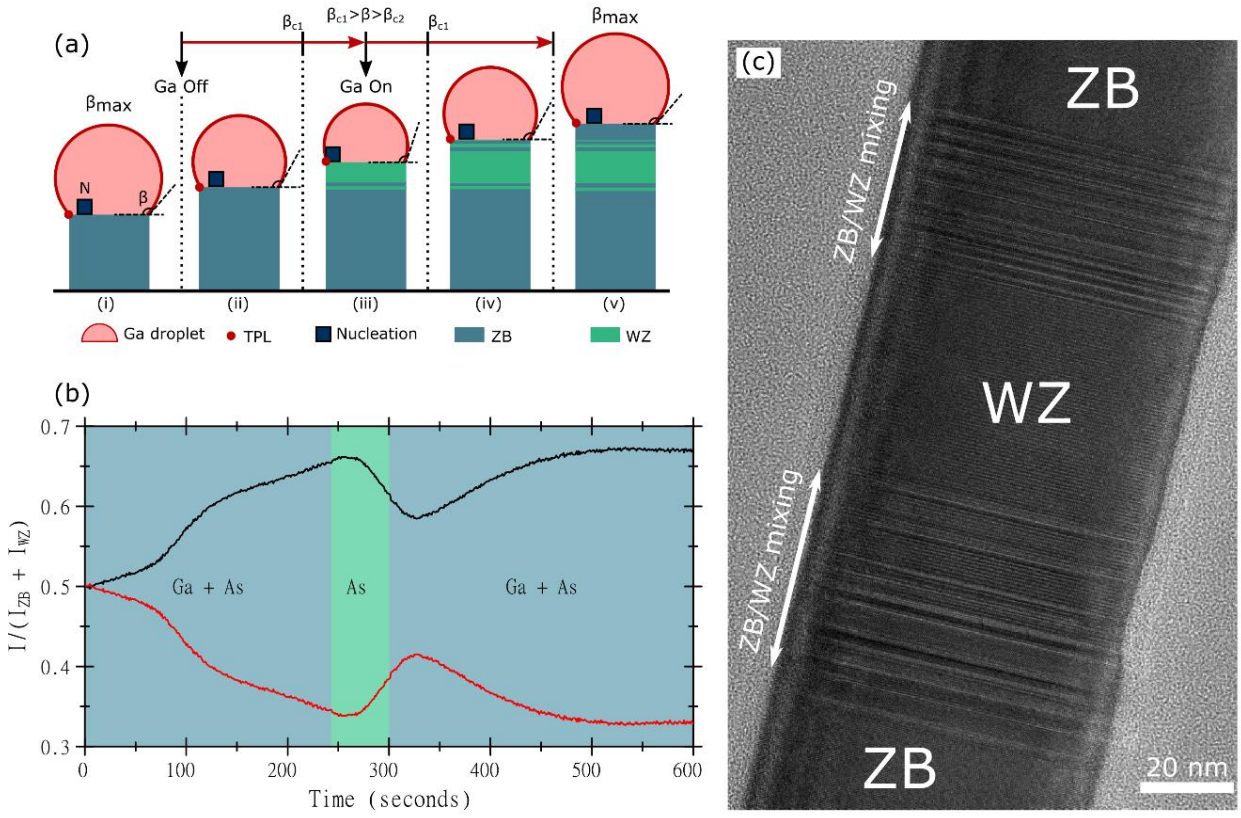


Figure 4.4. Schematic of the Ga droplet evolution and corresponding crystal structure during the growth, showing: (i) the growth of GaAs NWs under Ga and As flux, with a wetting angle $\beta = \beta_{max}$, leading to a nucleation inside the droplet and (ZB phase). The Ga flux was then interrupted, leading to a (ii) decrease of the wetting angle with a nucleation inside the droplet (ZB phase), followed by (iii) a nucleation at the TPL (ZB/WZ mixing followed by pure-WZ) once $\beta < \beta_{c1}$. The droplet was then re-exposed to a Ga flux, leading to the progressive increase of the wetting angle up to (iv, v) $\beta_{max}$. (b) $IR_{ZB}$ (black curve) and $IR_{WZ}$ (red curve) as a function of the growth time. The growth under Ga and As flux is shown in blue while the green part represents the growth under As only. (c) HRTEM image along the $[1\bar{1}0]$ zone axis of the WZ insertion grown in the ZB GaAs NW.[29]

The ZB structure was first formed during the growth of the NWs (first blue area), followed by the interruption of the Ga flux for 1 minute after 4 minutes of growth (green area). The Ga flux was then re-supplied to the droplet by re-opening the Ga shutter. A delay was observed between the interruption of the Ga flux and the minimum of the $IR_{WZ}$. In order to precisely estimate the duration of the WZ nucleation, the first derivative of the $IR_{WZ}$ between 200 and 400 seconds was plotted (Figure 4.5). The transitions from the ZB to the WZ phases and from the WZ to the ZB phases are indicated by the two vertical black lines, corresponding to the first derivative equals to zero. Thus, the first latency was estimated to about 17 seconds and corresponds to the time needed for the droplet to go from a maximal contact angle $\beta_{max} \approx 135° - 140°$ to the critical angle $\beta_{c1}$. Similarly, the second delay of 26 seconds was observed to go from a local minimum contact angle $\beta_{Lmin}$, reached the instant before the re-opening of the Ga flux, to the critical angle $\beta_{c1}$ necessary to allow the transition to the ZB phase.

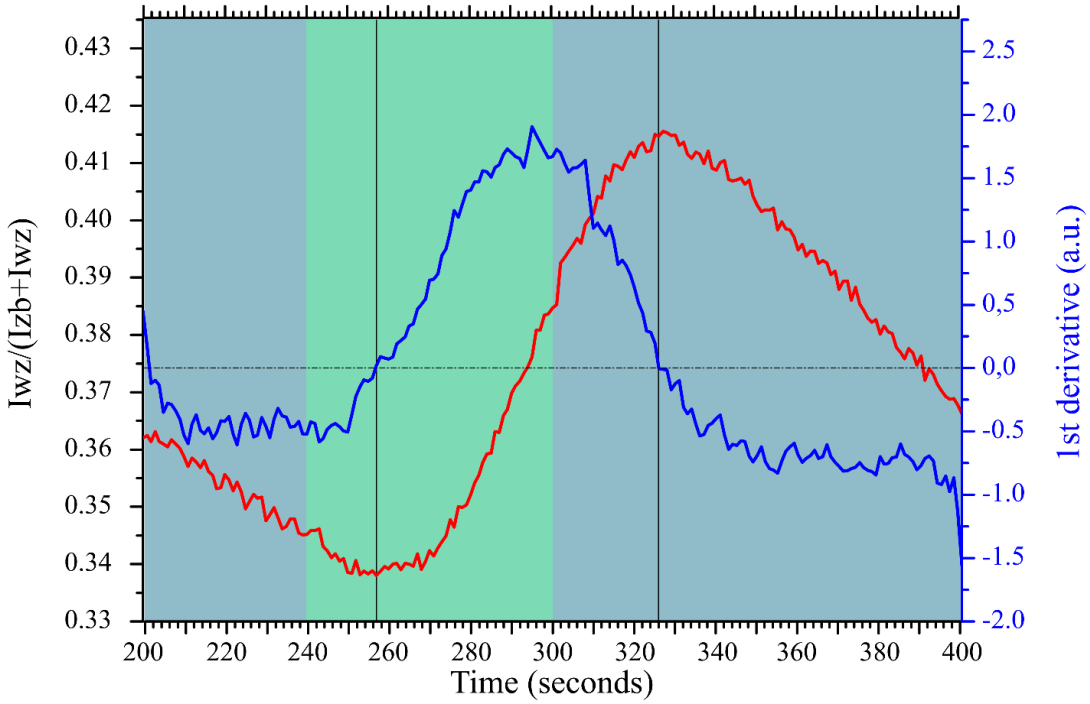


Figure 4.5. Enlarged image of the $IR_{WZ}$ (red curve) corresponding to the WZ segment growth. Blue areas correspond to the growth under Ga and As flux while green area is the growth under As flux only. The blue curve, linked to the right axis, corresponds to the first derivative of the $IR_{WZ}$. The black dashed line corresponds to the zero of the derivative.[29]

These phase transitions were used to estimate the lengths of the bottom ZB and WZ segments (including the ZB/WZ phase mixing segments visible in Figure 4.4.c). Indeed, taking into account the length and the growth time used, we estimated an average axial growth rate $\nu$= 1.7 nm/s (extracted from the average length of the bottom ZB + WZ segments measured in the TEM on around twenty NWs). From the first derivative shown in Figure 4.5, the growth duration of the WZ segment was estimated to 69 seconds, corresponding to an expected length of around 117 nm. Similarly, the length for the bottom ZB segment was calculated to be around 437 nm. In order to validate the viability of the RHEED measurements to characterize the NWs, a comparison between the calculated and the bottom ZB and WZ segment lengths measured in the TEM is reported in Table 4.1.

Table 4.1. Reported values of the growth time, the calculated lengths obtained from RHEED measurements (with an average growth rate of 1.7 nm/s) and the measured lengths extracted from TEM analysis. The growth time were obtained from Figure 4.5.[29]

| | Growth time (seconds) | Calculated length (nm) (from RHEED) | Measured length (nm) (from TEM) |
|---|---|---|---|
| Bottom ZB segment | 257 | ~437 | 440 ± 70 |
| WZ segment (including the ZB/WZ phase mixing segments) | 69 | ~117 | 120 ± 20 |

## 4.3 Simulation of the wetting angle and length evolution

By extending the semi-empirical growth model for Au-catalyzed GaAs[30–32] and InAs[33] NWs, we proposed a model for the self-assisted GaAs NWs[34] to account for the Ga droplet evolution as a function of two parameters: (1) the Ga and As atoms entering the droplets by direct impingement of the corresponding fluxes, and (2) the Ga atoms entering the droplets by diffusion on the $SiO_2$ – terminated silicon substrate (for short NWs) and on the NW facets. This model is described in the following paragraphs.

Assuming a growth time *t*, we can consider a NW presenting a length $L(t)$ and a radius under the droplet $r(t)$. Furthermore, the Ga droplet at the top of the NW can be described with the following parameters: the critical concentration $c^*$, the values for the Ga and As nominal fluxes (*i.e.*, the number of atoms / (unit time) * (unit surface normal to the flux direction)), the radius and As concentration denoted $R(t)$ and $c(t)$, respectively, such as $c(t) \leq c^*$ (subcritical concentration). The amount of Ga and As atoms in the droplet can be written as $Q_{Ga}(t)$ and $Q_{As}(t)$, respectively.

Therefore, the structural evolution of the NW is driven by the amount of Ga and As atoms feeding the Ga droplet, and follows two requirements: (1) the solidification occurs only when the droplet concentration reaches its critical value $c^*$, and (2) the droplet contact angle is such that $\beta_{min} \leq \beta(t) \leq \beta_{max}$.

Then, the NW growth process can be described as follows: in a small interval of time $(t, t+\delta t)$, we assume that the droplet incorporated an amount of Ga atoms $\Delta Q_{Ga}(t)$, coming either from the direct impingement, the diffusion along the NW facets with a diffusion length $\lambda_{facet}$, or from the diffusion on the substrate characterized by its diffusion length $\lambda_{substarte}$. Obviously, the last contribution is lost when the NW length overcomes the diffusion length on the NW facets ($L(t) > \lambda_{facet}$). Meanwhile, we assume that the amount of As atoms incorporated in the droplet, defined as $\Delta Q_{As}(t)$, is only due to the direct impingement.

Consequently, two situations may occur. First, the As "potential concentration" in the droplet at $t+\delta t$, is defined as:

$$\frac{Q_{As}(t) + \Delta Q_{As}(t)}{Q_{As}(t) + \Delta Q_{As}(t) + Q_{Ga}(t) + \Delta Q_{Ga}(t)} \leq c^*. \qquad (4.1)$$

In this situation, the solidification at the droplet / NW interface does not occur. Two distinct sub-cases can then be distinguished: (1) the droplet is pinned on the top of the NW with a contact angle $\beta \leq \beta_{max}$, leading to an increase of the droplet volume with a constant NW length (no axial growth). (2) If the droplet volume induces a contact angle $\beta > \beta_{max}$, the computation is stopped by considering the droplet stability.

The second situation presents an As "potential concentration" in the droplet defined as:

$$\frac{Q_{As}(t) + \Delta Q_{As}(t)}{Q_{As}(t) + \Delta Q_{As}(t) + Q_{Ga}(t) + \Delta Q_{Ga}(t)} > c^*. \quad (4.2)$$

In this case, a unique and equal quantities $Q$ of Ga and As atoms exists such as:

$$\frac{Q_{As}(t) + \Delta Q_{As}(t) - Q}{Q_{As}(t) + \Delta Q_{As}(t) + Q_{Ga}(t) + \Delta Q_{Ga}(t) - 2Q} = c^*. \quad (4.3)$$

Otherwise stated, only the excess of Ga and As atoms (due to supersaturation) will contribute to the solidification process. However, the volume of solid material can contribute to both axial and radial growth, depending on the remaining volume of the Ga droplet, which includes the total amount of Ga and As atoms defined as $Q_{As}(t) + \Delta Q_{As}(t) + Q_{Ga}(t) + \Delta Q_{Ga}(t) - 2Q$. If this volume can be pinned on the top of the NW with a contact angle $\beta(t + \delta t)$ such as $\beta_{min} \leq \beta(t + \delta t) \leq \beta_{max}$, only the axial growth is observed. In the other case, two distinct sub-cases may occur.

1) If the contact angle $\beta(t + \delta t) > \beta_{max}$, an inverse tapered axial growth is observed. The inverse tapering leads to a modification of the NW radius to $r(t + \delta t)$, corresponding to the unique value able to support the fixed droplet volume at contact angle $\beta_{max}$. Subsequently, the axial growth will place the solid material in a truncated cone geometry with lower radius $r(t)$, upper radius $r(t + \delta t)$, and height determined by the amount of equal solid quantities $Q$ of Ga and As atoms.

2) If the contact angle $\beta(t + \delta t) < \beta_{min}$ the situation is similar to 1), with an axial growth and a direct tapering. Indeed, a unique value of $r(t + \delta t)$ able to support the droplet at a contact angle $\beta_{min}$ exists. The solid material will then be placed in a truncated cone geometry with lower radius $r(t)$, upper radius $r(t + \delta t) < r(t)$, and height determined by the amount of equal solid quantities $Q$ of Ga and As atoms.

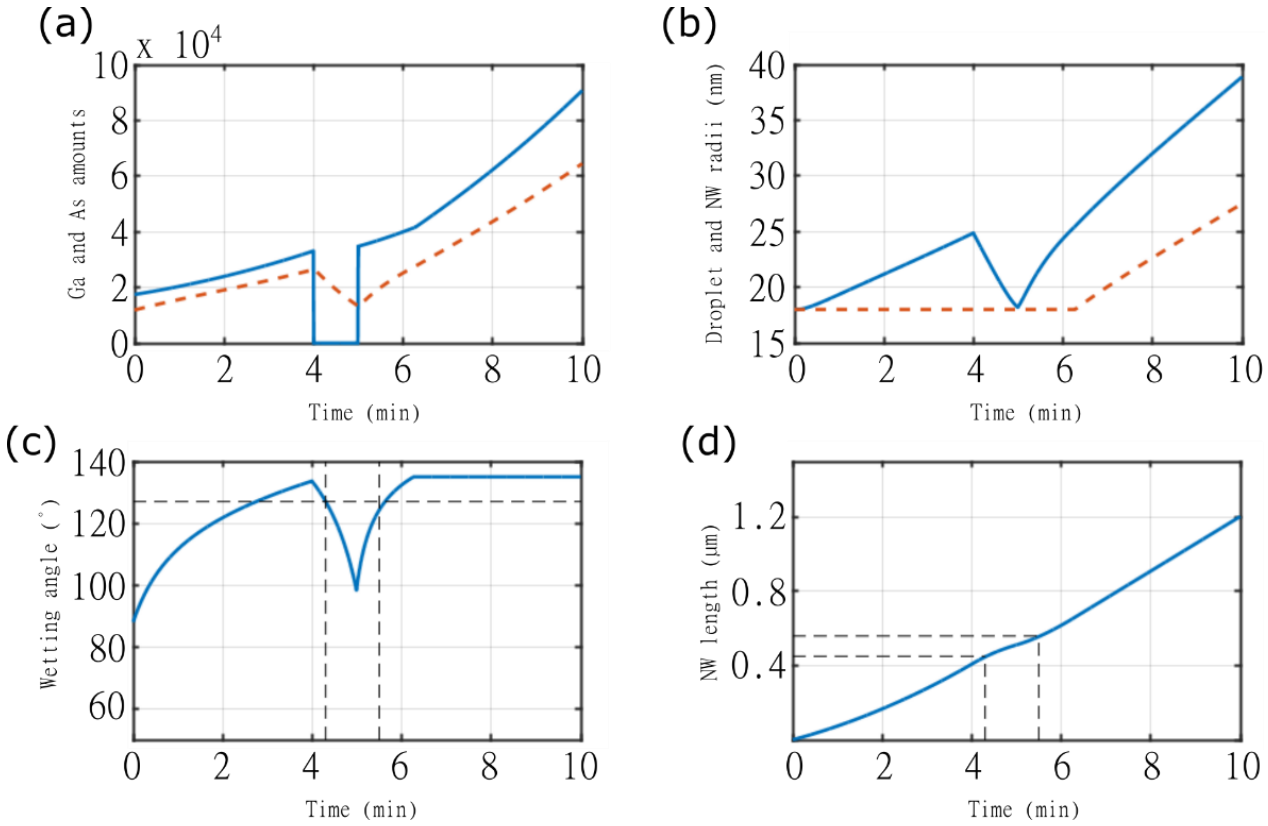


Figure 4.6. Curves representing the time evolution of (a) the number of Ga atoms (blue line) and As atoms (dashed orange line) feeding the droplet, (b) the droplet (blue line) and NW (dashed orange line) radii, (c) the wetting angle and (d) the NW length. The numerical results were obtained using: a Ga and As sources located at incidence angles of 27.9° and 41°, respectively, with respect to the normal of the substrate. The nominal Ga and As fluxes used: $F_{Ga}$ = 3.53 atoms/sec.nm$^2$ and $F_{As}$ = 27.3 atoms/sec.nm$^2$. The best fit was obtained using a diffusion length on the $SiO_2$ and on the NW facets of 38 nm and 1.4 µm, respectively. The As concentration threshold in the droplet was fixed at 1%. The initial radius and wetting angle of the droplet were equal to 18 nm and 90°, respectively.[29]

Finally, the algorithm can stop in the unrealistic situation when the NW radius becomes too large or too small. Assuming a critical concentration $c^* = 0.01$, and contact angles $\beta_{min} = 50°$ and $\beta_{max} = 140°$ under Ga and As fluxes of 0.5 and 1.15 ML/s, respectively, the numerical results are plotted in Figure 4.6.

As a consequence, besides the classical axial NW growth, the described model is able to predict the conditions triggering both axial and lateral growths, depending on the droplet evolution. In our specific case, the model is expected to provide and confirm the existence of a unique critical value of the contact angle, where the transition from the cubic ZB to the hexagonal WZ phases occurs. Results of the numerical simulations show the time evolution of the Ga and As amounts of atoms supplying the droplet, the droplet and NW radii, the contact angle of the droplet, and the NW length on Figure 4.6.a – d, respectively. The interruption of the Ga flux between 240 and 300 seconds induced a decrease of the droplet radius from about 25 nm to 18 nm (Figure 4.6.b), and therefore of the contact angle from 134° to 98° (Figure 4.6.c). Moreover, a reduction of the droplet capture surface of the As atoms was induced by the diminution of the contact angle, leading to a slight lower axial growth rate, as shown in Figure 4.6.d. Then, an increase of the droplet

radius and contact angle were observed immediately after the re-opening of the Ga shutter, after 300 seconds. The maximum contact angle $\beta_{max}$ was then reached about 70 seconds after the re-feeding of the droplet in Ga atoms, leading to an increase of the NW radius (Figure 4.6.b), needed to accommodate the higher droplet volume.

The vertical dashed lines in Figure 4.6.c and Figure 4.6.d correspond to the time $t_1$ = 257 seconds and $t_2$ = 326 seconds, highlighting the transition times identified in Figure 4.5. Therefore, the corresponding bottom ZB and WZ segment lengths predicted by our numerical simulations are 450 nm and 106 nm, respectively (Figure 4.6.d). The lengths obtain using this model are in good agreement with the TEM measurements of 440 ± 70 nm and 120 ± 20 nm, respectively, reported in Table 4.1. Similarly, we identified and predict contact angles equal to 126° for the ZB to WZ transition and to 124° for the WZ to ZB transition (Figure 4.6.c), in agreement with the results recently reported by Kim *et al*[22] by *ex situ* TEM and measured by F. Panciera *et al* by *in situ* TEM[24] on self-assisted GaAs NWs. The lengths predicted by the numerical models are compared with the previously measured lengths in Table 4.2.

Table 4.2. Reported values of the growth time, the calculated lengths obtained from RHEED measurements (with an average growth rate of 1.7 nm/s), measured lengths extracted from TEM analysis and simulated lengths predicted by the numerical simulations. The growth time were obtained from Figure 4.5. The measured lengths are average values obtained by measurements on TEM images of about twenty NWs. The WZ segment measured by TEM includes the ZB/WZ mixing phases[29].

| | Growth time (seconds) | Calculated length (nm) (from RHEED) | Measured length (nm) (from TEM) | Simulated length (nm) |
|---|---|---|---|---|
| Bottom ZB segment | 257 | ~437 | 440 ± 70 | 450 |
| WZ segment (including the ZB/WZ phase mixing segments) | 69 | ~117 | 120 ± 20 | 106 |

## 4.4 Conclusion

In this chapter, we showed that it was possible to track the formation of ZB and WZ structures through the indexation of the ZB and WZ diffraction spots observed in a RHEED pattern during the growth of self-assisted GaAs NWs, in real time. Using this approach, we followed the complete consumption of the Ga catalyst droplets at the end of the growth, induced by the interruption of the Ga flux. We established a procedure capable of producing extended WZ segments inside ZB GaAs NWs using only an *in situ* characterization technique such as RHEED. Finally, we demonstrated the strong capabilities of the RHEED to characterize the NW crystal structure during the growth, by confirming the observations using numerical simulations and *post mortem* TEM measurements. We obtained a value for the critical contact angle $\beta_1$ = 125° by combining our RHEED analysis with a numerical model. The real-time RHEED characterization presented in this chapter thus acts as a premise for an advanced control of the nucleation of hexagonal self-assisted GaAs NWs growth, discussed in the next chapter.

## 4.5 References

1. Glas, F., Harmand, J.-C. & Patriarche, G. Why Does Wurtzite Form in Nanowires of III-V Zinc Blende Semiconductors? *Phys. Rev. Lett.* **99**, 146101 (2007).

2. Fontcuberta i Morral, A., Colombo, C., Abstreiter, G., Arbiol, J. & Morante, J. R. Nucleation mechanism of gallium-assisted molecular beam epitaxy growth of gallium arsenide nanowires. *Appl. Phys. Lett.* **92**, 063112 (2008).

3. Capiod, P. *et al.* Band offsets at zincblende-wurtzite GaAs nanowire sidewall surfaces. *Appl. Phys. Lett.* **103**, 122104 (2013).

4. Spirkoska, D. *et al.* Structural and optical properties of high quality zinc-blende/wurtzite GaAs nanowire heterostructures. *Phys. Rev. B* **80**, 245325 (2009).

5. Ahtapodov, L. *et al.* A Story Told by a Single Nanowire: Optical Properties of Wurtzite GaAs. *Nano Lett.* **12**, 6090–6095 (2012).

6. Vainorius, N. *et al.* Observation of type-II recombination in single wurtzite/zinc-blende GaAs heterojunction nanowires. *Phys. Rev. B* **89**, 165423 (2014).

7. Mante, P.-A., Lehmann, S., Anttu, N., Dick, K. A. & Yartsev, A. Nondestructive Complete Mechanical Characterization of Zinc Blende and Wurtzite GaAs Nanowires Using Time-Resolved Pump–Probe Spectroscopy. *Nano Lett.* **16**, 4792–4798 (2016).

8. Zou, X., Chen, X., Huang, H., Xu, Y. & Duan, W. Enhanced thermoelectric figure of merit in thin GaAs nanowires. *Nanoscale* **7**, 8776–8781 (2015).

9. Al-Zahrani, H. Y. S., Pal, J., Migliorato, M. A., Tse, G. & Yu, D. Piezoelectric field enhancement in III–V core–shell nanowires. *Nano Energy* **14**, 382–391 (2015).

10. Calahorra, Y. *et al.* Exploring piezoelectric properties of III–V nanowires using piezo-response force microscopy. *Semicond. Sci. Technol.* **32**, 074006 (2017).

11. Jabeen, F., Grillo, V., Rubini, S. & Martelli, F. Self-catalyzed growth of GaAs nanowires on cleaved Si by molecular beam epitaxy. *Nanotechnology* **19**, 275711 (2008).

12. Cirlin, G. E. *et al.* Self-catalyzed, pure zincblende GaAs nanowires grown on Si(111) by molecular beam epitaxy. *Phys. Rev. B* **82**, 035302 (2010).

13. Plissard, S. *et al.* Gold-free growth of GaAs nanowires on silicon: arrays and polytypism. *Nanotechnology* **21**, 385602 (2010).

14. Rudolph, D. *et al.* Direct Observation of a Noncatalytic Growth Regime for GaAs Nanowires. *Nano Lett.* **11**, 3848–3854 (2011).

15. Yu, X. *et al.* Evidence for Structural Phase Transitions Induced by the Triple Phase Line Shift in Self-Catalyzed GaAs Nanowires. *Nano Lett.* **12**, 5436–5442 (2012).

16. Heon Kim, Y., Woo Park, D. & Jun Lee, S. Gallium-droplet behaviors of self-catalyzed GaAs nanowires: A transmission electron microscopy study. *Appl. Phys. Lett.* **100**, 033117 (2012).

17. Scarpellini, D. *et al.* Ga crystallization dynamics during annealing of self-assisted GaAs nanowires. *Nanotechnology* **28**, 045605 (2017).

18. Krogstrup, P. *et al.* Impact of the Liquid Phase Shape on the Structure of III-V Nanowires. *Phys. Rev. Lett.* **106**, 125505 (2011).

19. Dubrovskii, V. G. *et al.* New Mode of Vapor−Liquid−Solid Nanowire Growth. *Nano Lett.* **11**, 1247–1253 (2011).

20. Krogstrup, P. *et al.* Advances in the theory of III–V nanowire growth dynamics. *J. Phys. D: Appl. Phys.* **46**, 313001 (2013).

21. Jacobsson, D. *et al.* Interface dynamics and crystal phase switching in GaAs nanowires. *Nature* **531**, 317–322 (2016).

22. Kim, W. *et al.* Bistability of Contact Angle and Its Role in Achieving Quantum-Thin Self-Assisted GaAs nanowires. *Nano Lett.* **18**, 49–57 (2018).

23. Harmand, J.-C. *et al.* Atomic Step Flow on a Nanofacet. *Phys. Rev. Lett.* **121**, 166101 (2018).

24. Panciera, F. *et al.* Phase Selection in Self-catalyzed GaAs Nanowires. *Nano Lett.* **20**, 1669–1675 (2020).

25. Krogstrup, P. *et al. In-situ* x-ray characterization of wurtzite formation in GaAs nanowires. *Appl. Phys. Lett.* **100**, 093103 (2012).

26. Bastiman, F., Küpers, H., Somaschini, C., Dubrovskii, V. G. & Geelhaar, L. Analysis of incubation time preceding the Ga-assisted nucleation and growth of GaAs nanowires on Si(111). *Phys. Rev. Materials* **3**, 073401 (2019).

27. Jo, J., Tchoe, Y., Yi, G.-C. & Kim, M. Real-Time Characterization Using in situ RHEED Transmission Mode and TEM for Investigation of the Growth Behaviour of Nanomaterials. *Sci Rep* **8**, 1694 (2018).

28. Jakob, J. *et al.* Quantitative analysis of time-resolved RHEED during growth of vertical nanowires. *Nanoscale* **12**, 5471–5482 (2020).

29. Dursap, T. *et al.* Crystal phase engineering of self-catalyzed GaAs nanowires using a RHEED diagram. *Nanoscale Adv.* **2**, 2127–2134 (2020).

30. Dubrovskii, V. G., Sibirev, N. V., Harmand, J. C. & Glas, F. Growth kinetics and crystal structure of semiconductor nanowires. *Phys. Rev. B* **78**, 235301 (2008).

31. Krogstrup, P. *et al.* Structural Phase Control in Self-Catalyzed Growth of GaAs Nanowires on Silicon (111). *Nano Lett.* **10**, 4475–4482 (2010).

32. Dubrovskiĭ, V. G. *et al.* The role of surface diffusion of adatoms in the formation of nanowire crystals. *Semiconductors* **40**, 1075–1082 (2006).

33. Tchernycheva, M. *et al.* Au-assisted molecular beam epitaxy of InAs nanowires: Growth and theoretical analysis. *Journal of Applied Physics* **102**, 094313 (2007).

34. Vettori, M. *et al.* Impact of the Ga flux incidence angle on the growth kinetics of self-assisted GaAs nanowires on Si(111). *Nanoscale Adv.* **1**, 4433–4441 (2019).

# 5 The growth of a pure-WZ segment in self-assisted GaAs nanowires

## Chapter contents



### 5.1 Introduction

The occurrence of the cubic ZB and hexagonal WZ structures appears as an important feature of III-V semiconductors, which determines their properties. It is now well known that GaAs, a technologically relevant and massively employed material, crystalizes in the ZB structure in its bulk phase, whereas WZ nucleation occurs only with in NWs. Despite this limitation, the growth of GaAs NWs represents an advantageous outcome for application as integrated light source on silicon. Moreover, hexagonal GaAs NWs have recently been shown to be crucial building blocks for the growth of hexagonal Ge and light emitting SiGe alloys[1], notably.

However, as promising as these materials might be, the current reports face a bottleneck limiting the upgrade from prototypes to applied devices. Indeed, WZ GaAs NWs are obtained using the Au-catalyzed growth[2–6] as discussed in previous chapters, which is incompatible with the silicon electronic industry, due to trap states induced by gold in silicon[7,8], thus preventing the integration of these NWs on Si substrates. Self-assisted growth thus appears as the optimal solution to overcome the gold-contamination of the NWs. As already discussed in chapter 3, recent prototypical growth reactors have been used to highlight the nucleation mechanism of the different crystal structures and to control the phase on a single self-assisted GaAs NW[9]. The extended growth of the WZ structure of self-assisted GaAs NWs by MBE has only been investigated in recent studies, with the achievement of a 1.8 µm long pure WZ segment by Jansen's group[10], on pre-patterned substrates by controlling the Ga flux during the growth.

In our group, we demonstrated the applicability of RHEED in the control of the crystal structures grown in self-assisted GaAs NWs, giving access to the real-time monitoring of the crystal phase evolution during the growth[11] (discussed in chapter 4). It was possible to tune the growth parameters, such as the Ga and As flux, and force the nucleation of hexagonal WZ segments. In this chapter, the growth of self-assisted GaAs NWs, leading to an extended pure WZ segment of 1.3 µm long, will be presented and discussed. This growth was controlled by *in situ* RHEED and supported by numerical simulations, and has been the subject of a publication[10].

The MBE growths, RHEED interpretations, SEM and STEM characterizations were performed by myself. DF-TEM images were obtained by Nicholas Blanchard from the Institut Lumière Matière, Lyon. Finally, PL measurements and interpretations were carried out by Nicolas Chauvin from INL.

## 5.2 Simulation of the wetting angle as a function of the III and V fluxes

As far as the self-assisted GaAs growth is concerned, the cubic ZB and hexagonal WZ phases are determined by the contact angle $\beta$ between the droplet and the top facet of the NW[12]. For instance, when the Ga flux is interrupted and the As atoms feed the droplet by direct impingement, the contact angle of the droplet decreases and the crystal structure evolves from the ZB to the WZ phase, and then back to the ZB phase, as highlighted in the previous chapter. As discussed, the nucleation of the WZ phase occurs for a contact angle in the 90 – 125° range[9,11]. Then, the main question addressed is the following: is it possible to provide values for the V/III flux ratio that ensure a fixed contact angle in the 90 – 125° range, thus ensuring the growth of the WZ phase ?

The positive answer to this question is a consequence of the general statement that the self-assisted NW growth is a self-regulated system[13]. Indeed, considering fixed values of the Ga and As fluxes, the radius of the NW, the size of the droplet and its contact angle evolve toward a stationary regime, in which the amounts of Ga and As atoms supplied to the droplet are equal. However, this so-called constant growth regime could only be reached once the length of the NWs overcome a first-stage of "transient' regime.

Previous studies on self-assisted GaAs NW growth[13–17], show that the Ga atoms are assumed to supply the liquid droplet through three distinct sources, as illustrated in Figure 5.1.

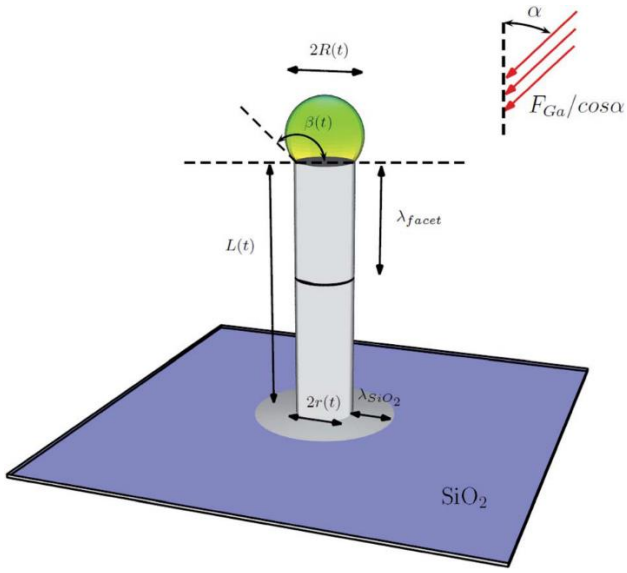


Figure 5.1. Geometry of the NW and droplet, generic flux position at an angle $\alpha$ with respect to the substrate normal and diffusion lengths[13].

Firstly, the amount of Ga atoms able to attain the droplet by surface diffusion on the $SiO_2$-terminated substrate, denoted $q_{Ga}^{sub}$ and defined by:

$$q_{Ga}^{sub}(t) = F_{Ga} S^{sub}(t), \qquad (5.1)$$

where $F_{Ga}$ corresponds to the Ga flux on the $SiO_2$-terminated substrate (in our case 0.5 ML/s, as explained in chapter 3) and $S^{sub}(t) = \pi[\left(\lambda_{SiO_2} + r(t)\right)^2 - r^2(t)]$ is the substrate capture area, with $\lambda_{SiO_2}$ the diffusion length on the $SiO_2$-terminated substrate and $r(t)$ the NW radius.

Secondly, the amount of Ga atoms able to reach the droplet by diffusion along the NW facets, denoted $q_{Ga}^{facet}$ and defined by:

$$q_{Ga}^{facet}(t) = F_{Ga} \tan \alpha_{Ga} S^{facet}(t), \qquad (5.2)$$

where $\alpha_{Ga}$ is the angle of the Ga source with respect to the normal of the substrate and $S^{facet}(t) = 2r(t)min\left(\lambda_{facet}, L(t)\right)$ represents the NW facet capture area projected on the plane normal to the Ga flux orientation. The $min$ function here above accounts for the NW length only for NWs with length $L(t)$ smaller than $\lambda_{facet}$.

Thirdly, the amount of Ga atoms feeding the droplet by direct impingement is written as:

$$q_{Ga}^{droplet}(t) = \frac{F_{Ga}}{\cos\alpha_{Ga}} S(\alpha_{Ga}, \beta(t), r(t)), \quad (5.3)$$

where $S(\alpha_{Ga}, \beta(t), r(t))$ is the value of the droplet area projected in the direction normal to the flux, when the droplet has a contact angle $\beta(t)$ with the top of a NW with a radius $r(t)$.

Meanwhile, we assumed that the As atoms only feed the catalyst through a direct impingement on the droplet surface, giving thus a quantity $q_{As}^{droplet}$ of As atoms supplying the droplet defined by:

$$q_{As}^{droplet}(t) = q_{As} S(\alpha_{As}, \beta(t), r(t)), \quad (5.4)$$

where $q_{As}$ corresponds to the nominal flux of As and $\alpha_{As}$ represents to the angle of the As source with respect to the normal of the substrate.

By considering the stationary regime introduced at the beginning of this section, in which the amounts of Ga and As atoms supplied to the droplet are equal, we can state the following:

$$q_{Ga}^{sub} + q_{Ga}^{facet} + q_{Ga}^{droplet} = q_{As}^{droplet}. \quad (5.5)$$

Therefore, recent experimental results obtained by using two Ga sources with different positions with respect to the substrate[13] show a disappearance of the substrate diffusion contribution $q_{Ga}^{sub}$ when the NW length $L(t)$ overcomes the diffusion length on the NW facets $\lambda_{facet}$, which is typically in the 1 – 2 µm range. Hence, by growing self-assisted GaAs NWs for 25 minutes using the standard growth parameters described in chapter 3, we obtained NWs longer than 2 µm. This 25 minute growth will hereafter be referred to as "standard growth". In these conditions, the previous equality can be reduced to:

$$q_{Ga}^{facet} + q_{Ga}^{droplet} = q_{As}^{droplet}. \quad (5.6)$$

Subsequently considering the Ga nominal flux $q_{Ga} = \frac{F_{Ga}}{\cos\alpha_{Ga}}$, we can express the equal amount of Ga and As atoms supplied to the droplet as:

$$q_{Ga}\sin(\alpha_{Ga}) 2r\lambda_{facet} + q_{Ga} S(\alpha_{Ga}, \beta, r) = q_{As} S(\alpha_{As}, \beta, r). \quad (5.7)$$

Furthermore, the above equality can be used to explain the self-regulation of the system. Indeed, in the case of an As-rich regime, the equation's right – hand side (RHS) becomes larger than the left – hand side (LHS), inducing a decrease of the droplet volume. The contact angle of the droplet decreases to a value for which the surface diffusion term balances the difference between the direct impingement terms. On the contrary, in the Ga-rich regime, the volume of the droplet will tend to increase leading to a rise of its contact angle. As both direct impingement terms increase and the V/III flux ratio is larger than 1, the RHS will

increase faster than the LHS. In both cases the evolution of the system tends to a stationary growth regime, presenting a constant contact angle.

With known orientations of the Ga and As sources ($\alpha_{Ga}$ and $\alpha_{As}$, respectively), a contact angle $\beta$ in the 90 – 125° range can be determined using the V/III flux ratio given by:

$$\frac{q_{As}}{q_{Ga}} = \frac{\sin(\alpha_{Ga})2r\lambda_{facet} + S(\alpha_{Ga},\beta,r)}{S(\alpha_{As},\beta,r)} = \frac{\sin(\alpha_{Ga})2\gamma + S(\alpha_{Ga},\beta,1)}{S(\alpha_{As},\beta,1)}, \qquad (5.8)$$

where the last equality holds since $S(\alpha,\beta,r)$ is quadratic with respect to $r$, and $\gamma$ represents the number $\frac{\lambda_{facet}}{r}$. Moreover, this equation shows that a fixed V/III flux ratio can lead to different contact angles for different NW radii, so that the ideal situation is the monodisperse case. Using our model that accounts for the droplet evolution and a variable NW radius presented in the work of M. Vettori *et al*[13], a numerical value for the diffusion length on the facets $\lambda_{facet}$ = 1.8 µm, and our reactor configurations ($\alpha_{Ga}$ = 28° and $\alpha_{As}$ = 41°), we computed the values of the contact angle $\beta$, as a function of the radius $r$ of the NW and the V/III flux ratio $\frac{q_{As}}{q_{Ga}}$. These contact angles are therefore called asymptotic, as they equilibrate the amount of Ga and As atoms for various radii and V/III flux ratios.

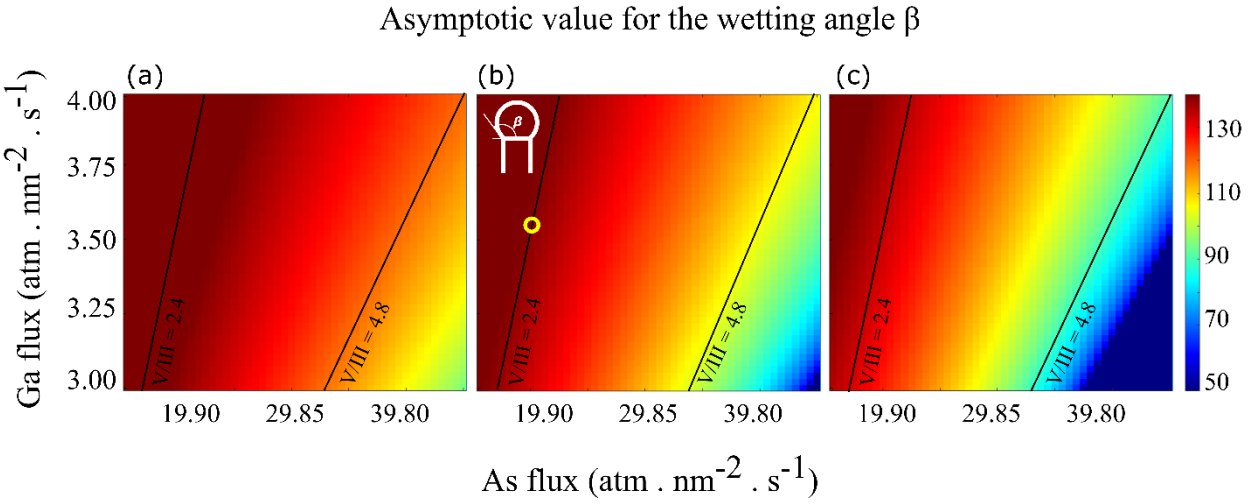


Figure 5.2. Values of the wetting angle $\beta$ obtained for NWs with a radius $r$ equal (a) 40 nm, (b) 50 nm and (c) 60 nm for various V/III flux ratio. The area highlighted with the yellow circle represents the conditions used for the NW growth (V/III flux ratio = 2.4 at $q_{Ga}$ = 3.53 atm.nm$^{-2}$.s$^{-1}$), in order to overcome the transient regime where the diffusion on the $SiO_2$-terminated substrate contributes to the Ga supply. Values lower than 50° are not represented as we consider that the droplet disappears and the VLS growth stops. Black lines represents V/III flux ratio equal to (left) 2.4 and (right) 4.8.[18]

Figure 5.2.a – c illustrate the asymptotic values of the contact angle $\beta$ for a large range of ($q_{As}$, $q_{Ga}$) couples and for different radius. The yellow circle on the left side of Figure 5.2.b (V/III flux ratio = 2.4 and $q_{Ga}$ = 0.5 ML/s = 3.53 atm/(nm.s)) represents the ($x$, $y$) position of the standard growth conditions described

in chapter 3. As illustrated in Figure 5.2, V/III flux ratio larger than 3.5 – 4.0 can lead to asymptotic values of the contact angle lower than 125°. On the contrary, too large values of the V/III flux ratio will stop the VLS growth process due to the extinction of the droplet. The oblique black lines visible on the color maps correspond to V/III flux ratios of 2.4 (left) and 4.8 (right).

In order to experimentally verify these simulations, NWs obtained after our standard growth were characterized by SEM, as shown in Figure 5.3.a. The grown NWs were about 2.7 ± 0.2 µm long, with a diameter in the 90 – 100 nm range. The contact angle was then measured around 137°, in complete accordance with F. Panciera *et al*[9] and with the expected asymptotic value highlighted in Figure 5.2.b by the yellow circle. Furthermore, the RHEED diagram recorded along the $[1\bar{1}0]$ azimuth at the end of the growth highlights the presence of the ZB structure only, as expected by the measured contact angle (Figure 5.3.b).

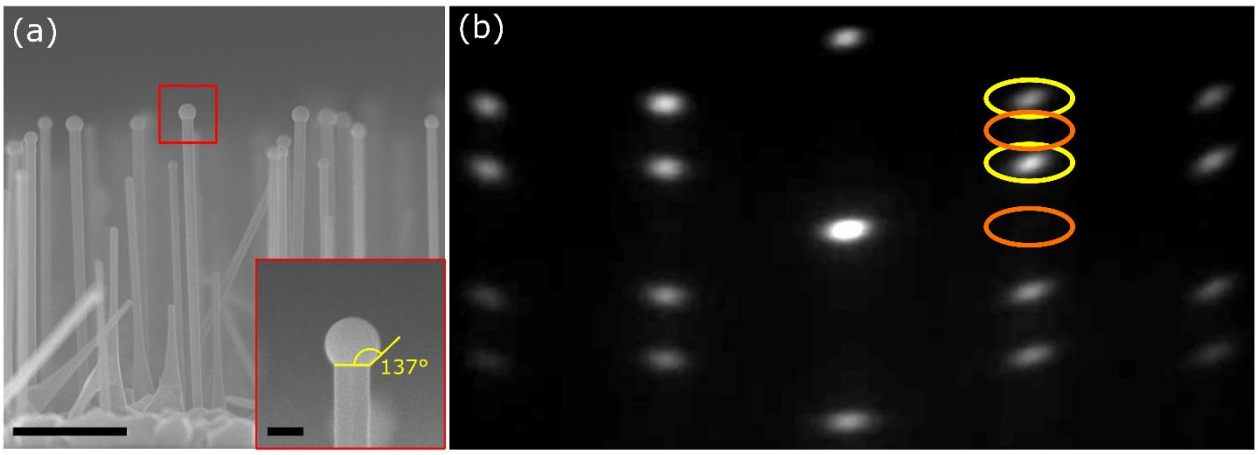


Figure 5.3. (a) Side view SEM image showing the NW morphology after the standard growth of 25 min. Scale bar is 1 µm. The inset corresponds to a higher magnification image of the droplet at the end of a NW. Scale bar is 100 nm. (b) RHEED pattern recorded at the end of the growth along the $[1\bar{1}0]$ azimuth, where only the ZB spots (highlighted by the yellow circles) are visible. The orange circles show the position of the WZ spots.

Thus, the numerical implementation of the model suggests the following growth recipe: a first VLS stage using the standard conditions, leading to a ZB phase, used to overcome the transient regime due to the on – substrate diffusion. This stage will then be followed by an increase of the V/III flux ratio from 2.4 to a value between 4.0 and 7.0. It is important to notice that for large diameter NWs (typically larger than about 120 nm) the VLS growth process stops, while for NWs with diameters smaller than a critical threshold (typically smaller than about 80 nm) the VLS growth continues with a contact angle larger than 125°. However, considering a typical diameter distribution, we estimate that about 90% of the sample will switch from ZB phase to the stationary growth in the WZ phase.

Therefore, a first series of samples was grown starting with a standard growth, followed by the growth using higher V/III flux ratio. The contact angle induced by these increases of V/III flux ratio was systematically measured using SEM. Each value was then compared with the expected angles given by the

simulation and reported in Table 5.1. The correlation between the measurements and the simulations is strong, showing an optimal V/III flux ratio of 4.0 that led to a contact angle of 120°.

Table 5.1. Measured and simulated values of the contact angle $\beta$ for different growth conditions. The first row corresponds to the standard growth of the self-assisted GaAs NWs, with a V/III flux ratio of 2.4. The other rows correspond to a standard growth, followed by an extended growth with higher As flux. The hypothetical optimal growth is highlighted in blue.

| | Growth time under high V/III (in minutes) | Measured contact angle (°) | Simulated contact angle (°) |
|---|---|---|---|
| Standard growth reference | | 137 | 140 |
| Standard growth follows by V/III = 3.0 | 20 | 135 | 135 |
| Standard growth follows by V/III = 3.7 | 20 | 127 | 125 |
| Standard growth follows by V/III = 4.0 | 20 | 120 | 120 |
| Standard growth follows by V/III = 4.3 | 20 | 109 | 113 |

In order to investigate more in depth the impact of the V/III flux ratio on the contact angle, we grew a series of four samples using four different As flux, to obtain V/III flux ratios of 3.0, 3.7, 4.0 and 4.3. The IRs and RHEED diffraction patterns obtained are reported in Figure 5.4.

With a low V/III flux ratio (3.0 and 3.7), an increase of the $IR_{WZ}$ (and decrease of the $IR_{ZB}$) was first observed, indicating the nucleation of a WZ segment, and was followed by an increase of the $IR_{ZB}$. Indeed, the increase of the As flux led to a decrease of the contact angle, and consequently to the formation of a faulty section. The droplet then tends to stabilize with a contact angle larger than 125°, as shown in Table 5.1. On the contrary, higher V/III flux ratio (4.0 and 4.3) led to a constant increase of the $IR_{WZ}$. The change of the slope observed after about 200 seconds is due to the loss of the ZB contribution, due to a probed depth of a few hundreds of nanometers, as described in chapter 4. It thus appears that a V/III flux ratio of 4.0 (or 4.3) starts as the optimal parameter to grow an extended WZ segment in self-assisted GaAs NWs.

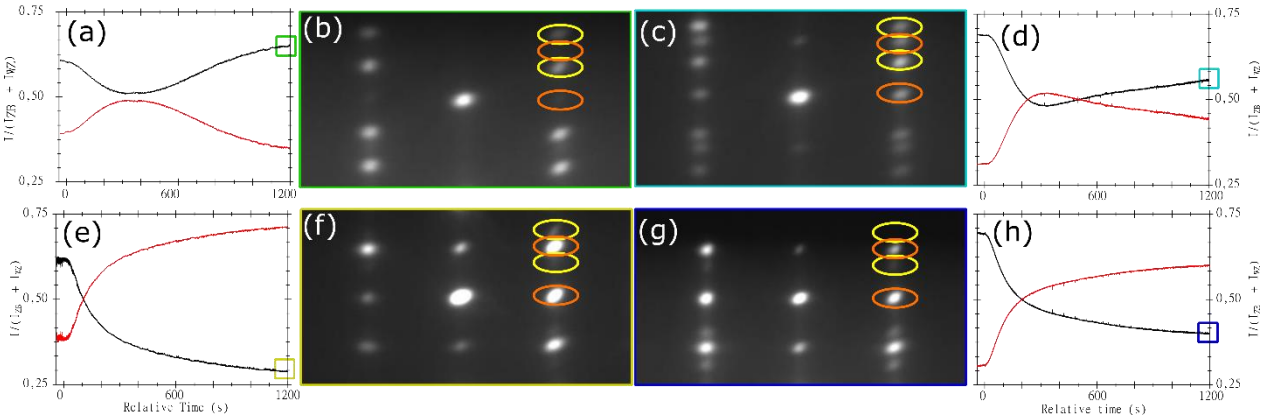


Figure 5.4. $IR_{ZB}$ (black line) and $IR_{WZ}$ (red line) obtained during 20 minutes' growth and RHEED patterns taken at the end of the growth for a V/III flux ratio of (a) and (b) 3.0, (c) and (d) 3.7, (e) and (f) 4.0, (g) and (h) 4.3. On the IR *x*-axis, $t = 0$ corresponds to the increase of the As flux. The time indicates the growth time under high As flux, which follows a first stage of standard growth. The yellow and orange circles indicate the ZB and WZ spots, respectively.

## 5.3 Evidences of the pure-WZ phase

The stationary growth of the WZ phase was followed in real-time using our *in situ* RHEED analysis method discussed in chapter 4. The evolution of the RHEED pattern was continuously recorded during the entire growth under high As pressure (V/III = 4.0).

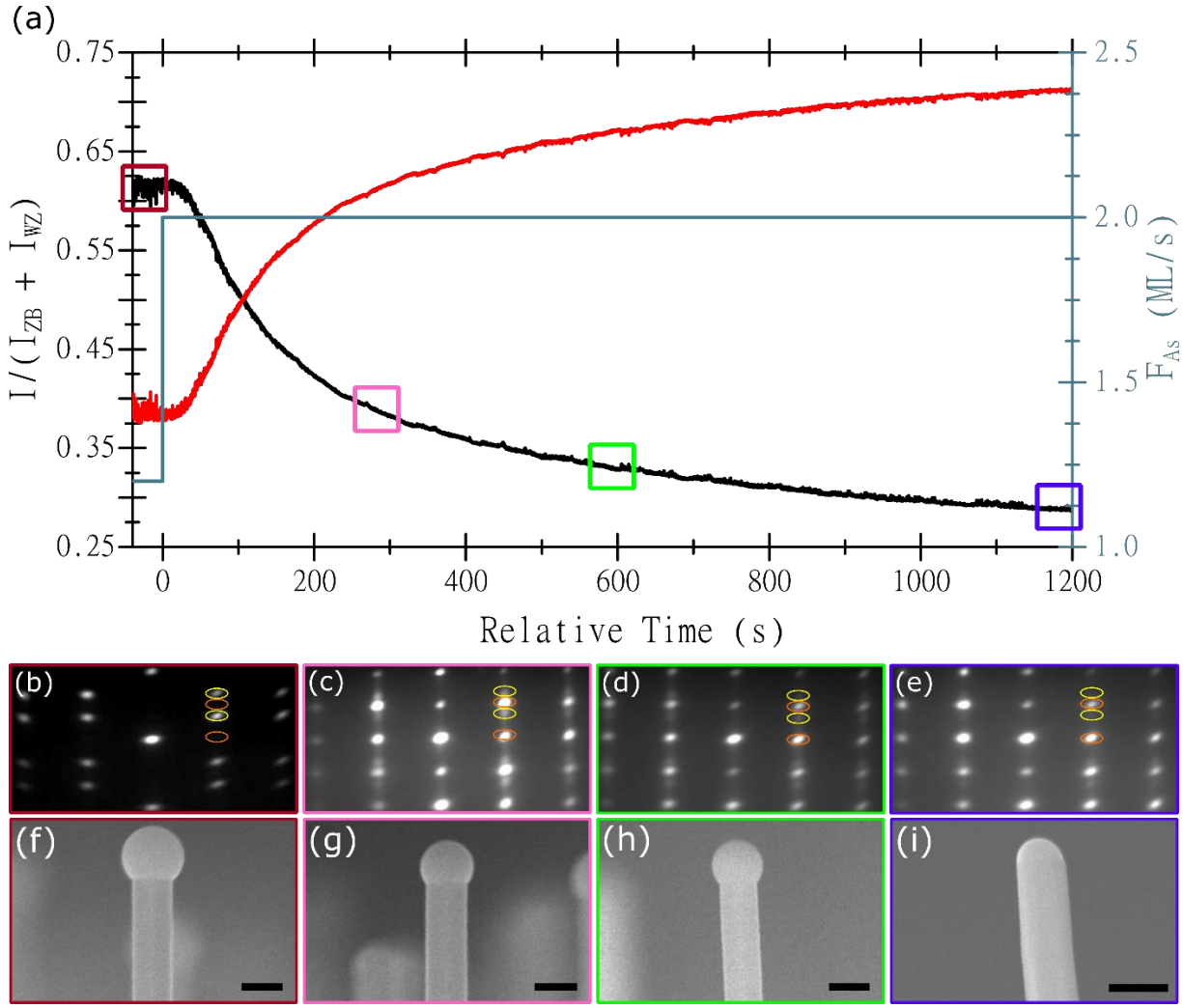


Figure 5.5. $IR_{ZB}$ (black line) and $IR_{WZ}$ (red line), associated to the left y-axis, as a function of the relative growth time ($t$ = 0 s corresponds to the increase of the As flux, after the 25 min growth under the standard conditions). The light blue line, associated to the right y-axis, corresponds to the As flux in ML/s. RHEED patterns recorded along the [1$\bar{1}$0] azimuth and SEM images of the catalyst droplet (b, f) before the increase of the As flux, and after (c, g) 5 min, (d, h) 10 min and (e, i) 20 min of growth under high As flux. The ZB and WZ spots on the RHEED patterns are highlighted with the yellow and orange circles, respectively. Scale bars in (f – i) are 100 nm. Figure adapted from ref [18].

Figure 5.5.a illustrates the $IR_{ZB}$ and $IR_{WZ}$ obtained during a 20 minutes growth with a V/III flux ratio of 4.0 that follows a standard growth. The *x*-axis represents the growth time under high As flux such as $t$ = 0 seconds corresponds to the increase of the As pressure. An increase of the $IR_{WZ}$ was observed around 20

seconds after the augmentation of the V/III flux ratio, as shown in chapter 4[11]. A progressive disappearance of the ZB signal during the growth is then clearly visible in the IRs lines (Figure 5.5.a) as well as on the RHEED pattern shown in Figure 5.5.b – e, thus proving the growth of a WZ phase. The growth was then ended by stopping the Ga and As fluxes simultaneously, in order to maintain the droplet at the top of the NWs. The contact angle of the Ga droplet was measured on tens of NWs before the increase of As pressure and after 5 minutes, 10 minutes and 20 minutes (Figure 5.5.f – i, respectively) of growth using SEM. After 5 and 10 minutes, the contact angle was measured close to 120°, as predicted by the simulation in Figure 5.2.b. However, we noticed a slight decrease of the contact angle for the 20 minutes' growth with a value measured around 100°. It is important to mention that these SEM characterizations were performed on four distinct samples, grown successively on the same day, using exactly the same growth recipe. The growth was stopped by interrupting the III and V fluxes, and lowering the substrate temperature to 330°C. We have to note that this procedure could modify the catalyst droplet due to an oxidation in contact with air. However, the strong correlation between the experiments and simulations validates the relevance of the procedure.

Coupling these measurements to the RHEED IRs analysis, provides indirect but strong evidences of the growth of an extended WZ segment. Indeed, the presence of the droplet revealed by SEM imaging after a 20-minute growth, using a V/III flux ratio of 4.0, suggests that the growth of the WZ segment could be extended even further.

In order to investigate further the presence of the WZ structure and the phase transitions between ZB and WZ in a single NW, we used high-resolution (aberration-corrected) high angle annular dark field (HAADF) imaging in scanning transmission electron microscopy (STEM) mode, as well as dark-field (DF)-TEM imaging. Figure 5.6.a shows a HAADF-STEM overview of a single NW after the 45-minute growth (first stage standard growth followed by 20 minutes with a V/III flux ratio of 4.0). The NW initially crystallizes in the ZB phase as predicted from simulations in Figure 5.2.b, expected from the RHEED observation in Figure 5.3.b and evidenced by the atomic structure revealed by the HAADF-STEM image in Figure 5.6.c. The transition region between the ZB and the WZ phases consists of alternate WZ and ZB domains, as highlighted by the sharp contrast variations in the DF-TEM image shown in Figure 5.6.b and by the HAADF – STEM image in Figure 5.6.d, where the domains are delimited by the yellow lines. This specific transition was the last one observed before the 1.3 µm long WZ segment evidenced in the DF-TEM image obtained using the $[1\bar{1}00]$ g vector, specific to the WZ phase, as shown in Figure 5.6.b. Only two stacking faults are visible in the whole segment and are pointed with red arrows, dividing the long WZ segment into 3 sub-segments of 620 nm, 180 nm and 480 nm. Nevertheless, considering the total length of the extended WZ and the presence of only 2 stacking faults inside it, we considered this segment as a pure-WZ segment. Furthermore, we confirmed the WZ structure by high-resolution HAADF-STEM imaging, as shown in Figure 5.6.e and Figure 5.6.f. However, it is important to mention the presence of few atomic planes corresponding to the ZB structure under the droplet as visible on the right side of Figure 5.6.f. These ZB MLs were expected due to the lower contact angle, close to the critical value $\beta_2$, in the 85 – 100° range[9].

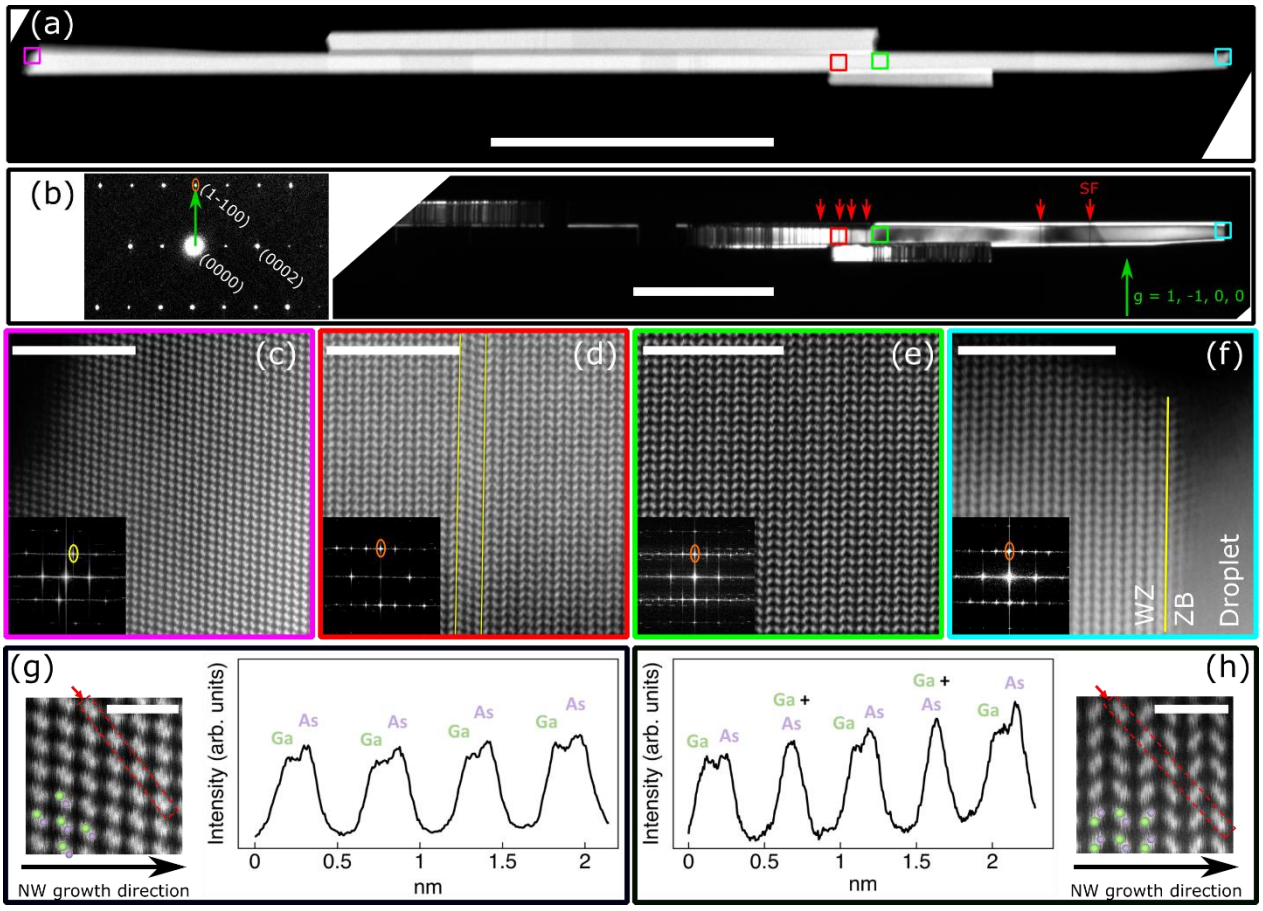


Figure 5.6. (a) HAADF-STEM overview of a single NW. Broken pieces of other NWs are visible at the top and bottom. Scale bar is 1 µm. (b) Diffraction pattern and DF-TEM image of the extended WZ segment with red arrows indicating stacking faults in the WZ segment. Scale bar is 500 nm. High-resolution HAADF-STEM images showing (c) the foot of the NW with a ZB crystalline structure, (d) the beginning of the extended WZ segment with a 3MLs long ZB inclusion, (e) a portion of the extended WZ segment and (f) the end of the extended WZ segment with the Ga droplet / NW interface. (c)-(f) correspond to the regions highlighted with colored squares, magenta, red, green, and cyan, respectively, in (a) and (b). The ZB and WZ spots of the FFTs are highlighted with the yellow and orange circles, respectively. Scale bars in (c)-(f) are 5 nm. The ZB structure in (c), (d) and (g) is observed in the $[1\bar{1}0]$ zone axis, and the WZ structure in (e), (f) and (h) is seen in the $[11\bar{2}0]$ zone axis. (g) and (h) High-resolution HAADF-STEM image and intensity profile of the ZB segment near the NW foot and of the WZ segment near the NW head, respectively. Scale bars in (g) and (h) are 1 nm. The overlayed atomic models of WZ and ZB highlight the Ga (green) and As (purple) atomic column positions, and were made using the VESTA software.[18,19]

By investigating further the NW atomic structure and analyzing the relative intensity of HAADF profiles obtained across the Ga – As pairs dumbbell (illustrated in Figure 5.6.g and h), we identified the position of the Ga and As atomic columns. Indeed, the HAADF imaging conditions result in contrasted images in which the intensity scales proportionally to $Z^2$, where Z is the atomic number of the elements[20]. Hence, a higher intensity is expected for As atoms compared to Ga ones, as measured in Figure 5.6.g and h, providing evidence that As atoms are positioned toward the top of the NW. This NW is As-polarized, in agreement with the expected polarity of the ZB and WZ crystal phases of the GaAs NWs[21].

The last part of this work consists in the photoluminescence (PL) study of the sample. It should be noted that the specific high refractive index of the NWs, leading to waveguiding properties, induce a strong dependence of the absorption efficiency on the incident light wavelength λ[22].

In order to understand the absorption phenomenon occurring in a single NW as a function of λ, we performed finite difference time domain (FDTD) simulations using Rsoft FullWAVE software. Considering a single GaAs NW, indicated by the white dashed lines in Figure 5.7, illuminated with a plane wave propagating along a direction parallel to the NW axis (*y*-axis) with a transverse polarization (along the *x*-axis), and exhibiting a WZ segment on its top, we determined an absorption profile as a function of the crystal structure. As shown in Figure 5.7, the absorption is strongly localized in the upper part of the NW (WZ section) when λ = 532 nm, whereas the absorption is mainly observed in the bottom part (ZB section) when λ = 671 nm.

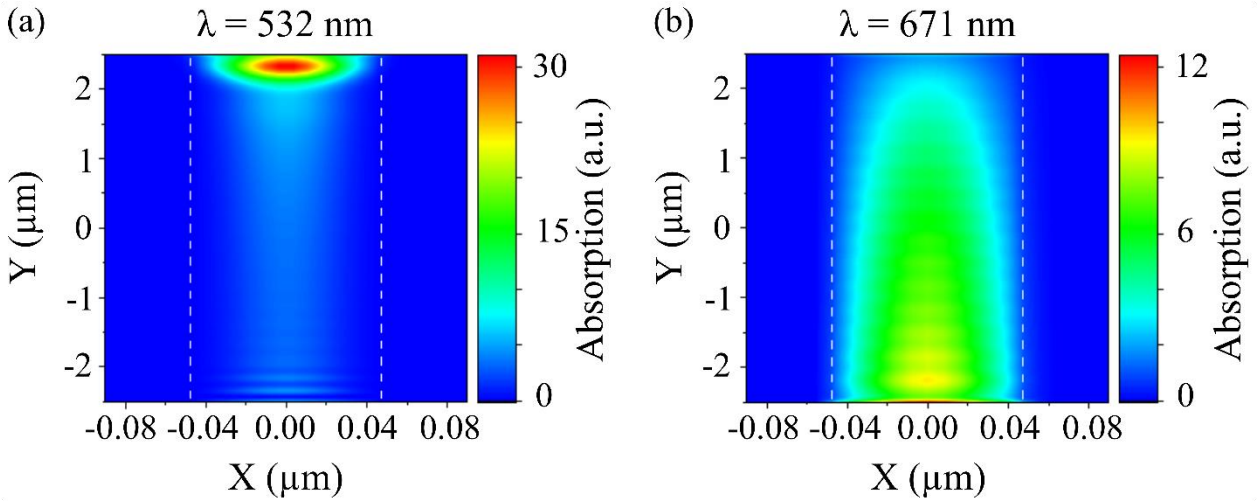


Figure 5.7. Absorption profile for a 2D – cut along the NW growth axis, illuminated with plane waves of (a) 532 nm and (b) 671 nm.

Low temperature (12 K) PL measurements were performed on our extended WZ sample, using a 532 nm and 671 nm continuous wave optical excitation at low excitation power (21 W/cm²), revealing a broad emission in the 1.46 – 1.49 eV range, as shown in Figure 5.8.a. This energy is already known to be related to a type II ZB / WZ emission[23,24]. By exciting the sample with a λ = 671 nm laser, we observed a peak at 1.516 eV, shown by the peak A on the red line, which is 3 meV below the low temperature band gap of the ZB structure of GaAs (1.519 eV). If this peak A is related to the recombination of free excitons, then their recombination energy should be equal to:

$$E = E_{gap} + E_{strain} + E_{QC} - E_{binding}, \qquad (5.9)$$

where $E_{strain}$, $E_{QD}$ and $E_{binding}$ are the energy shifts induced by the strain, the quantum confinement and the exciton binding energy, respectively. Therefore, the strain in our NWs can be neglected due to the absence of shell used to passivate the GaAs. Furthermore, the NWs are standing straight, and not lying on

the substrate, thus avoiding any substrate-induced strain during the sample cooling[25,26]. Meanwhile, the quantum confinement is weak, or inexistent. Moreover a 1-2 meV confinement energy is expected for a cylindrical shaped ZB GaAs NW, with a 90-100 nm diameter, according to the formula developed by N. Yamamoto *et al* [27]. Furthermore, an exciton binding energy in the order of 4.2 meV has been reported for the bulk ZB GaAs[28,29]. Therefore, the peak A emission energy agrees with the recombination of free excitons in ZB GaAs and with a laser absorption in the lower part of the NWs.

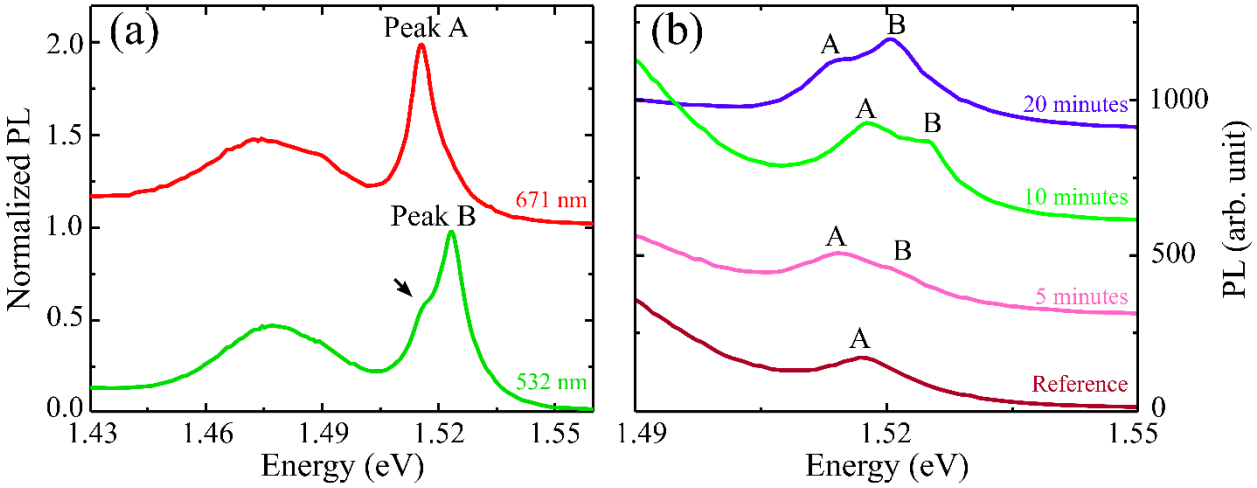


Figure 5.8. (a) Photoluminescence spectra of the sample at 12 K for a 671 nm excitation wavelength (red line) and a 532 nm excitation wavelength (green line). The spectra were normalized to the strongest emission peak and offset for clarity. (b) Close-up view on the peaks related to free excitons measured for different samples. Dark red line corresponds the standard growth, exhibiting only a ZB structure. Pink, green and purple lines represents the standard growth followed by a WZ growth of 5 minutes, 10 minutes and 20 minutes, respectively. The spectra were offset vertically for clarity. Figure adapted from ref [18].

For a 532 nm excitation wavelength, the PL emission is quite different, it is dominated by a peak at 1.5235 eV (peak B), whereas the peak A appears as a low-energy shoulder, highlighted by the arrow in Figure 5.8.a. Indeed, the peak B is only observed when a WZ structure is grown on the upper part of the NWs as shown in Figure 5.8.b, where a single peak (A) is observed on the reference ZB sample at 1.517 eV, which is closed to the ZB GaAs reference band gap of 1.519 eV[30]. When a WZ segment is grown on the upper part of the NWs, we observed the appearance of a second peak (B), 7 – 8 meV above peak A. The intensity of the peak B, compared to the intensity of peak A increases along with the length of the grown WZ section. Consequently, peak B is assumed to be related to the free exciton recombination in the WZ segment of the NWs, which is in agreement with the strong absorption of the 532 nm lase in the upper part of the NWs, as shown in Figure 5.7.a. Furthermore, these results are in agreement with low temperature PL studies performed by other groups on WZ GaAs NWs grown by metalorganic vapor-phase epitaxy (catalyst-free) or by MBE (gold or manganese catalysts)[31–33], where WZ emissions were observed at 1.522 eV[31], 1.519 eV[32] and 1.518 eV. However, to determine the low temperature band gap of WZ GaAs, we must consider the quantum confinement and the exciton binding energy contributions. Performing the

calculations using the dielectric constant $\varepsilon_0 = \sqrt{\varepsilon_0^{\perp}\varepsilon_0^{\parallel}} = 12.77$, determined by A. De's group[34] and an exciton reduced mass $\mu$ = 0.05 – 0.06 from M. De Luca's group[35] led to a quantum confinement (1 – 2 meV) and a binding energy (4 – 5 meV) for the WZ GaAs very similar to the ZB GaAs ones. From these values, we estimated a band gap for the WZ GaAs located about 6 – 9 meV above the gap of its cubic counterpart. It is worth noting the narrowness of the peaks measured. Indeed, linewidths of around 7 meV for the peak A and 8.5 meV for the peak B, are comparable or better than the 7 meV[31] and 18 meV[32] values reported for non – passivated WZ GaAs NWs. Furthermore, these results are close to the 4 meV linewidth obtained on single passivated NWs[33,36].

## 5.4 Conclusion

In summary, we used numerical simulations to provide a set of parameters intended to stabilize the contact angle of the Ga droplet in self-assisted GaAs nanowires grown by MBE for an extended time. An extended pure WZ segment longer than one micrometer was obtained, experimentally demonstrating the applicability of our theoretical model. Evidences of a 1.3 – 1.5 µm-long extended WZ segment, grown using a V/III flux ratio of 4.0, were provided using high-resolution HAADF-STEM and DF-TEM analysis, supported by RHEED analysis performed using the techniques developed in chapter 4. Furthermore, the luminescence properties of the NWs were investigated by PL measurements, showing the spectral dependence on the crystalline phase.

In this chapter, we thus demonstrated that a precise tuning of the As flux opens the way to control the length of pure WZ crystalline segments in self-assisted GaAs nanowires. The growth of pure WZ self-assisted GaAs nanowires could possibly be achieved with the constant tuning of the As flux over time, modified through a RHEED feedback loop to compensate the variation of the amount of Ga supplied to the droplet during the transient regime. This combined experimental and numerical study is of major interest to tune the properties of III-V nanostructures on demand, and to fabricate semiconducting heterostructures with novel functionalities, such as the growth of hexagonal Ge by MBE[37].

## 5.5 References

1. Fadaly, E. M. T. *et al.* Direct Bandgap Emission from Hexagonal Ge and SiGe Alloys. *Nature* **580**, 205–209 (2020).

2. Plante, M. C. & LaPierre, R. R. Control of GaAs nanowire morphology and crystal structure. *Nanotechnology* **19**, 495603 (2008).

3. Caroff, P., Bolinsson, J. & Johansson, J. Crystal Phases in III--V Nanowires: From Random Toward Engineered Polytypism. *IEEE J. Select. Topics Quantum Electron.* **17**, 829–846 (2011).

4. Dheeraj, D. L. *et al.* Controlling crystal phases in GaAs nanowires grown by Au-assisted molecular beam epitaxy. *Nanotechnology* **24**, 015601 (2013).

5. Soda, M. *et al.* Transition from Au to pseudo-Ga catalyzed growth mode observed in GaAs nanowires grown by molecular beam epitaxy. *Phys. Rev. B* **85**, 245450 (2012).

6. Lehmann, S., Jacobsson, D. & Dick, K. A. Crystal phase control in GaAs nanowires: opposing trends in the Ga- and As-limited growth regimes. *Nanotechnology* **26**, 301001 (2015).

7. Jackson, J. B., Kapoor, D., Jun, S.-G. & Miller, M. S. Integrated silicon nanowire diodes and the effects of gold doping from the growth catalyst. *Journal of Applied Physics* **102**, 054310 (2007).

8. Schmidt, V., Wittemann, J. V., Senz, S. & Gösele, U. Silicon Nanowires: A Review on Aspects of their Growth and their Electrical Properties. *Adv. Mater.* **21**, 2681–2702 (2009).

9. Panciera, F. *et al.* Phase Selection in Self-catalyzed GaAs Nanowires. *Nano Lett.* **20**, 1669–1675 (2020).

10. Jansen, M. M. *et al.* Phase-Pure Wurtzite GaAs Nanowires Grown by Self-Catalyzed Selective Area Molecular Beam Epitaxy for Advanced Laser Devices and Quantum Disks. *ACS Appl. Nano Mater.* **3**, 11037–11047 (2020).

11. Dursap, T. *et al.* Crystal phase engineering of self-catalyzed GaAs nanowires using a RHEED diagram. *Nanoscale Adv.* **2**, 2127–2134 (2020).

12. Glas, F., Harmand, J.-C. & Patriarche, G. Why Does Wurtzite Form in Nanowires of III-V Zinc Blende Semiconductors? *Phys. Rev. Lett.* **99**, 146101 (2007).

13. Vettori, M. *et al.* Impact of the Ga flux incidence angle on the growth kinetics of self-assisted GaAs nanowires on Si(111). *Nanoscale Adv.* **1**, 4433–4441 (2019).

14. Krogstrup, P. *et al.* Structural Phase Control in Self-Catalyzed Growth of GaAs Nanowires on Silicon (111). *Nano Lett.* **10**, 4475–4482 (2010).

15. Dubrovskii, V. G. *et al.* Diffusion-induced growth of GaAs nanowhiskers during molecular beam epitaxy: Theory and experiment. *Phys. Rev. B* **71**, 205325 (2005).

16. Tchernycheva, M. *et al.* Au-assisted molecular beam epitaxy of InAs nanowires: Growth and theoretical analysis. *Journal of Applied Physics* **102**, 094313 (2007).

17. Dubrovskii, V. G., Sibirev, N. V., Harmand, J. C. & Glas, F. Growth kinetics and crystal structure of semiconductor nanowires. *Phys. Rev. B* **78**, 235301 (2008).

18. Dursap, T. *et al.* Wurtzite phase control for self-assisted GaAs nanowires grown by molecular beam epitaxy. *Nanotechnology* **32**, 155602 (2021).

19. Momma, K. & Izumi, F. *VESTA 3* for three-dimensional visualization of crystal, volumetric and morphology data. *J Appl Crystallogr* **44**, 1272–1276 (2011).

20. Chou, M. Y., Cohen, M. L. & Louie, S. G. Theoretical study of stacking faults in silicon. *Phys. Rev. B* **32**, 7979–7987 (1985).

21. de la Mata, M. *et al.* Polarity Assignment in ZnTe, GaAs, ZnO, and GaN-AlN Nanowires from Direct Dumbbell Analysis. *Nano Lett.* **12**, 2579–2586 (2012).

22. Mokkapati, S., Saxena, D., Tan, H. H. & Jagadish, C. Optical design of nanowire absorbers for wavelength selective photodetectors. *Sci Rep* **5**, 15339 (2015).

23. Spirkoska, D. *et al.* Valence band structure of polytypic zinc-blende/wurtzite GaAs nanowires probed by polarization-dependent photoluminescence. *Phys. Rev. B* **85**, 045309 (2012).

24. Vainorius, N. *et al.* Observation of type-II recombination in single wurtzite/zinc-blende GaAs heterojunction nanowires. *Phys. Rev. B* **89**, 165423 (2014).

25. Anufriev, R. *et al.* Impact of substrate-induced strain and surface effects on the optical properties of InP nanowires. *Appl. Phys. Lett.* **101**, 072101 (2012).

26. Senichev, A. *et al.* Electronic properties of wurtzite GaAs: A correlated structural, optical, and theoretical analysis of the same polytypic GaAs nanowire. *Nano Res.* **11**, 4708–4721 (2018).

27. Yamamoto, N., Bhunia, S. & Watanabe, Y. Polarized cathodoluminescence study of InP nanowires by transmission electron microscopy. *Appl. Phys. Lett.* **88**, 153106 (2006).

28. Sell, D. D. Resolved Free-Exciton Transitions in the Optical-Absorption Spectrum of GaAs. *Phys. Rev. B* **6**, 3750–3753 (1972).

29. Nam, S. B. *et al.* Free-exciton energy spectrum in GaAs. *Phys. Rev. B* **13**, 761–767 (1976).

30. Ehrenreich, H. & Spaepen, F. *Solid state physics.* vol. 61 (Amsterdam ; Boston : Academic Press, 2009).

31. Martelli, F. *et al.* Photoluminescence of Mn-catalyzed GaAs nanowires grown by molecular beam epitaxy. *Nanotechnology* **18**, 125603 (2007).

32. Chuang, L. C. *et al.* GaAs nanoneedles grown on sapphire. *Appl. Phys. Lett.* **98**, 123101 (2011).

33. Furthmeier, S. *et al.* Long exciton lifetimes in stacking-fault-free wurtzite GaAs nanowires. *Appl. Phys. Lett.* **105**, 222109 (2014).

34. De, A. & Pryor, C. E. Optical dielectric functions of wurtzite III-V semiconductors. *Phys. Rev. B* **85**, 125201 (2012).

35. De Luca, M. *et al.* Addressing the Fundamental Electronic Properties of Wurtzite GaAs Nanowires by High-Field Magneto-Photoluminescence Spectroscopy. *Nano Lett.* **17**, 6540–6547 (2017).

36. Lu, Z., Shi, S., Lu, J. & Chen, P. Photoluminescence of the single wurtzite GaAs nanowire with different powers and temperatures. *Journal of Luminescence* **152**, 258–261 (2014).

37. Dudko, I. *et al.* Hexagonal Ge Grown by Molecular Beam Epitaxy on Self-Assisted GaAs Nanowires. *Crystal Growth & Design* **22**, 32–36 (2022).

# 6 Combined aberration-corrected STEM and synchrotron nano-diffraction for crystal phase engineering in GaAs nanowires

## Chapter contents



### 6.1 Introduction

Controlling the crystalline structure of self-assisted GaAs NWs appears as an important step for the integration of such gold-free nano-objects in modern electronic and optoelectronic devices[1]. In addition to their different properties, the ZB and WZ phases present slightly different lattice parameters[2,3]. Phase changes could induce local deformation (compression, expansion, torsion, bending) at the interface of the different structures, and it is well known that such deformation can alter the properties of the NWs. Indeed, the modification of the optical properties of substrate-strained InP NWs was reported in 2012 by R. Anufriev[4], while P. Sutters *et al.* recently described the change of the electronic structure and optoelectronic properties of van der Waals GeS NWs induced by the twisting of the lattice along the NW long axis[5]. It is

now common knowledge that the electronic mobility can be tuned through strain in GaAs NWs[6]. While J. Lähnemann *et al.* and S. Hammarberg *et al.* investigated the influence of the crystal phase on the emission of (In, Ga)As/GaAs NWs core/shell quantum wells[7] and on the strain implied by GaInP and InP sequences inside a NW[8], we studied in detail the strains and tilts induced by the phase changes inside GaAs NWs. Cubic ZB GaAs exhibits a lattice parameter $a$ = 5.6533 Å[9], and the hexagonal WZ GaAs lattice parameters were experimentally determined equal to $a$ = 3.9845 Å and $c$ =6.5701 Å[10]. Subsequently, the inter-reticular distance $d_{hkl}$ becomes accessible using the equation ( 6.1 ) for the ZB structure or equation ( 6.2 ) for the WZ structure.

$$d_{hkl} = \frac{a}{\sqrt{h^2 + k^2 + l^2}}, \qquad (6.1)$$

$$d_{hkl} = \frac{1}{\sqrt{\frac{4}{3a^2}(h^2 + hk + k^2) + \frac{l^2}{c^2}}}. \qquad (6.2)$$

A lattice mismatch of about 0.6% along the [111] growth axis and of about -0.3% perpendicularly to the growth direction. The mismatch between ZB and WZ GaAs can induce strain and an accommodation of the inter-reticular distance[11].

During the last decade, U. Pietsch's group has intensively investigated the structural properties of GaAs NWs by XRD characterization on arrays of NWs[12–14] and more recently on single NW[15,16]. The influence of a bending induced by the growth of an asymmetrical shell was studied[12], as well as *in situ* growth characterization using synchrotron facilities[17,18].

In this chapter, we investigate the relaxation and deformation mechanisms involved in a NW with different crystal structures, using the high reciprocal-space resolution of synchrotron nano-diffraction. These characterizations were combined with high-resolution STEM and DF-TEM analyses performed on the same individual NW, using the same diffraction spots as for nano-diffraction. Finally, a linear elasticity model was used to simulate the relaxation of the inter-reticular distance induced by the phase change along the NW.

The MBE growths, RHEED interpretations, SEM and STEM images were performed by myself. The nano-diffraction experiments and results interpretations were carried out in collaboration with Marie-Ingrid Richard and Maxime Dupraz from the European Synchrotron Radiation Facility, Grenoble, Stephane Labat and Olivier Thomas from the Institut Matériaux Microélectronique et Nanosciences de Provence, Marseille and Tao Zhou from the Argonne National Laboratory. The nano-diffraction data were treated by Marie-Ingrid Richard from the European Synchrotron Radiation Facility, Grenoble. The FIB lamella was realized by Solène Brottet from INL. The DF-TEM images were obtained by Nicholas Blanchard from the Institut Lumière Matière, Lyon. Finally, the numerical simulations were developed in collaboration with Niels Fardeau from INL.

## 6.2 Structural properties of a single GaAs nanowire

### 6.2.1 Sample preparation and characterization setup

The self-assisted GaAs NWs were grown by MBE using the method described in the previous chapters. As indicated in chapter 5, the growth was initiated with a "buffer" length during 20 minutes, followed by modifications of the As pressure, as illustrated in Figure 6.1.a. The switching from ZB to WZ was observed using the RHEED diagram along the $[1\bar{1}0]$ azimuth at different times during the growth. This procedure led to the fabrication of NWs exhibiting pure ZB, pure WZ, as well as highly mixed phases segments. The NWs obtained (Figure 6.1.k) were measured with a length of about 4.0 ± 0.3 µm and a diameter and density of about 80 ± 10 nm and 1.8 NW/µm², respectively.

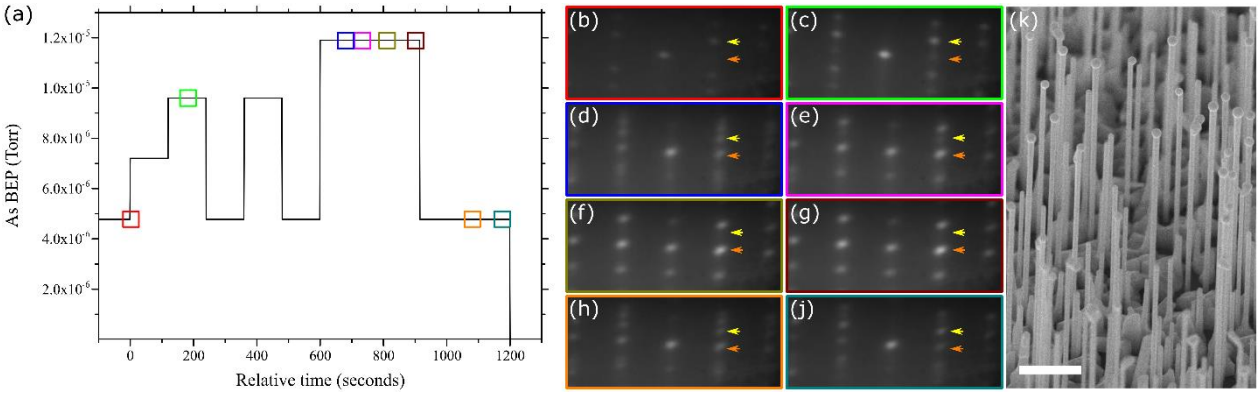


Figure 6.1. (a) Graphic representing the As BEP variation during the growth. The time $t$ = 0 sec represents the start of the change of As following the 20 minutes growth under standard conditions. (b)-(j) RHEED pattern snapshots recorded during the growth along the $[1\bar{1}0]$ azimuth, where only the ZB and WZ spots are highlighted by yellow and orange arrows, respectively. (k) 45°-tilted SEM image of the NWs after the growth. Scale bar is 1 µm.

Therefore, the NWs were studied at Hard X-ray Nanoprobe beamline 26-ID of the Advanced Photon Source (APS) at Argonne National Laboratory. A photon energy of 10.4 keV was used to probe the fluorescence signal of Ga ($K_{\alpha 1}$ = 9.252 keV). The beam was focused down to a 25 nm diameter probe using a Fresnel zone-plate. The order sorting aperture used to filter the direct beam as well as higher diffraction orders from the zone-plate was positioned at 3 mm upstream from the sample.

The NWs were randomly drop-casted onto a 10 µm thick silicon substrate, transparent to hard X-rays. All investigated NWs had their *a*-plane $(2\bar{1}\bar{1}0)$ facet parallel to the Si substrate.

### 6.2.2 Diffraction, *d*-spacing and internal strain

The first step of this experiment consisted in locating the position of an individual GaAs NW on the Si substrate, using a scanning probe nano-fluorescence. Once located, the fluorescence signal of Ga was measured, and a series of Bragg reflections were recorded for different beam positions on the NWs. A two-dimensional (2D) Pilatus detector, positioned at 0.9 m from the sample was used to record the diffraction patterns. Therefore, diffraction patterns were recorded at four different GaAs diffraction peaks, sensitive

either to the WZ or ZB structures of the GaAs NW. The combined scanning nano-fluorescence and nano-diffraction measurements allow to locate the position of the ZB and WZ segments all along the NW, as well as their associated strain state. The vertical NW orientation enabled two different Bragg peaks to be accessed in the horizontal scattering plane. Indeed, we measured the $[10\bar{1}0]$ WZ planes and the $[2\bar{1}\bar{1}0]$ WZ planes, which is equivalent to the $[20\bar{2}]$ ZB planes. The $[10\bar{1}0]$ WZ Bragg peak reveals the location and deformation of the WZ segments of the NW, while the $[2\bar{1}\bar{1}0]$ WZ-equivalent to the $[20\bar{2}]$ ZB peaks are sensitive to both the WZ and ZB segments of the NW. Then, a "hybrid" reflection $[11\bar{1}]$ was measured, corresponding to the ZB planes and containing information about the in-plane and out-of-plane ZB structure, as well as the fourth reflection $[\bar{1}\bar{1}3]$, which is sensitive to the twinned ZB structure (as described in the previous chapter) denoted hereafter TZB. Figure 6.2 displays the location in reciprocal space of three of the measured reflections.

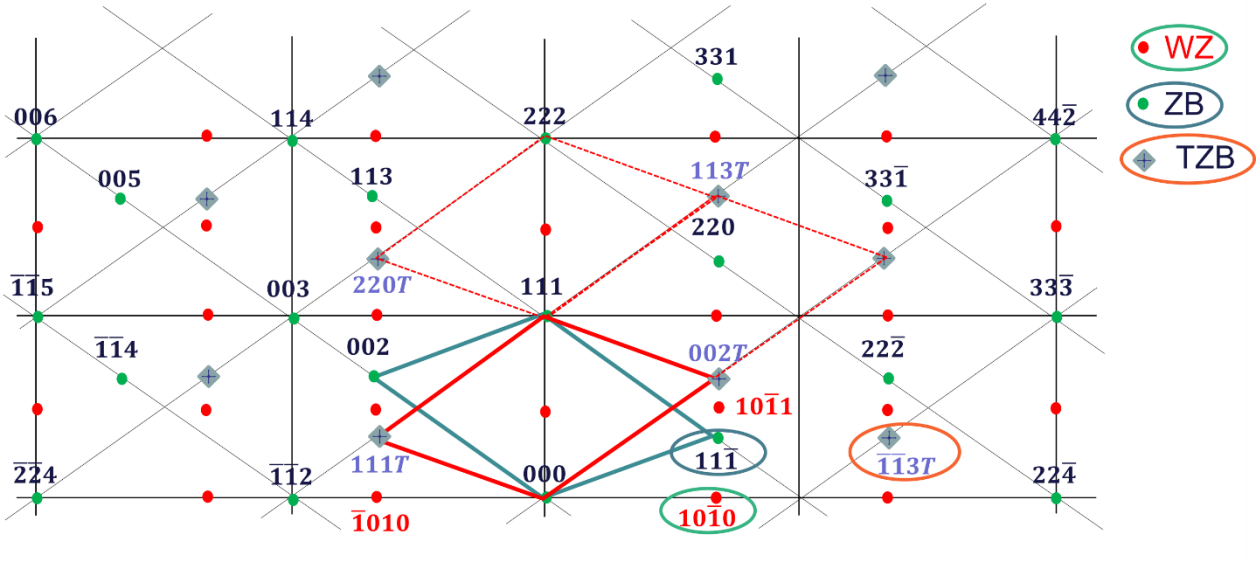


Figure 6.2. Simplified schematic representation of the electron diffraction pattern along a $[1\bar{1}0]$ azimuth. The green, blue and orange circles highlight the spots used to discriminate the different crystal structures in the NW.

The results of the combined scanning nano-fluorescence and nano-diffraction measurements of the $[2\bar{1}\bar{1}0]$ WZ planes-equivalent to the $[20\bar{2}]$ ZB planes is shown in Figure 6.4.a (Ga K-edge fluorescence) and Figure 6.4.b (integrated intensity of the measured Bragg reflection). The bright spot visible at the bottom right of Figure 6.4.a corresponds to a fragment of another NW. The 2D nano-diffraction maps were obtained by measuring a series of angles around the Bragg peak, to disentangle the lattice strain of the measured (*hk.l*) planes, while simultaneously measuring the Ga K-edge fluorescence. Furthermore, the 2D maps were obtained by moving the NW with horizontal or vertical translations with 20 nm or 25 nm steps, respectively. Moreover, the angle was adjusted with 0.2° steps around the Bragg condition with a rotational stage used to rotate the NW around its long axis. The scans were then systematically stopped before the foot of the NW in order to avoid the diffraction of the small fragment observed in Figure 6.4.a.

Subsequently, the reciprocal space coordinates $Q_x$, $Q_y$ and $Q_z$ (defined in Figure 6.3) of the center of mass of the measured Bragg peaks have been determined for each position scanned, $Q_x$ being horizontal and parallel to the beam direction, and $Q_z$ being vertical. Figure 6.4.c displays the 2D map of the *d*-spacing ($d_{hkl} = \sqrt{2\pi/(Q_x^2 + Q_y^2 + Q_z^2)}$) of the reflection obtained from the 2D nano-diffraction map and clearly reveals distinct regions along the NW. A first determination of the location of the different crystal phases was obtained by plotting the variation of the *d*-spacing along the NW as shown in Figure 6.4.d, and by comparing the measured values (red line) to the theoretical *d*-spacing for the WZ (green dashed-line) and the ZB (blue dashed-line) structures. A WZ segment of about 500 nm long was identified at the top of the NW, and two smaller WZ segments were observed in the middle of the NW. This distribution of the WZ (and thus ZB) structure was expected from the growth parameters used during the fabrication of this sample, shown in Figure 6.1.

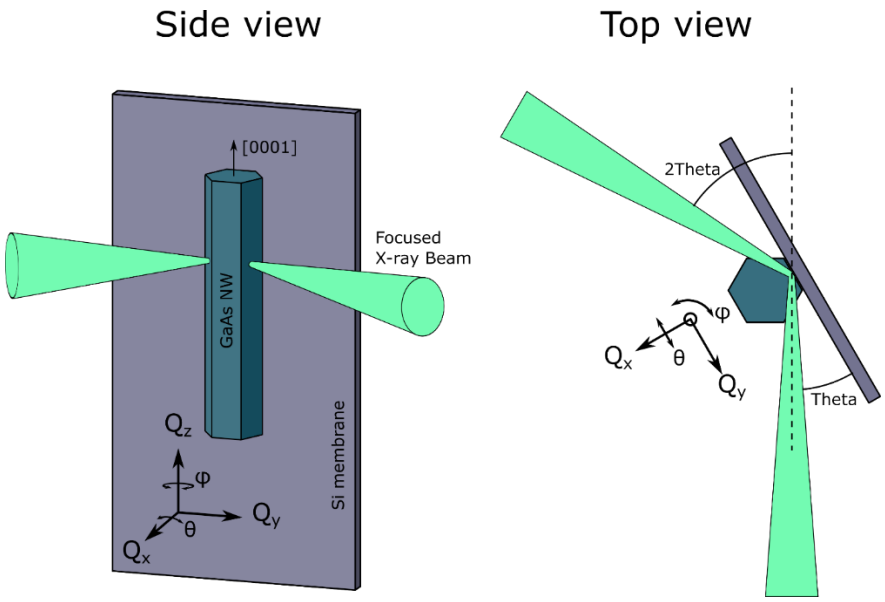


Figure 6.3. Schematic showing the side view and top view orientation of the system. The azimuthal angle $\varphi$, corresponding to the torsion along the long axis of the NW, and the tilt / orientation angle $\theta$, representing the bending of the NW of the (*hk.l*) planes are represented regarding the NW orientation.

Furthermore, the experimental measurement of the $d_{hkl}$ for the $[20\bar{2}]$ (ZB) / $[2\bar{1}\bar{1}0]$ (WZ) planes obtained in Figure 6.4.c and Figure 6.4.d allow a simple computation of the lattice parameter observed. Using the equations ( 6.1 ) and ( 6.2 ), lattice parameters $a_{ZB,\,exp}$ = 5.6554 Å and $a_{WZ,\,exp}$ = 3.9866 Å were calculated, corresponding to a difference with the theoretical values of about 0.04% and 0.05%, respectively. It is important to note that the planes observed in this experiment did not give access to the WZ lattice parameter *c*. However, it is possible to estimate this parameter using the *c/a* ratio, equal to $\sqrt{8/3} = 1.633$. A lattice parameter $c_{exp}$ = 6.5101 Å was obtained, corresponding to a mismatch with the experimental value of about 0.9% measured by D. Jacobsson[10]. Nonetheless, M. I. McMahon *et al.* demonstrated in 2005 the existence

of a slight larger value of the *c/a* ratio, equal to 1.6455[2]. Using this value leads to a lattice parameter $c_{exp}$ = 6.5599 Å, corresponding to a difference of 0.1% with the experimental results obtained by D. Jacobsson[10].

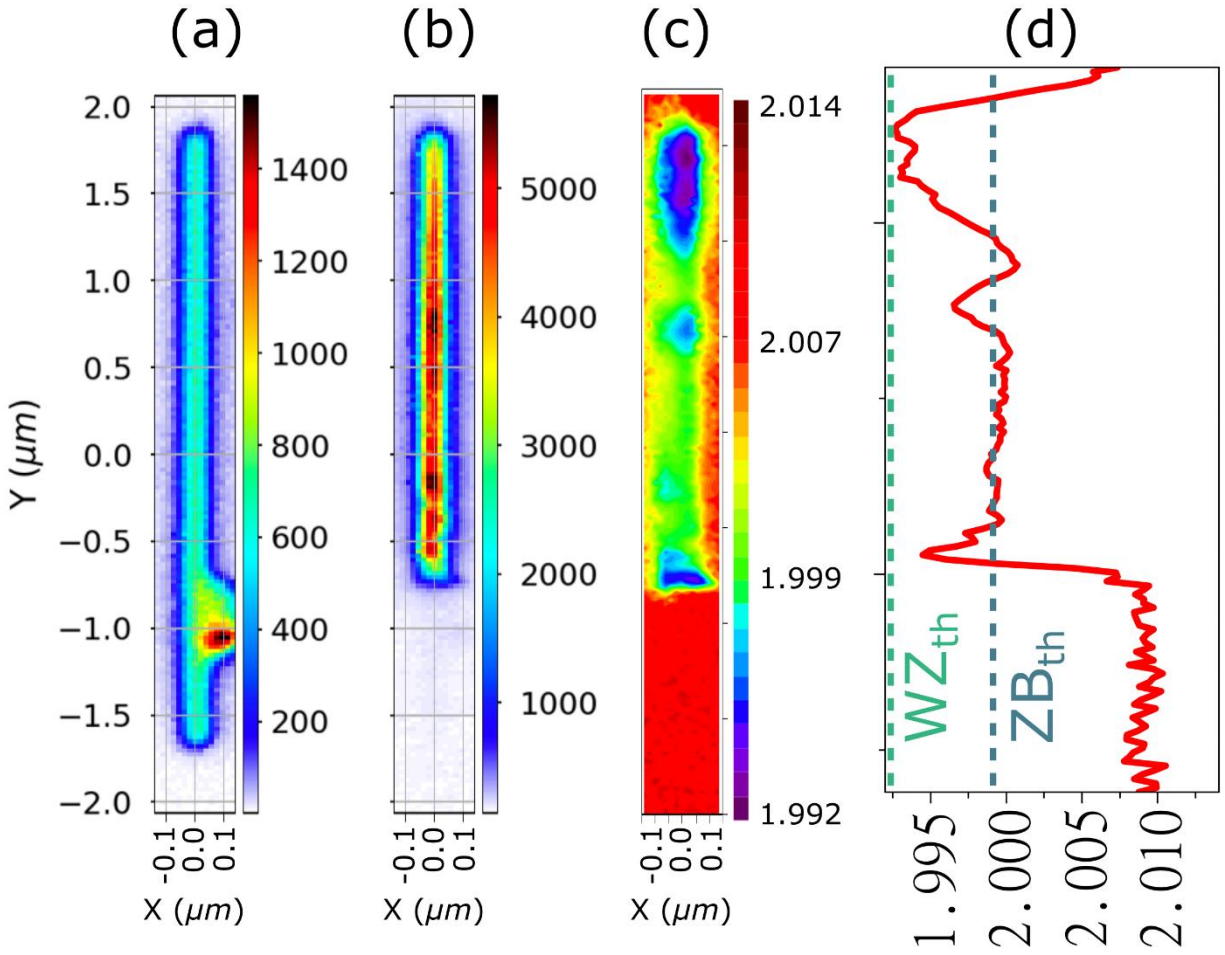


Figure 6.4. (a) Ga K-edge fluorescence map of a single NW. A broken NW is visible at the bottom right of the image. (b) Color map of the integrated intensity of the Bragg reflections obtained along the $[20\bar{2}]$ (ZB) / $[2\bar{1}\bar{1}0]$ (WZ) planes. (c) Color map representing the evolution of the $d_{hkl}$ along the NW. (d) Profile of the *d*-spacing plotted from the integration of the color map (c). The green and blue dashed lines represent the theoretical values of the $d_{hkl}$ for the WZ and the ZB structures, respectively.

The same characterization procedure was used to study the $[11\bar{1}]$ ZB, $[\bar{1}\bar{1}3]$ TZB and $[10\bar{1}0]$ WZ planes, as shown in Figure 6.5.a, Figure 6.5.b and Figure 6.5.c, respectively. Furthermore, the strain along the [*hkl*] direction, $\varepsilon_{hkl}$, was retrieved from the 2D maps of the *d*-spacing: $\varepsilon_{hkl} = \frac{d_{hkl} - \bar{d}_{hkl}}{\bar{d}_{hkl}}$, where $\bar{d}_{hkl}$ corresponds to the measured average *d*-spacing along the NW. Strains in the range -0.4% to 0.4% were observed all along the wire.

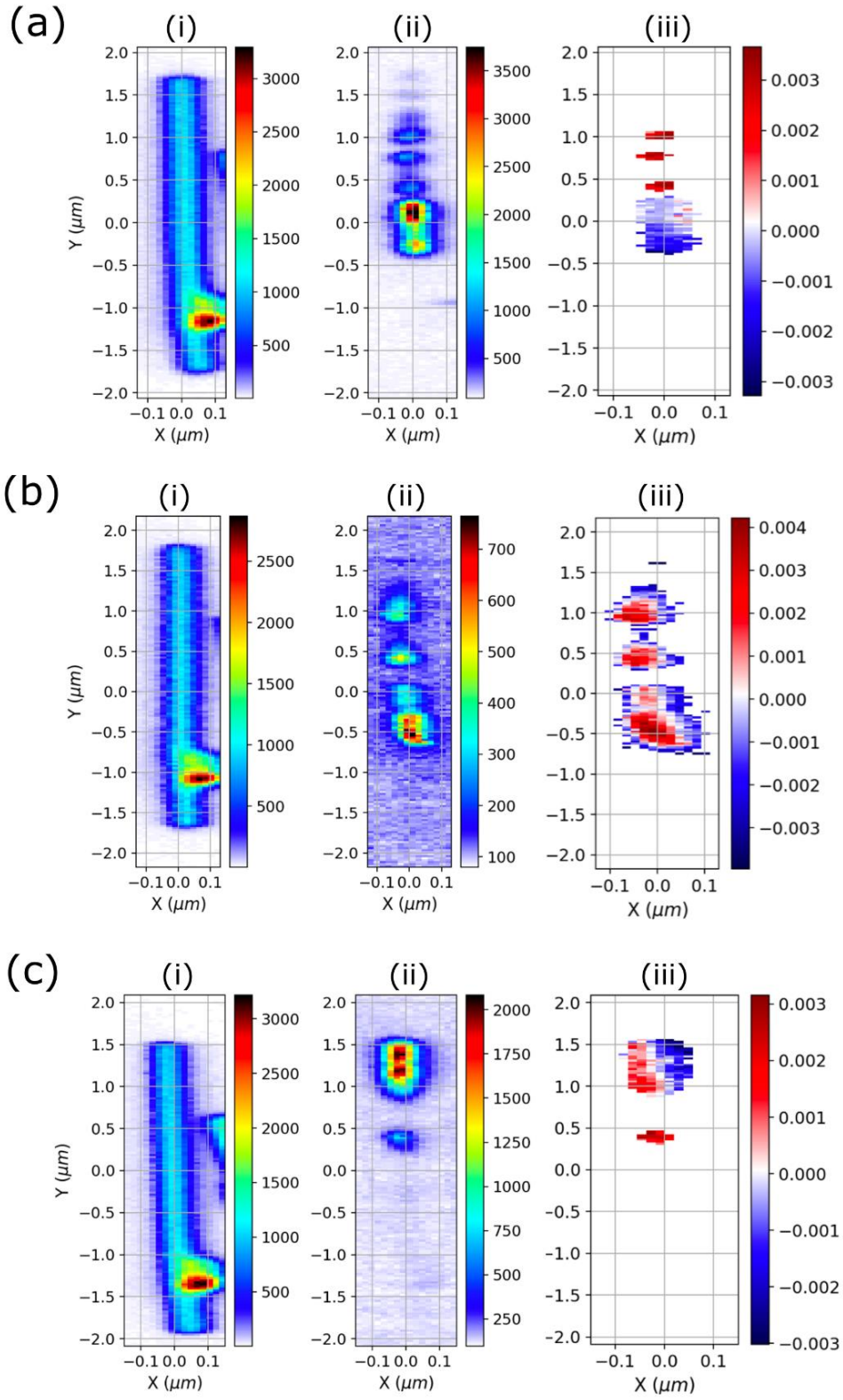


Figure 6.5. (i) 2D map of the Ga K-edge fluorescence, (ii) integrated intensity and (iii) 2D map of the strain $\varepsilon$ measured for the (a) $[11\bar{1}]$, (b) $[\bar{1}\bar{1}3]$ and (c) $[10\bar{1}0]$ Bragg reflections.

The azimuthal angle $\varphi$, corresponding to the torsion along the long axis of the NW, and the tilt/orientation angle $\theta$, representing the bending of the NW of the measured (*hkl*) planes were measured and are represented in Figure 6.3. It is possible to obtain information about these angles using $\varphi = \arctan(Q_y/Q_x)$ and $\theta = \arccos(Q_z/Q)$. Large variations were observed between the bottom, close to the fragment of NW, and the top of the NW, as shown in Figure 6.6. Nonetheless, it is important to notice the presence of small lattice misorientations at the top of the NW only, away from the fragment. While the influence of the substrate on the torsion or bending of the NW cannot be excluded, the angular variations match the presence of either ZB or WZ crystal structures.

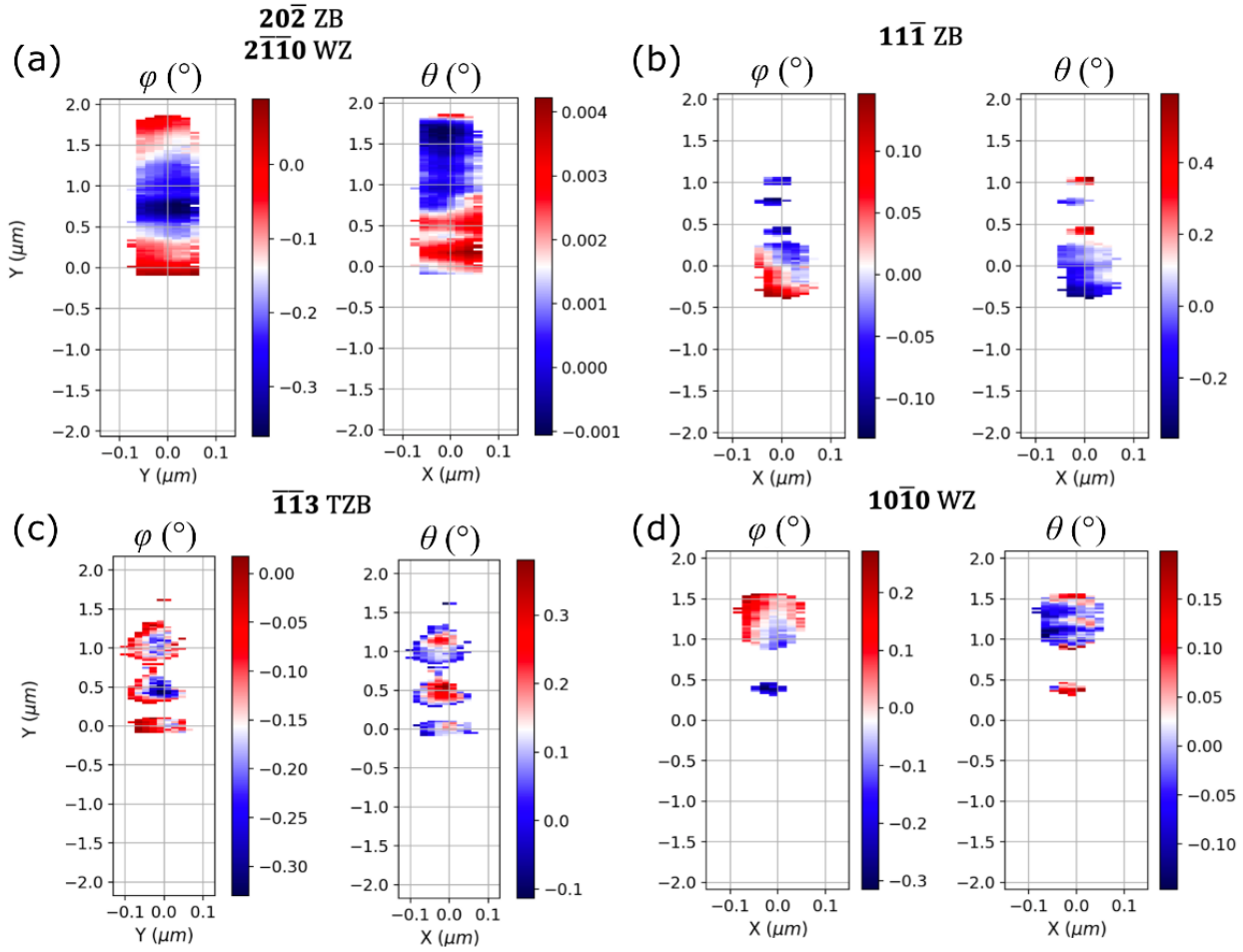


Figure 6.6. 2D maps of the azimuthal angle $\varphi$, corresponding to the torsion along the long axis of the NW, and the tilt / orientation angle $\theta$, representing the bending of the NW of the (*hk.l*) planes: (a) $[20\bar{2}]$ (ZB) / $[2\bar{1}\bar{1}0]$ (WZ), (b) $[11\bar{1}]$ (ZB), (c) $[\bar{1}\bar{1}3]$ (TZB) and (d) $[10\bar{1}0]$ (WZ). Maps represented for the top part of the NW (Y > -0.1 μm) to avoid contribution from the NW fragment.

This spatial correlation between the presence of a crystal phase and the torsion and tilt is further illustrated on the line profiles of Figure 6.7, obtained from the integration of the 2D map in Figure 6.6. Indeed, a negative torsion and positive bending is observed in the WZ segments. The bending and torsion appeared stronger in the highly defected WZ section, in comparison with the pure-WZ section. Further investigations should be performed in order to clarify the origin of both the torsion and bending. Indeed, the comparison between the elastic energy stored in the NW and the adhesion energy could be a first suggestion to determine the origin of the bending and torsions.

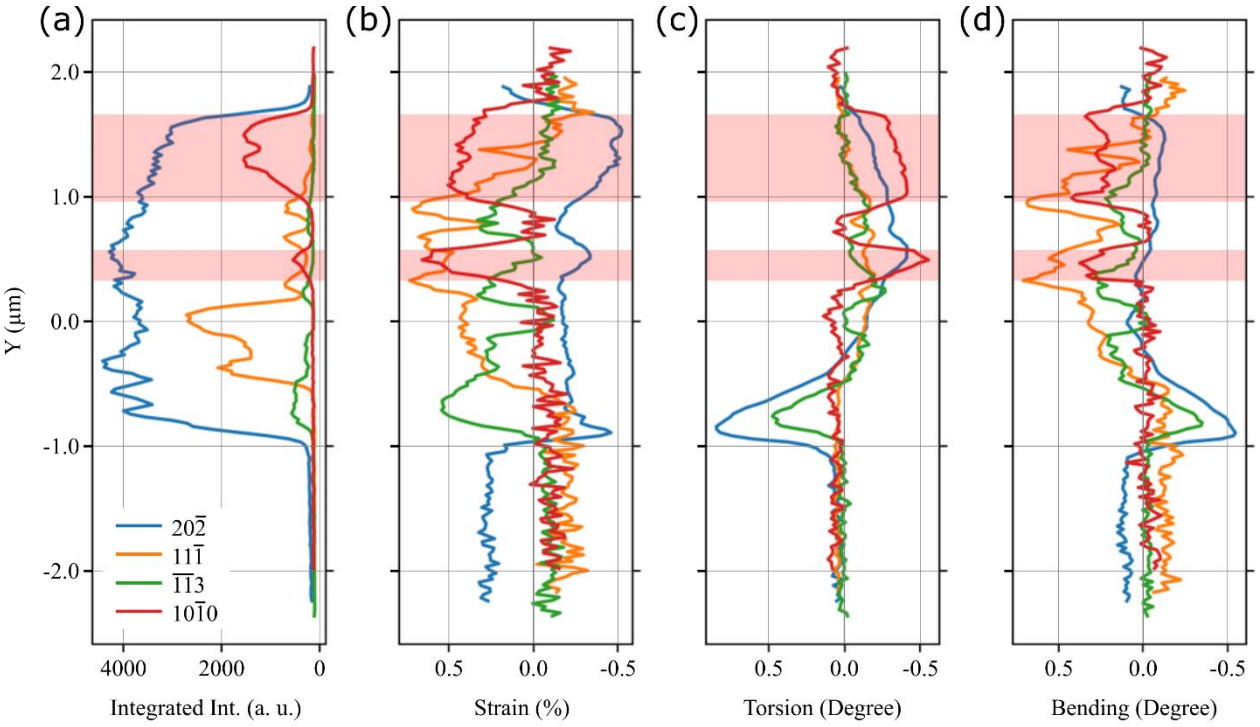


Figure 6.7. Profiles of the (a) integrated intensity, (b) strain, (c) torsion and (d) bending obtained for the $[20\bar{2}]$ / $[2\bar{1}\bar{1}0]$ (blue lines), $[11\bar{1}]$ (orange lines), $[\bar{1}\bar{1}3]$ (green lines) and $[10\bar{1}0]$ (red lines). Red areas highlight the localization of the WZ phase on the NW.

### 6.2.3 Combined TEM and diffraction characterization

In order to perform STEM and DF-TEM imaging, the NW studied by X-ray nano-diffraction was extracted into a TEM lamella using focused ion beam (FIB) preparation, allowing a combined characterization on a single NW. The location of the NW on the Si substrate was performed using SEM imaging, prior to FIB milling. Top and side views of the lamella are provided in Figure 6.8. The position of the isolated NW is highlighted in yellow.

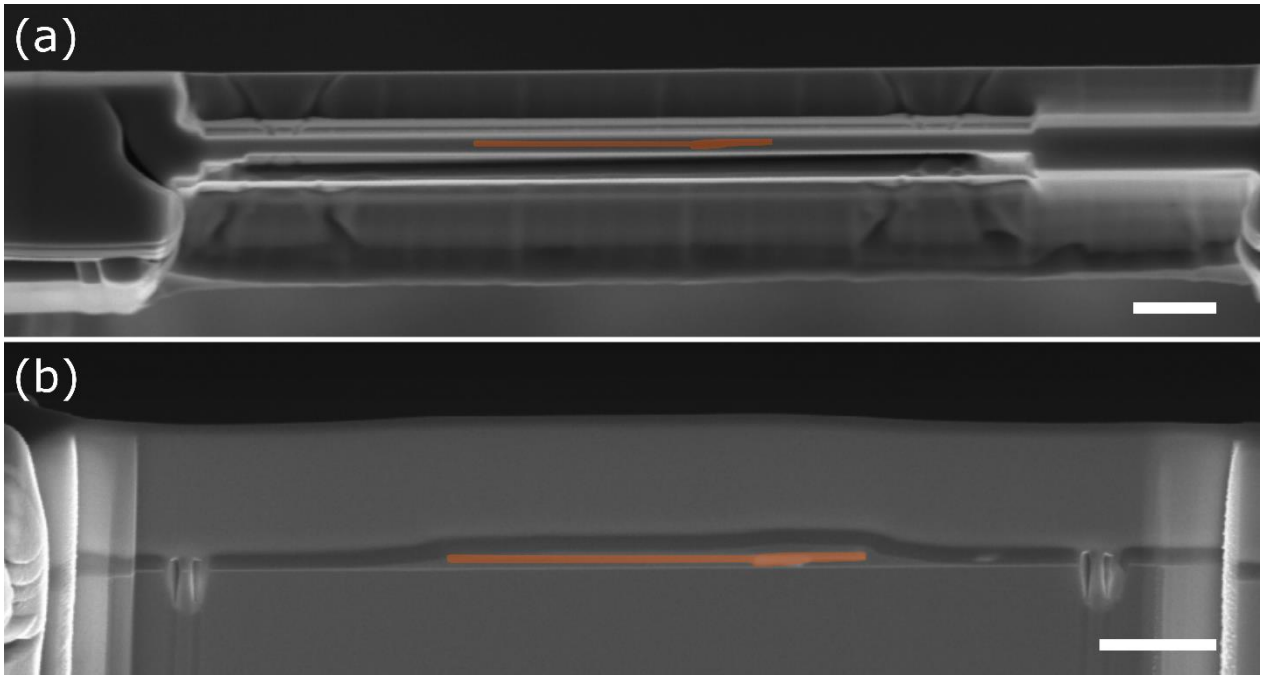


Figure 6.8. SEM images showing the (a) top view and (b) side view of the FIB lamella. The NW position is highlighted in yellow. Scale bars are 1 µm.

High-resolution STEM-HAADF was performed on the NW, as shown in Figure 6.9. The structure of the NW at specific locations (Figure 6.9.b-f) confirms the nano-diffraction observation (Figure 6.9.a) of the pure WZ (Figure 6.9.b), ZB (Figure 6.9.e), TZB (Figure 6.9.f), mixed ZB (Figure 6.9.d) and mixed phases (Figure 6.9.c). Despite the great correlation between the nano-diffraction and high-resolution STEM imaging, the information obtained here is only relevant on specific locations. To obtain a more general overview of the NW's structure, DF-TEM was performed. Indeed, by selecting the appropriate diffraction spots, it is possible to obtain the dark field image using the electrons diffracted by specific crystallographic planes.

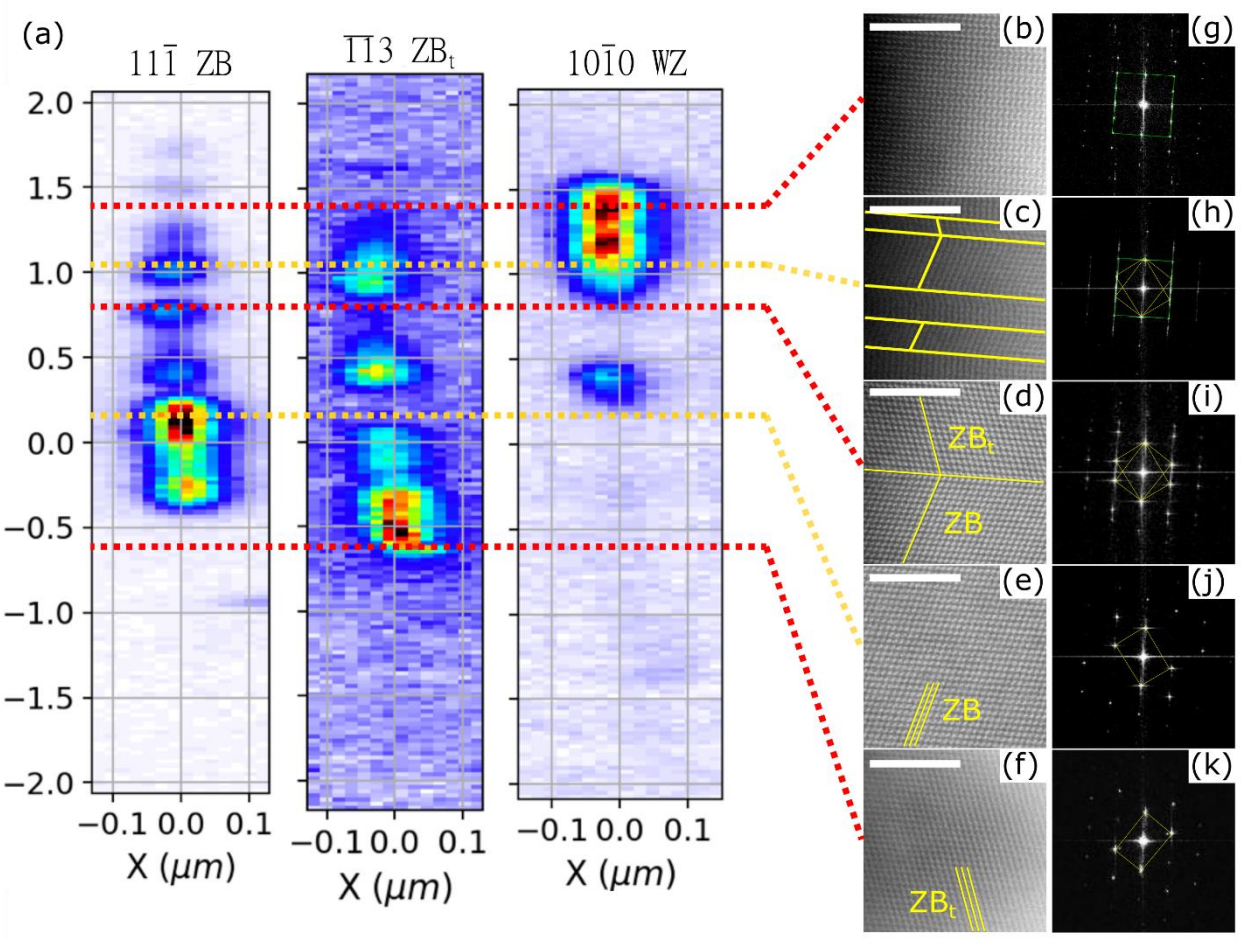


Figure 6.9. (a) Color mapping of the integrated intensity of different reflections, showing the distribution of the ZB, ZB$_t$ and WZ structure. (b-f) High-resolution STEM-HAADF images along the [1$\bar{1}$0] zone axis showing the crystal structure at specific position highlighted by the blue and orange dashed lines on (a). Scale bars are 5 nm. (g-k) FFTs associated to the HR-STEM images on (b-f), respectively. (g), (j) and (k) FFTs show the typical diffraction pattern of the WZ, ZB and ZB$_t$ structures, respectively.

By selecting similar diffraction spots as in the nano-diffraction experiments, images of the NW showing only the ZB, the TZB or the WZ were obtained, as illustrated in Figure 6.10.a-c (i, ii), respectively, revealing the pure phase segments and the mixed phase portions. Comparing the DF-TEM observation with the in-plane strain 2D maps shown in Figure 6.10.a-c (iii) reveals a slight compression of the lattice parameter in the highly WZ defects area.

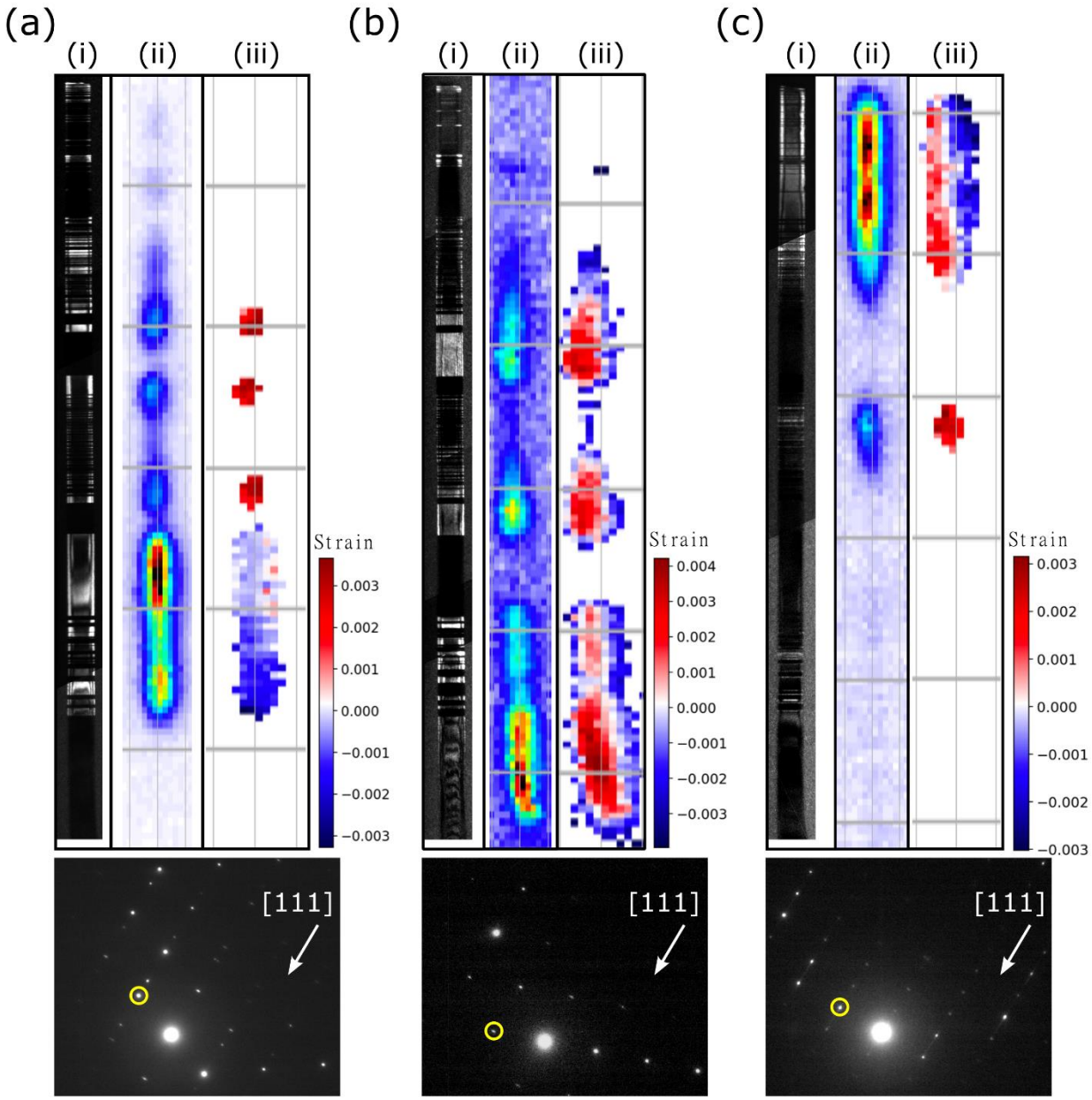


Figure 6.10. (i) DF-TEM image, (ii) integrated intensity and (iii) internal strain color map observed along the NW for the (a) $[1\bar{1}0]$, (b) $[\bar{1}\bar{1}3]$ and (c) $[10\bar{1}0]$ planes highlighting the contribution of the ZB, $ZB_t$ and WZ crystal structures, respectively.

Furthermore, in order to determine the deformation of the lattice parameter along the NW, numerical simulations were performed, using the DF-TEM as input data. Image processing was first developed in the work of N. Fardeau[19], and was used to identify the phase location within the DF-TEM images. The DF-TEM image was converted into a numerical matrix, representing the intensity of each pixel of the image. Since the phase transition only occurs along the long axis of the NW, an intensity profile was calculated by summing the intensity along the width of the NW. The intensity profile obtained was then processed using

a Butterworth low-pass filter of order 2, using a wavelength $\lambda_c$ = 1 nm. Indeed, the variations smaller than $\lambda_c$ are mainly related to the noise of the measurements and can be neglected.

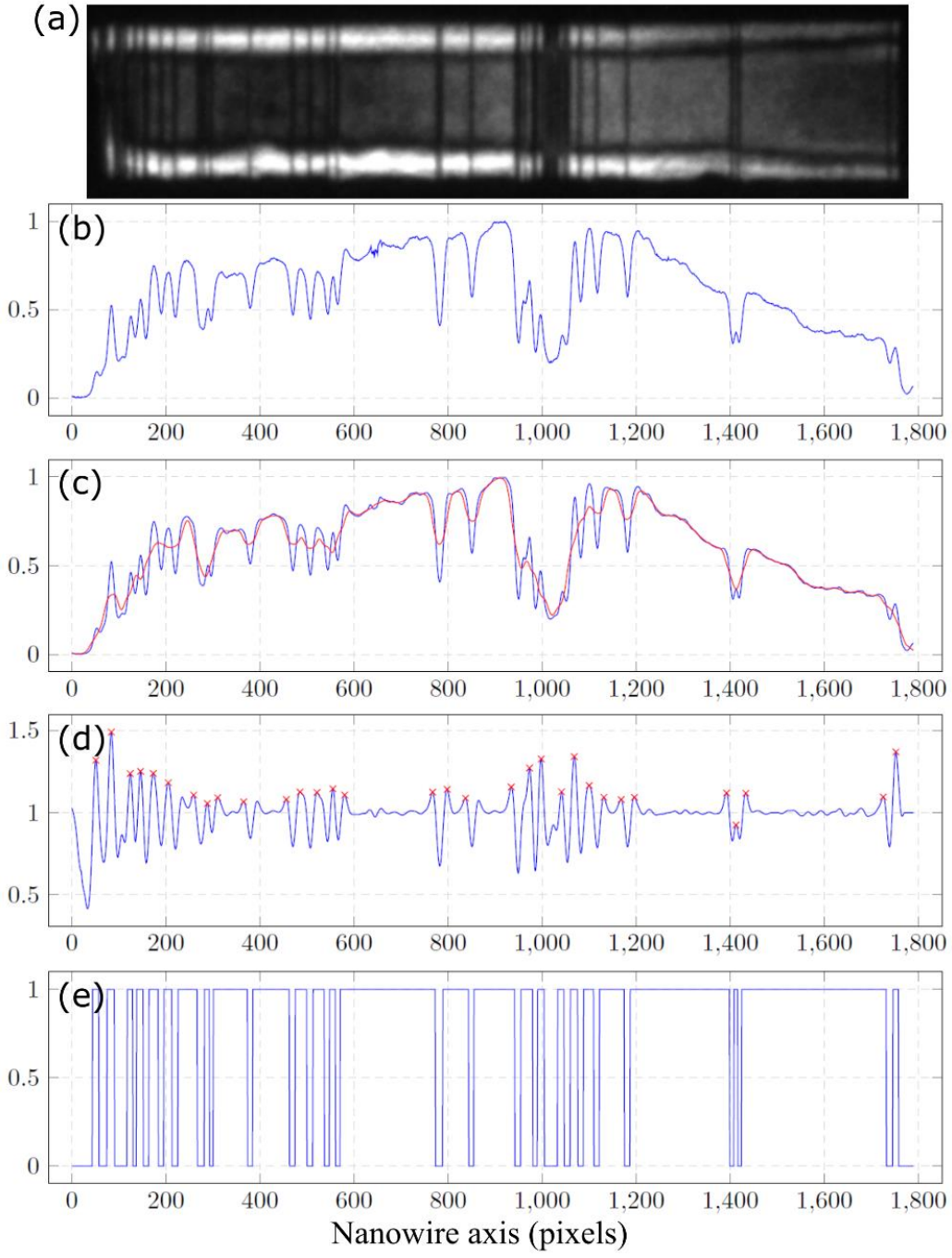


Figure 6.11. (a) DF-TEM image of the top of the NW, showing the [$10\bar{1}0$] WZ. (b) Raw intensity profile summed along the width of the NW. (c) Intensity signal after noise reduction (blue line) and average values calculated using the Savitzky-Golay filter (red line). (d) Corrected intensity profile (blue line) and detected maxima (red crosses). (e) Final WZ detection determined from the DF-TEM image. A value equal to 1 corresponds to the presence of WZ while a value equal 0 designates the absence of WZ.

Two different procedures were developed to detect the intensity peaks in the profiles. On the one hand, if the intensity profile only presents equivalent height peaks, a saturation of the signal was used to diminish its dynamic range and reveal the variations of small amplitude. Then, an algorithm identified local maxima and determine their location. The width of each identified peak was determined using the appropriate algorithm. On the other hand, if the signal present large variation in the peak intensities, a problem occurs in the detection of high intensity variations. To overcome this problem, an adaptive average of the signal is calculated using a Savitzky-Golay filter[20]. Indeed, this filter consists in the calculation of the central point of a sliding window using a polynomial interpolation. In our case, a 31 pixel-wide window, corresponding to about 7 nm, was used with a first order polynomial interpolator. The filtered signal is divided by the obtained adaptive average, and maxima are determined. Finally, the algorithm returns tables with values equal to 1 when the phase is detected in the DF-TEM image, and 0 elsewhere. This process was applied to the entire length of the NW for the three different phases (WZ, ZB and TZB) to obtain a complete mapping of the different structures. The entire signal processing for the detection of the WZ phase on the top part of the NW is illustrated in Figure 6.11.a-e. The final curve obtained was used as an input for the finite element approach described in the following paragraphs.

The phase mapping obtained from the procedure just-described can be used to calculate the variation of the inter-reticular distance $d_{hkl}$ along the NW axis using the equation ( 6.1 ) for the ZB structure and the equation ( 6.2 ) for the WZ structure, defined in the first part of this chapter.

To determine $d_{hkl}$, the lattice parameters *a* and *c* have to be calculated. In the pure-phase segments and for the portions away from the phase transitions, the lattice parameters were approximated to their theoretical values. However, due to the difference of lattice parameters between ZB and WZ and as evidenced from the experiment (Figure 6.10) a deformation of the crystal is expected close to the phase-change zones, thus slightly modifying the values of the lattice parameters to accommodate the variations[9,10].

Subsequently, the inter-reticular distance of the portion of NW presented in Figure 6.11.a was calculated using the WZ phase detection of Figure 6.11.e. The detailed calculation is available in the Master 2 report of N. Fardeau[19]. The results of these calculations were compared to the experimental measurements of the *d*-spacing shown in Figure 6.4.d, as illustrated in Figure 6.12.b.

From 25 to 100 nm, the calculated *d*-spacing decreases consistently and overlaps with the experimental value. At 125 nm, the calculated *d*-spacing hits a local maximum, corresponding to the phase transitions shown in Figure 6.12.a, which is not visible in the experiment. A second more intense and broader maximum is observed at ~250 nm in both experimental and calculated values. The four phase changes observed around 350 nm in Figure 6.12.a reveal another local maximum of the inter-reticular distance in both the experimental and simulated lines of Figure 6.12.b. Above 400 nm, both experimental and calculated *d*-spacing increase. The experimental results appear less sensitive to the phase changes compared to the simulations, which is very likely due to a lower resolution. Nevertheless, the trend and the main variations of experimentally-measured inter-reticular distance are reproduced by the simulations. Overall, these results highlight the strong contribution of structural transitions on the *d*-spacing.

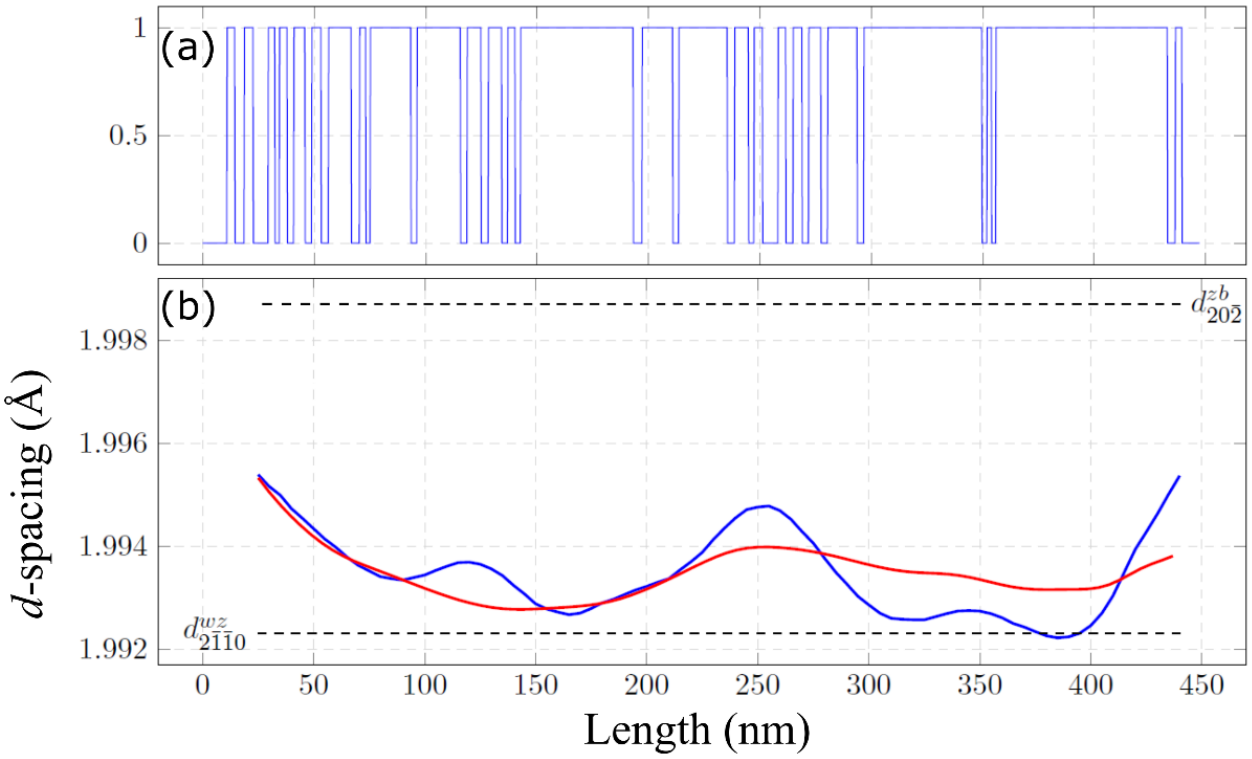


Figure 6.12. (a) WZ phase detection. A value equal to 1 corresponds to the presence of hexagonal WZ while a value equal 0 designates the presence of a cubic ZB structure. (b) Inter-reticular distance $d_{20\bar{2}}$ (ZB)/ $d_{2\bar{1}\bar{1}0}$ (WZ) measured (red line) and calculated (blue line) for an average NW diameter of 50 nm. Top and bottom dashed lines represent the theoretical values of the ZB $d_{20\bar{2}}$ and WZ $d_{2\bar{1}\bar{1}0}$ inter-reticular distances, respectively.

The here-developed methodology shows a remarkable correlation with the experiments and give the possibility to simulate the evolution of the inter-reticular distance all along the NW, using DF-TEM images as input for the phase detection. However, this process still need improvements, particularly regarding the detection of the two ZB phases (ZB and TZB).

## 6.3 Conclusion

In this chapter, the ZB and WZ structure of an individual GaAs NW were investigated using synchrotron X-ray nano-diffraction, leading to the precise measurement of their lattice parameters. A difference of about 0.04% between the lattice parameter of the ZB structure was observed, as well as a difference of 0.05% and 0.1% for the *a* and *c* parameters of the WZ structure, respectively, placing these measurements in a close range with the TEM observations of D. Jacobsson's group[10]. Combining these results with high resolution STEM-HAADF and DF-TEM imaging, the existence of strain was carefully correlated at the nanoscale with the alternation of ZB and WZ crystal structures along the NW growth axis, and was shown to be responsible of the slight lattice parameter variations. In addition, the presence of bending (and torsion) seems to match the presence of ZB and WZ crystal structures. A linear elasticity model was made to predict the evolution of the *d*-spacing induced by the structural transitions, using DF-TEM images of the different structures as

input. The calculated *d*-spacing reproduces the experimental data, supporting the correlation of the *d*-spacing variations with the structural transitions. These results call for further investigations and characterizations to fully understand the mechanisms leading to the strain and torsion/bending observed, as well as their consequences on the NW properties.

## 6.4 References

1. Fadaly, E. M. T. *et al.* Direct Bandgap Emission from Hexagonal Ge and SiGe Alloys. *Nature* **580**, 205–209 (2020).

2. McMahon, M. I. & Nelmes, R. J. Observation of a Wurtzite Form of Gallium Arsenide. *Phys. Rev. Lett.* **95**, 215505 (2005).

3. *Springer handbook of condensed matter and materials data*. (Springer, 2005).

4. Anufriev, R. *et al.* Impact of substrate-induced strain and surface effects on the optical properties of InP nanowires. *Appl. Phys. Lett.* **101**, 072101 (2012).

5. Sutter, P., Wimer, S. & Sutter, E. Chiral twisted van der Waals nanowires. *Nature* **570**, 354–357 (2019).

6. Balaghi, L. *et al.* High electron mobility in strained GaAs nanowires. *Nat Commun* **12**, 6642 (2021).

7. Lähnemann, J. *et al.* Correlated Nanoscale Analysis of the Emission from Wurtzite versus Zincblende (In,Ga)As/GaAs Nanowire Core–Shell Quantum Wells. *Nano Lett.* **19**, 4448–4457 (2019).

8. Hammarberg, S. *et al.* High resolution strain mapping of a single axially heterostructured nanowire using scanning X-ray diffraction. *Nano Res.* **13**, 2460–2468 (2020).

9. Saib, S. & Bouarissa, N. High-pressure band parameters for GaAs: first principles calculations. *Solid-State Electronics* **50**, 763–768 (2006).

10. Jacobsson, D. Crystal Structures in GaAs Nanowires. 110.

11. Glas, F. Strain in Nanowires and Nanowire Heterostructures. in *Semiconductors and Semimetals* vol. 93 79–123 (Elsevier, 2015).

12. Al Hassan, A. *et al.* Complete structural and strain analysis of single GaAs/(In,Ga)As/GaAs core–shell–shell nanowires by means of in-plane and out-of-plane X-ray nanodiffraction. *J Appl Crystallogr* **51**, 1387–1395 (2018).

13. Kashani, S. M. M., Dubrovskii, V. G., Baumbach, T. & Pietsch, U. In Situ Monitoring of MBE Growth of a Single Self-Catalyzed GaAs Nanowire by X-ray Diffraction. *The Journal of Physical Chemistry C* (2021) doi:10.1021/acs.jpcc.1c04255.

14. Al Hassan, A. *et al.* Beam damage of single semiconductor nanowires during X-ray nanobeam diffraction experiments. *J Synchrotron Rad* **27**, 1200–1208 (2020).

15. Bahrami, D. *et al.* Impact of Electrical Current on Single GaAs Nanowire Structure. *Phys. Status Solidi B* **258**, 2100056 (2021).

16. Davtyan, A. *et al.* X-ray diffraction reveals the amount of strain and homogeneity of extremely bent single nanowires. *J Appl Crystallogr* **53**, 1310–1320 (2020).

17. Schroth, P. *et al.* Radial Growth of Self-Catalyzed GaAs Nanowires and the Evolution of the Liquid Ga-Droplet Studied by Time-Resolved in Situ X-ray Diffraction. *Nano Lett.* **18**, 101–108 (2018).

18. Jakob, J. *et al.* Correlating *in situ* RHEED and XRD to study growth dynamics of polytypism in nanowires. *Nanoscale* **13**, 13095–13107 (2021).

19. Niels, M. Source de lumière à base de germanium hexagonal. *Master 2 Report* (2021).

20. Savitzky, Abraham. & Golay, M. J. E. Smoothing and Differentiation of Data by Simplified Least Squares Procedures. *Anal. Chem.* **36**, 1627–1639 (1964).

# 7 The fabrication of nanowire-based photoelectrodes for the water reduction / oxidation

## Chapter contents



### 7.1 Introduction

Due to their high aspect ratio, large surface area of III-V material can be obtained using the NW geometry, hence reducing the production costs of efficient photoelectrodes[1]. Indeed, an array of NWs with a length of about 3 µm for a diameter of 100 nm and a density of about 2 NW/µm² will induce an increase of the surface area by a factor 2. The NW geometry thus appears as a promising candidate to enhance the photoactivity of photoelectrochemical cells (PEC) for water splitting in comparison with their thin films counterpart[2,3]. Furthermore, the control of the morphology of such electrodes appeared as a critical factor to

enhance the efficiency and the light absorption properties of the PEC[4]. Indeed, the efficient light-trapping induced by the high aspect-ratio of III-V NWs appears to be particularly attractive for the development of new photoelectrodes for the overall light-driven water splitting[5], either as photoanodes for the OER[5–7] or as photocathodes for the HER[8–12].

The study of III-V NWs, first dedicated to their electronic and optical properties, extended in the last decade to their implementation in PEC[5,6,9,13–17]. More recently, F. Cui *et al.* reported the impact of $TiO_2$ protective shell on GaAs NW photocathodes for water splitting[10] while G. Xie *et al.* investigated the development of GaP/GaPN NWs for hydrogen production[11].

This chapter is divided in two distinct parts. Firstly, the development and characterization of GaAs NW-based photocathodes will be discussed, reporting on the advantageous NW geometry in comparison with its planar counterpart. The influence of the morphology and of the doping will further be discussed. Secondly, analogous studies performed on GaP NW-based photoanodes will be presented, aiming at the fabrication of a tandem photocathode / photoanode cell.

All the PEC measurements and result interpretations presented in this chapter were obtained by Mariam Fadel, Mathieu Koepf and Vincent Artero from CEA, Grenoble. The MBE growths of the GaAs NWs, the SEM and STEM-EELS characterizations were performed by myself. The reflectivity measurements were carried out in collaboration with Hai Son Nguyen from INL. The XPS experiments and interpretation of the results were carried out in collaboration with Hélène Magnan and Antoine Barbier from CEA, Saclay.

## 7.2 The case of the GaAs photocathode

### 7.2.1 The influence of the geometry on the photocurrent density

To investigate the effect of the geometry on the PEC performances, a 2D layer of GaAs was grown by MBE on a *p*-doped silicon substrate, as well as samples of self-assisted GaAs NWs. The self-assisted GaAs NWs were grown by MBE during 20 minutes using a V/III flux ratio of 2.4 with a Ga flux of 0.5 ML/s, using the VLS mechanism. The growth was then terminated under As atmosphere by interrupting the Ga flux, ensuring the consumption of the liquid droplet at the top of the NWs. The grown NWs exhibited a length of about 2.3 ± 0.3 µm, for a diameter of 125 ± 20 nm and a density of around 1.1 NWs/µm² and are shown on the SEM image in Figure 7.1.a. The 2D layer was grown during 2 minutes on a 1 × 1 cm² Si(111) substrate with a growth rate of 0.25 nm/s, leading to the fabrication of a thin layer of about 30 nm thick. Due to a large lattice mismatch (4.1%) between the silicon substrate and the GaAs material, structural defects are formed at the III-V interface[18]. However, we decided to grow a 2D GaAs layer on Si substrate to promote the growth of NWs on a substrate of similar chemical composition. Therefore, the only variable parameters are the volume of GaAs deposited on the substrate and the effective surface area of GaAs able to interact with the liquid electrolyte.

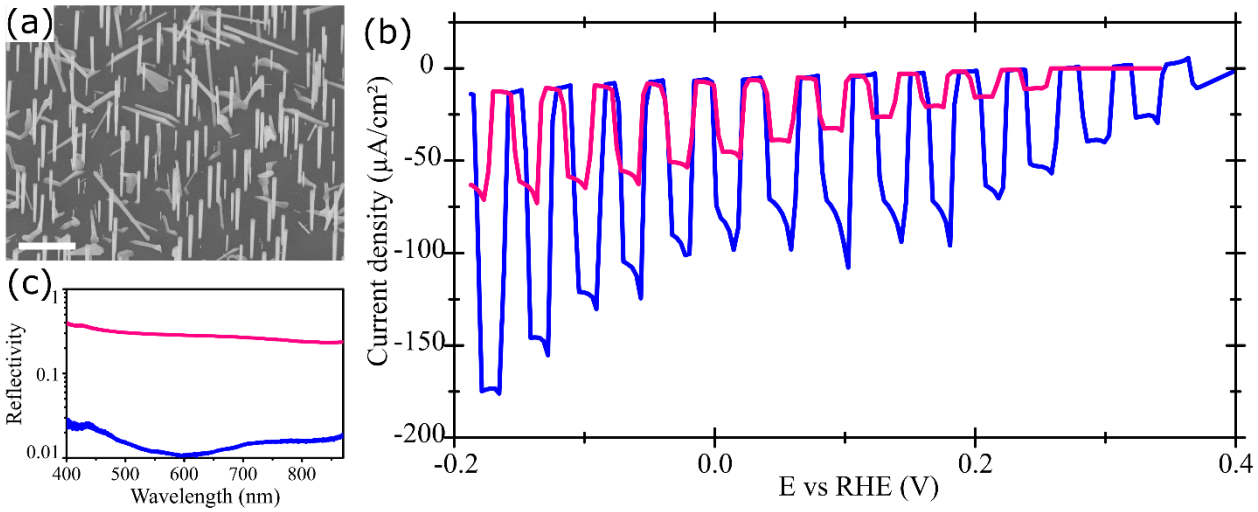


Figure 7.1. (a) SEI SEM image (30° tilted) showing the NWs after the growth. Scale bar is 2 µm. (b) Linear sweep voltammogram (10 mV/s) recorded in a nitrogen-saturated 0.1 M potassium phosphate buffer (pH 7), under chopped-light irradiation (simulated 1 sun, 1.5 AM filter). (c) Reflectivity measured on a 400-870 nm range spectrum. The *y*-axis is in log scale. Pink and blue lines in (b) and (c) correspond to the GaAs 2D layer and to the self-assisted GaAs NWs, respectively.

The length, diameter and density obtained for the NWs gives a total surface of GaAs of about 1.01 cm², on a 1 × 1 cm² Si substrate. Hence, the effective surface of GaAs exposed to the electrolyte is almost the same considering the 2D layer or NWs. Furthermore, the NW morphology led to a total volume of about $3.1 \times 10^{-6}$ cm$^3$ of GaAs deposited on the 1 × 1 cm² silicon substrate, which corresponds to the total amount of GaAs deposited for the 30-nm thick film. Finally, the SEM image in Figure 7.1.a reveals the clear appearance of the Si substrate due to the high growth temperature, with a really low density of parasitic GaAs crystallites. Therefore, the difference between the two samples can be approximated as purely geometric: 2D film *versus* NWs.

The photoelectrochemical properties of these samples were investigated in an aqueous potassium phosphate buffer (0.1 M, pH 7, KPi) chosen as electrolyte, in collaboration with the LCBM (CEA-Grenoble). The linear sweep voltammograms (LSV) were then recorded in oxygen free conditions between + 0.4 V and -0.2 V *vs* RHE. Exposing the samples to chopped-light irradiation using a Xe lamp, simulating the irradiation of 1 sun, at a power of 100 mW/cm² and an air mass of 1.5, allows the observation of clear photocurrents, as illustrated in Figure 7.1.b. Indeed, the NW sample (blue line) shows a photocurrent with an onset potential of about + 0.35 V *vs* RHE, while a lower onset potential of + 0.25 V *vs* RHE was observed for the thin film sample, with almost 2 to 2.5 times higher photocurrent recorded over the full range of explored potentials. Indeed, a photocurrent density of about 100-125 µA/cm² at 0 V *vs* RHE was measured for the NW sample compared to 50 µA/cm² at 0 V *vs* RHE for the 2D layer of GaAs. The photocurrent are here reported at 0 V *vs* RHE, corresponding to the performance obtained by interaction with the light only. Since the effective surface area of the two samples were both equal to 1.0 cm², we associated this photocurrent enhancement to the improved light-trapping efficiency of the NW sample with respect to the

thin film counterpart. Indeed, as shown in Figure 7.1.c, the NW geometry induces a reduction of the reflectivity from around 30 % down to 2 % compared to the flat sample, indicating an enhancement of the sample light absorption efficiency, and thus suggesting the interest of the nano-structuration of the GaAs materials into NWs to design improved photoelectrodes for PEC applications, in agreement with the observations of A. Javay's group[19] or E. P. A. M. Bakkers's group[8] on InP or GaP nanowires, respectively.

### 7.2.2 The influence of the morphology of the nanowires

As the NW geometry showed improved performance compared to the thin film due to better light absorption, we investigated the impact of the morphology of these objects on the photocurrent density generated under a simulated 1 sun irradiation. To investigate the influence of the morphology of the NWs, three samples were grown, exhibiting different NW morphologies as reported in Table 7.1. The length, diameter and density of the samples 1-3 were measured from SEM images, displayed in Figure 7.2.a-c. The sample 1 corresponds to the same sample as for the previous study of the geometry. The samples 2 and 3 in Figure 7.2b and Figure 7.2.c show the NWs after an extended axial growth of about 1 h and 2 h, respectively. The diameter of the NWs was then increased through radial GaAs growth at a substrate temperature of 400°C and with a V/III flux ratio of 2.4. With longer and large NWs, we aimed to increase the total effective surface area of GaAs materials exposed to the electrolyte, for a given NW density.

Table 7.1. Measured length and diameter for the different samples shown in Figure 7.2.a-c, labelled as sample 1-3, respectively.

| | Sample 1 | Sample 2 | Sample 3 |
|---|---|---|---|
| Length (in μm) | 2.3 ± 0.3 | 5.2 ± 0.4 | 9.4 ± 0.3 |
| Diameter (in nm) | 125 ± 20 | 380 ± 20 | 740 ± 0.4 |
| Density (in NWs/μm²) | 1.1 | 1.0 | 0.9 |
| GaAs surface area (in cm²) | 1.0 | 7.2 | 17.8 |

As expected, the photocurrent densities obtained by increasing the NW sizes gradually increased according to the actual GaAs surface area of the samples, as illustrated in Figure 7.2.d and Figure 7.2.e. Indeed, the smallest NWs displayed in Figure 7.2.a delivers a photocurrent of around 100-125 μA/cm² at 0 V *vs* RHE under the irradiation of 1 sun, while a value close to 310 μA/cm² was obtained at 0 V *vs* RHE under the same conditions for the thicker NWs, displayed in Figure 7.2.c.

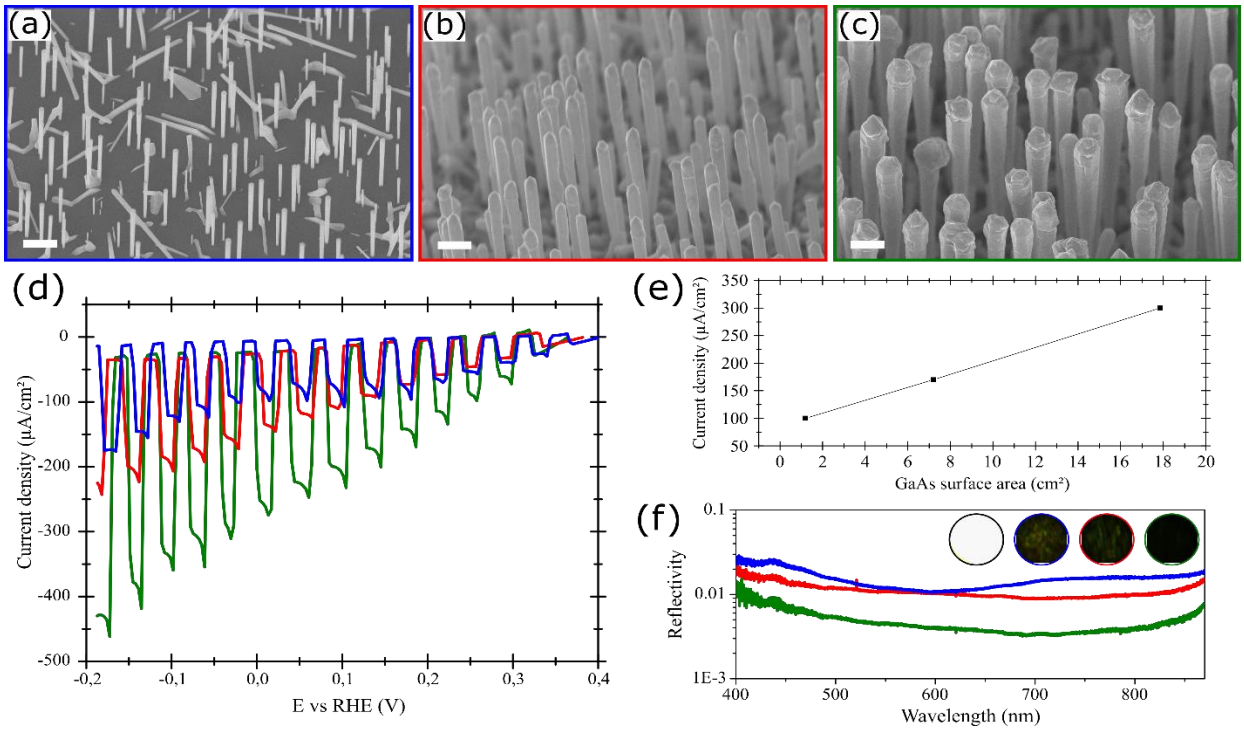


Figure 7.2. (a)-(c) SEI SEM images (30° tilted) of the NW sample showing the different morphologies obtained with the different growths. Scale bars are 1 µm. (d) PEC characterization of the 3 samples recorded at 10 mV/s in 0.1 M potassium phosphate buffer (pH 7) under nitrogen, irradiated with chopped-light (1 sun, 1.5 AM filter). (e) Current density at 0 V *vs* RHE as a function of the effective surface area of GaAs material on a 1 cm² silicon substrate. (f) Reflectivity of the samples measured on a 400-870 nm range spectrum. Blue, red and green lines in (d) and (f) correspond to the NWs samples showed in (a)-(c), respectively. Insets in (f) show pictures of the reference mirror (circled in black) and of the samples (a)-(c), circles in blue, red and green, respectively.

The improvement of the photocurrent density was attributed to the increase of the effective surface area of GaAs material in contact with the electrolyte, as shown in Figure 7.2.e. Furthermore, an enhancement of the light trapped by the NWs was measured, as reported in Figure 7.2.f, where the reflected light in the 400-870 nm spectrum range dropped from about 2 % for the smallest NWs (blue lines) down to about 0.5 % for the thickest ones (green lines). An increase of the GaAs surface area by a factor 7 led to an increase of the photocurrent density of a factor 2, with a decrease by a factor 2 of the reflected light. Finally, an increase by a factor 18 of the GaAs surface area led to an increase of the photocurrent density of a factor 3, and a diminution of the reflected light by a factor 4.

### 7.2.3 p–n junction and Co nanoparticle-enhanced photocathode

Since the HER occurs at the interface between the electrode and the liquid electrolyte, a transfer of electrons from the photocathode surface to the solution happens, caused by the potential differences between the material and the electrolyte. An increase of the PEC efficiency could be achieved by promoting electron motion to the edge of the NWs. A sample with NWs exhibiting a p–n junction was then produced, with an *n*–doped (Si-doped) shell grew around a *p*–core NW (Be-doped), as illustrated in Figure 7.3.a. This sample

was aimed for the same NW dimensions as sample 3 reported in Table 7.1. The shell was grown at a low substrate temperature (400°C).

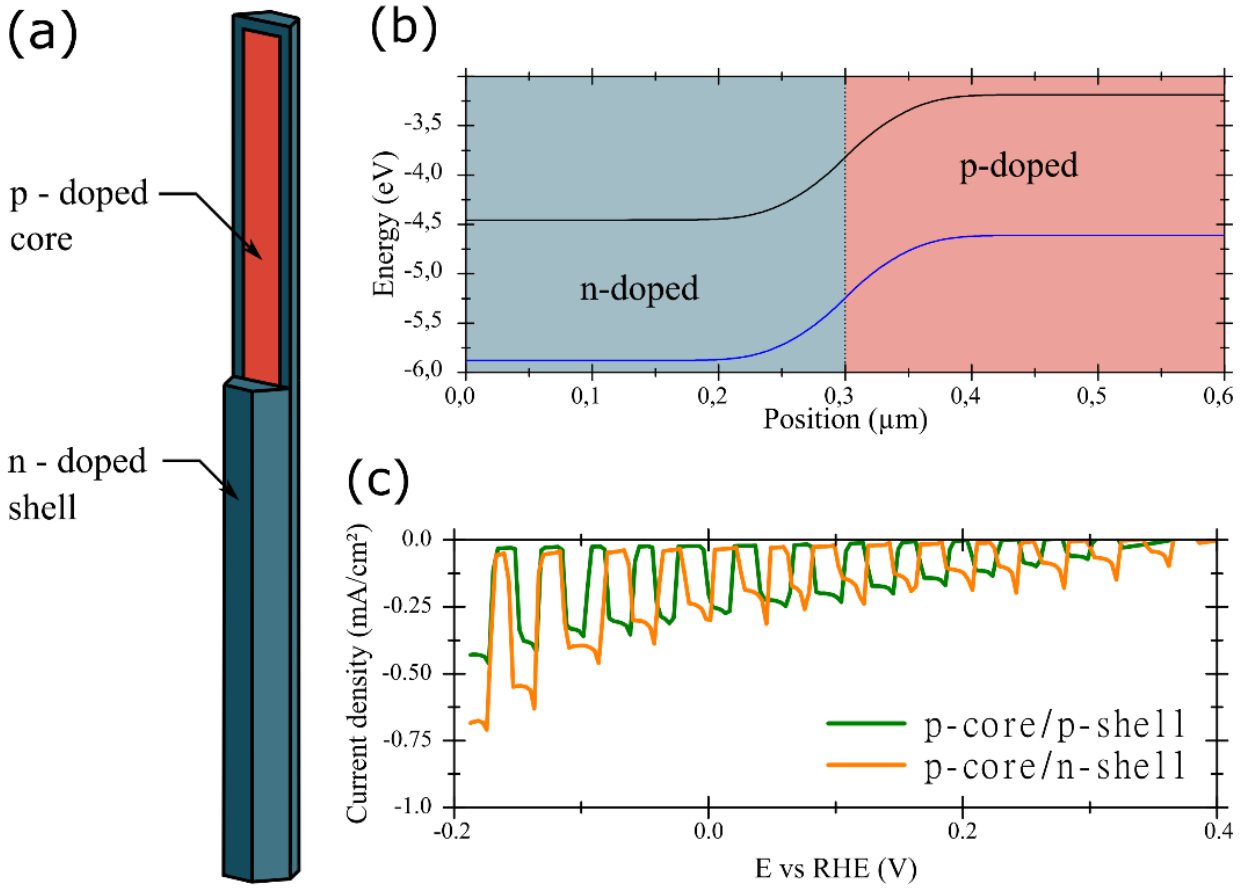


Figure 7.3. (a) Schematic representation of the NW structure, showing the *p*-doped core in orange and the *n*-doped shell in blue. (b) Energy band diagram simulation showing the band bending at the interface of the *n*-doped and *p*-doped GaAs. The conduction and valence bands are represented by the black and blue lines, respectively. (c) LSV measurements performed at 10 mV/s in 0.1 M potassium phosphate buffer (pH 7) under nitrogen, irradiated with chopped light (1 sun, 1.5 AM filter), showing the current densities of the sample 3 in green and of a similar morphology NWs exhibiting a p-n junction in orange.

The fabricated p–n junction creates a bending in the band diagram at the interface of the p–core and the n–shell of the NW, as illustrated by the simulation showed in Figure 7.3.b. Indeed, the bending created by this junction aims to favor the separation of the charges and thus to reduce the rate of their recombination. However, the LSV measurements carried out on two samples with the same sample dimensions, with and without p–n junction, only reveal a slight increase of the photocurrent density from about 0.3 mA/cm² to 0.4 mA/cm² at 0 V *vs* RHE, as shown in Figure 7.3.c.

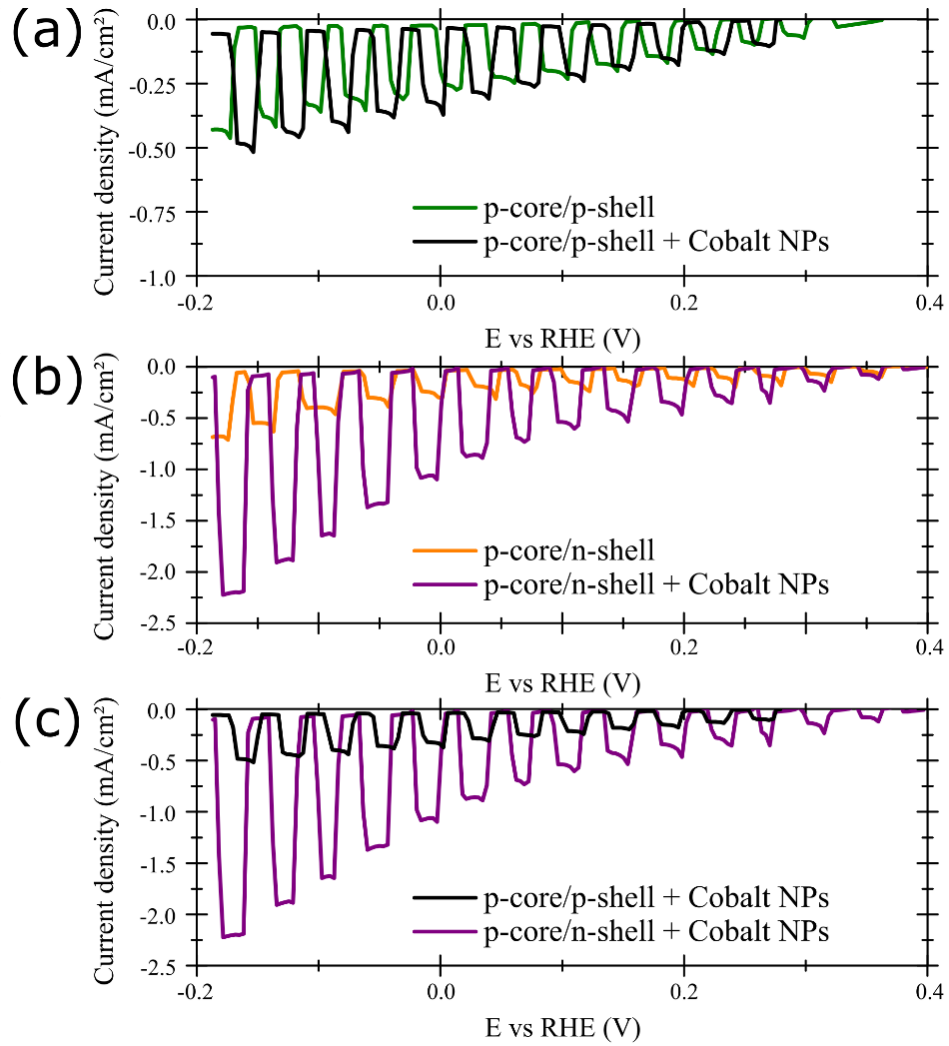


Figure 7.4. (a)-(c) LSV measurements performed at 10 mV/s in 0.1 M potassium phosphate buffer (pH 7) under nitrogen, irradiated with chopped light (1 sun, 1.5 AM filter), showing the current density of samples with and without p-n junction in orange and green, respectively. The purple and black lines respectively correspond to the current density obtained for samples with and without p-n junction, after the deposition of cobalt-catalyst nanoparticles. The Co nanoparticles were deposited at-0.65 V vs Ag/AgCl during 45 minutes, under 1 sun illumination.

Nevertheless, a significant increase of the photocurrent density was obtained after the integration of a HER catalyst on the NW based electrode. Indeed, while Pt is the most commonly used catalyst for the hydrogen reaction, Co nanoparticles (NPs), a more abundant and cost-effective metal in comparison with Pt, were deposited on the NW sample. Despite its excellent efficiency as a catalyst for the reaction, Pt is an extremely rare and expensive material. The Co NPs were deposited on both samples with and without p–n junctions following the procedure developed by V. Artero's team[20]. A comparison of the photocurrents obtained is provided in Figure 7.4 and shows an increase from 0.4 mA/cm² to about 1.2 mA/cm² at 0 V *vs* RHE for the sample with the p–n junction, as shown in Figure 7.4.b and Figure 7.4.c. However, the efficiency enhancement is drastically smaller for the sample presenting a p–core and a p–shell, with an increase from 0.3 mA/cm² to about 0.4 mA/cm² at 0 V *vs* RHE (Figure 7.4.a and Figure 7.4.c). The Co NPs

catalyst were assumed to act as traps for the electrons, thus guaranteeing an optimal use of the charges generated by GaAs NWs[21] and overcoming the recombination issues induced by the slow reaction with the electrolyte.

### 7.2.4 Ageing and $TiO_2$ protection of the GaAs nanowires

Despite their promising efficiency for the photocatalytic water splitting, III-V semiconductors suffer from instability when placed in an aqueous electrolyte. To overcome this critical problem, a thin layer of titanium oxide ($TiO_2$) is commonly deposited all around the materials and acts as a layer of protection[10,22,23]. A $TiO_2$ protective shell of about 10 nm thick was deposited on the p–core / n–shell NWs by atomic layer deposition (ALD), ensuring the homogeneous deposition of the oxide[22,24–26].

The LSV measurements realized on the *p*–core / *n*–shell samples with and without the protective shell are shown in Figure 7.5.a. A slight decrease of the photocurrent density from about 1.2 mA/cm² down to 0.8 mA/cm² at 0 V vs RHE was observed for the $TiO_2$ protected sample, due to the thickness of the oxide layer covering the NWs, while an opposite observation were done by F. Cui *et al.* with an increase of the photocurrent density in presence of the $TiO_2$ protective shell[10]. Nonetheless, the stability of the photocathode over time was enhanced. Indeed, Figure 7.5.b shows a chronoamperometric (CA) measurement performed under a 1 sun illumination over half a day. During the first minutes the sample without the oxide shell, represented with the purple line, showed a higher photocurrent density compared to the sample with the protective shell (dark blue line). However, in less than one hour the photocurrent of the sample without the $TiO_2$ shell dropped to ~0.2 mA/cm², and stabilized at about 0.06 mA/cm² after ~6 hours. On the opposite, the photocurrent of the sample with the oxide shell dropped quickly to ~0.4 mA/cm² then stabilized after ~ 6 hours at around 0.15 mA/cm². Despite the lower photocurrent measured after 12 hours, the unshelled NWs still present a similar stability as the NWs covered by the $TiO_2$ protective shell, unlike the results recently presented by H. Liu's group[10] that observed a fast degradation of the unprotected NWs.

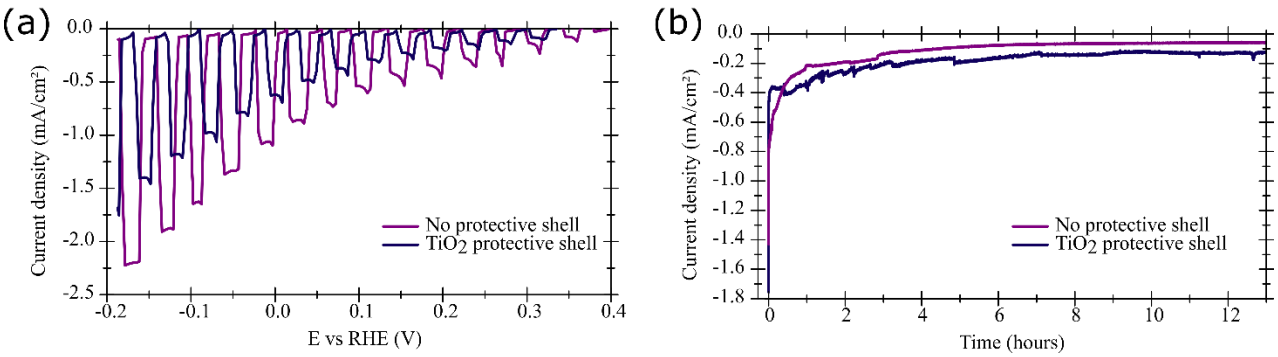


Figure 7.5. (a) LSV measurements performed at 10 mV/s in 0.1 M potassium phosphate buffer (pH 7) under nitrogen, irradiated with chopped-light (1 sun, 1.5 AM filter), showing the current density of the p-n junction samples, with and without the 10-nm thick $TiO_2$ protective shell. (b) Chronoamperometric measurements recorded for 13 hours at 10 mV/s in 0.1 M potassium phosphate buffer (pH 7) under 1 sun illumination for sample with and without $TiO_2$ protective shell. The dark blue and purple lines on (a) and (b) correspond to the sample with and without the $TiO_2$ protective shell, respectively.

## 7.3 The GaP photoanode

Similarly to the previous section, GaP NWs were tested as photoanodes for the OER. The NWs were grown by MBE using the gold-catalyzed growth method on a *n*-doped Si(111) substrate and were protected by the deposition of a 15-nm thick $TiO_2$ layer. A STEM-ADF image of a typical GaP NW obtained through a focused ion beam (FIB) lamella extracted from the electrode is displayed in Figure 7.6.a. The heavier GaP core and lighter $TiO_2$ shell are identified within the ADF image. They were evidenced within EELS elemental maps of the Ga-$L_{23}$ and Ti-$L_{23}$ edges, using the spectrum imaging technique, as illustrated in Figure 7.6.b (Ga core) and Figure 7.6.c (Ti shell). The particular bottleneck shape visible at the top of the NWs is here related to the gold-assisted technique. Indeed, a small gold NP is still present at the tip of the objects, leading to a slight axial growth during the radial growth of the NWs. The remaining gold droplet is visible as a small bright dot at the tip of the NW in Figure 7.6.a. The EELS maps confirmed the conformal deposition of the $TiO_2$ all around the NW suggesting no visible leak points.

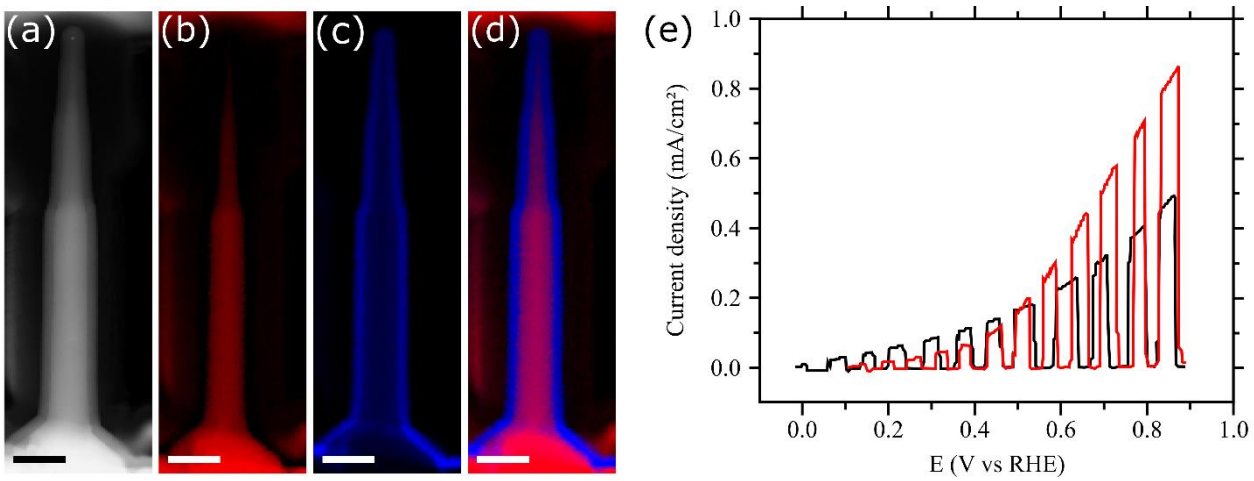


Figure 7.6. (a) STEM-ADF image of a single GaP NW. (b) Ga core, (c) Ti shell and (d) superimposed maps of the Ga core (red) and Ti shell (blue). Scale bars are 100 nm. (e) LSV measurements performed at 10 mV/s in 0.1 M potassium hydroxide (pH 13) under argon, irradiated with chopped-light (1 sun, 1.5 AM filter). Red and black lines represent the GaP NW sample with and without Ni NPs catalysts, respectively.

Subsequently, the activity of the fabricated photoanode was measured by LSV in an aqueous potassium hydroxide electrolyte (pH13) using the same conditions as for the photocathodes. Figure 7.6.b shows the photocurrent obtained for GaP NWs (black line), reaching a density of about 0.4 mA/cm² at 0.8 V *vs* RHE. The LSV measurements were stopped at 0.9 V *vs* RHE due to strong degradation of the cell caused by an oxidation peak and to the destruction of the sample. In the same way as the GaAs photocathode, an OER catalyst was used to enhance the efficiency of the electrode. Ni nanoparticles were then deposited on the NWs by photoelectrodeposition, and was confirmed through the dissolution of the sample in nitric acid, revealing a total Ni amount of about 1.8 µg/cm². The addition of such Ni catalysts led to an increase of the photocurrent density up to about 0.9 mA/cm² at 0.8 V vs RHE.

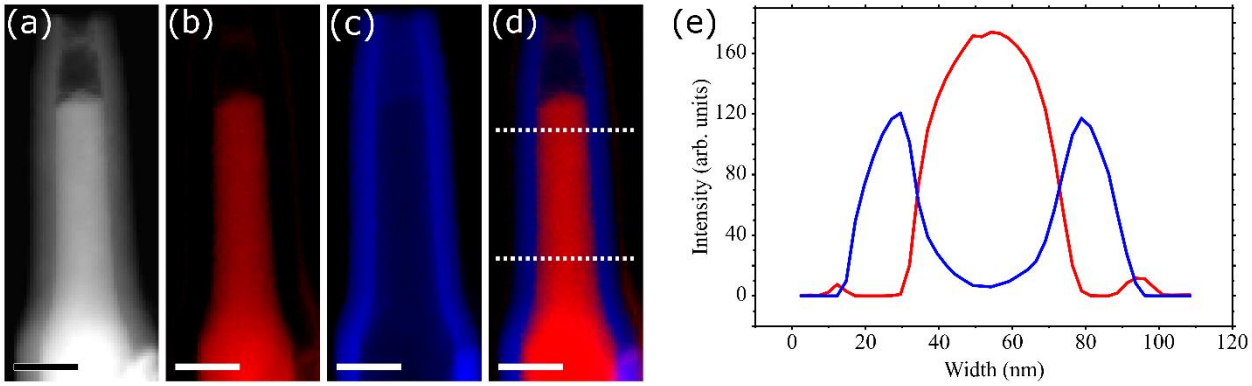


Figure 7.7. (a) STEM-ADF image of the tip of a GaP NW after 2 hours of OER performed at 0.8 V vs RHE. (b) Ga core, (c) Ti shell and (d) superimposed maps of the Ga core (red) and Ti shell (blue). Scale bars are 50 nm. (e) Intensity profile of the tip of the NW representing the Ga and Ti profiles in red and blue lines, respectively.

Further investigations were performed in order to study the $TiO_2$ shell and its capacity to protect the NWs from the degradation due to the electrolyte and to the reactions. Indeed, due to the nature of the OER forming $O_2$ bubbles at the surface of the NWs, a strong degradation is expected (stronger compared to the HER of the photocathode). The integrity of the NW core and of the $TiO_2$ shell was then studied using STEM-EELS, as shown in Figure 7.7. The deterioration of the $TiO_2$ protecting the tip of the NWs was systematically observed after the OER, as shown in Figure 7.7.a,c,d, creating a hole in the protective shell at the top of the NW. This weak point led to the consumption of the GaP core of the NWs as illustrated in Figure 7.7.b and Figure 7.7.d. Subsequently, the presence of a thin layer of Ga was observed outside the $TiO_2$ shell. Indeed, the intensity profile of the Ga EELS maps in Figure 7.7.e reveals a peak on each side of the NW.

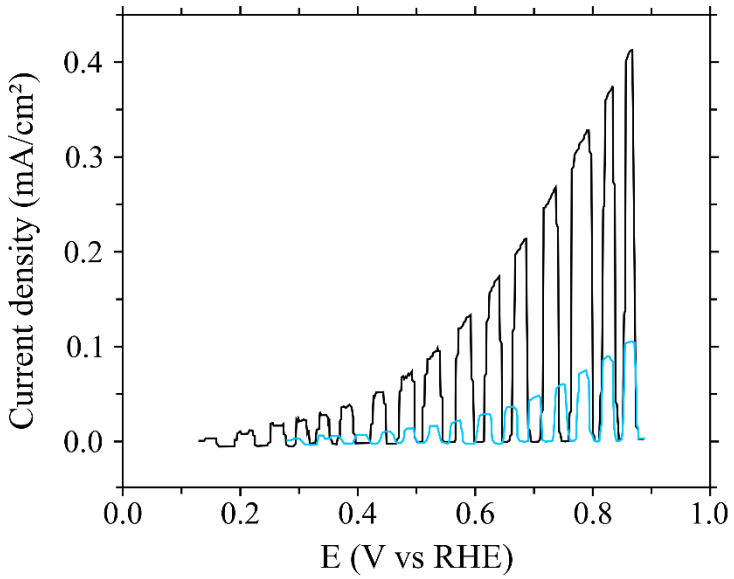


Figure 7.8. LSV measurements performed at 10 mV/s in 0.1 M potassium hydroxide (pH 13) under argon, irradiated with chopped-light (1 sun, 1.5 AM filter). Light blue and black lines correspond to the measurements performed with and without the UV filter, respectively.

In order to validate the contribution of the GaP semiconductor as a source of the photocurrent produced by the electrode, LSV measurements were performed using a 400 nm cutoff filter, which ensures the transmission of light with a wavelength $\lambda < 400$ nm. Figure 7.8 shows a drastic decrease of the photocurrent of about 75 % in the presence of the UV filter (light blue line), revealing that the main contribution provided by the electrode came from the $TiO_2$ thin layer. This major contribution of the $TiO_2$ over the GaP could be explained by an inefficient transfer of the electron from the electrolyte to the material. Therefore, XPS analyses were performed to determine the band alignment between the GaP core and the $TiO_2$ shell, using the TEMPO beamline at the SOLEIL synchrotron, in collaboration with the SPEC (CEA-Saclay). Three distinct samples (a bulk GaP substrate acting as a reference sample, an undoped GaP / $TiO_2$ NWs and an n–doped GaP / $TiO_2$ NWs) were studied.

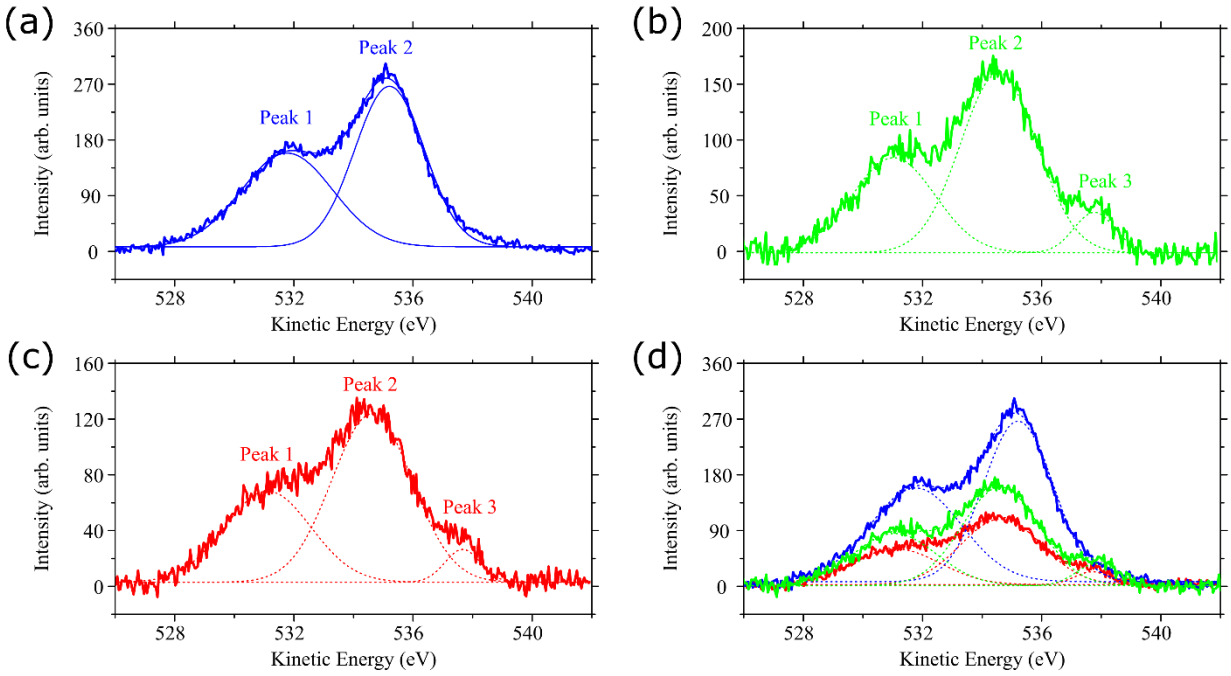


Figure 7.9. XPS spectra of Ga 3p obtained at a photon energy of 645 eV corresponding to (a) bulk GaP, (b) undoped GaP NWs, (c) n–doped GaP NWs. (d) Superposition of the three spectra. Doted lines correspond to the fits of the different peaks.

Firstly, the Ga 3p edge (Figure 7.9) was investigated at a photon energy of 645 eV, showing three broad peaks at 535.21 eV, 534.62 eV and 534.64 eV, corresponding to the bulk GaP, undoped GaP / $TiO_2$ NWs and n–doped GaP / $TiO_2$ NWs, respectively. The energy positions of the valence bands were then measured (Figure 7.10) for the three samples at the same photon energy of 645 eV, leading to values of 639.18 eV, 637.04 eV and 636.94 for the bulk GaP, the undoped GaP / $TiO_2$ NWs and the n–doped GaP / $TiO_2$ NWs, respectively.

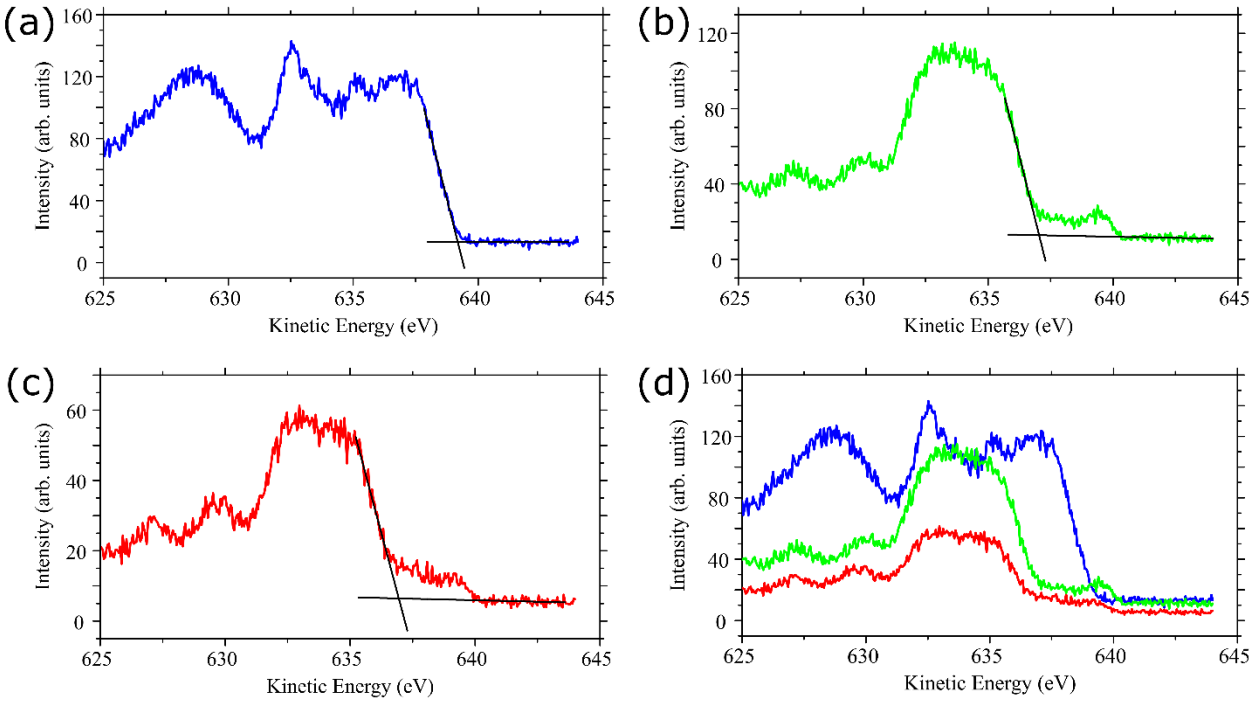


Figure 7.10. XPS spectra of the valence band obtained at a photon energy of 645 eV corresponding to (a) bulk GaP, (b) undoped GaP NWs, (c) n–doped GaP NWs. (d) Superposition of the three spectra. Black lines correspond to the fits used to determine the value of the energy position of the valence band maximum.

Secondly, the samples were investigated at a photon energy of 1300 eV to access the Ga $2p_{3/2}$ and Ga 3p states. The Ga $2p_{3/2}$ (Figure 7.11.a-c) measured at 177.70 eV, 177.59 eV and 177.40 eV for the bulk GaP, the undoped GaP / $TiO_2$ NWs and the n–doped GaP / $TiO_2$ NWs respectively, can be used as references to determine the alignment of the valence bands measured. The second peak of the Ga 3p was then measured at 1191.09 eV, 1190.53 eV and 1191.09 eV for the bulk GaP, the undoped GaP / $TiO_2$ NWs and the n–doped GaP / $TiO_2$ NWs respectively, as shown in Figure 7.11.d-f.

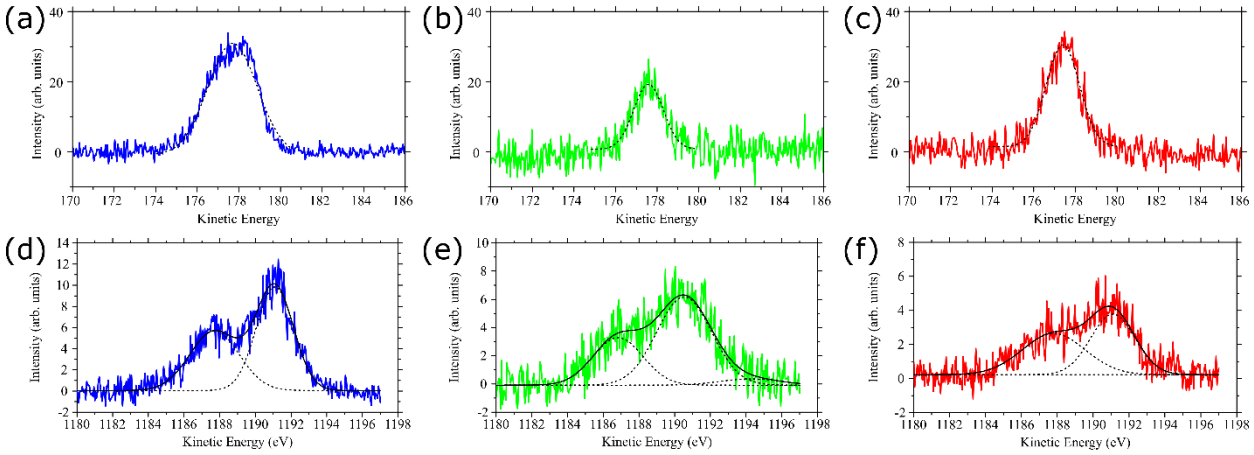


Figure 7.11. XPS spectra obtained at a photon energy of 1300 eV, corresponding to (a)-(c) Ga $2p_{3/2}$ and (d)-(f) Ga 3p. Blue, green and red lines correspond to the bulk GaP, undoped GaP NWs and n–doped GaP NWs. Doted lines correspond to the fits used to identify the different peaks. Black lines correspond to the sum of the fits.

Subsequently, the difference between the Ga 2p level and the valence band can be determined using the following equation:

$$\Delta\left(K_{Ga\ 2p} - K_{VB}\right) = \Delta(K_{Ga\ 2p} - K_{Ga\ 3p})_{@1300\ eV} + \Delta(K_{Ga\ 3p} - K_{VB})_{@645\ eV}, \qquad (7.1)$$

where $K_{Ga\ 2p}$, $K_{Ga\ 3p}$ and $K_{VB}$ correspond to the kinetic energy of the Ga 2p peak, Ga 3p peak and valence band, respectively. The difference $\Delta(K_{Ga\ 2p}\text{-}K_{VB})$ was determined equal to 1117.36 eV, 1115.43 eV and 1115.99 eV for the bulk GaP, the undoped GaP / $TiO_2$ NWs and the n–doped GaP / $TiO_2$ NWs, respectively. The two NW samples covered by a 5-10 nm thick layer of $TiO_2$ led to the measurement of the $TiO_2$ valence band, while the bulk sample gives a value for the valence band of the GaP. Taking Ga 2p as reference, it is possible to determine the position of the $TiO_2$ valence band with respect to the GaP valence band. Thus, the $TiO_2$ valence band was estimated 1.37 eV below the valence band of the GaP, as illustrated in Figure 7.12. The band gap of GaP and $TiO_2$ being respectively equal to 2.25 eV and 3.20 eV, they induce a hypothetical conduction of $TiO_2$ located about 0.42 eV below the conduction band of GaP.

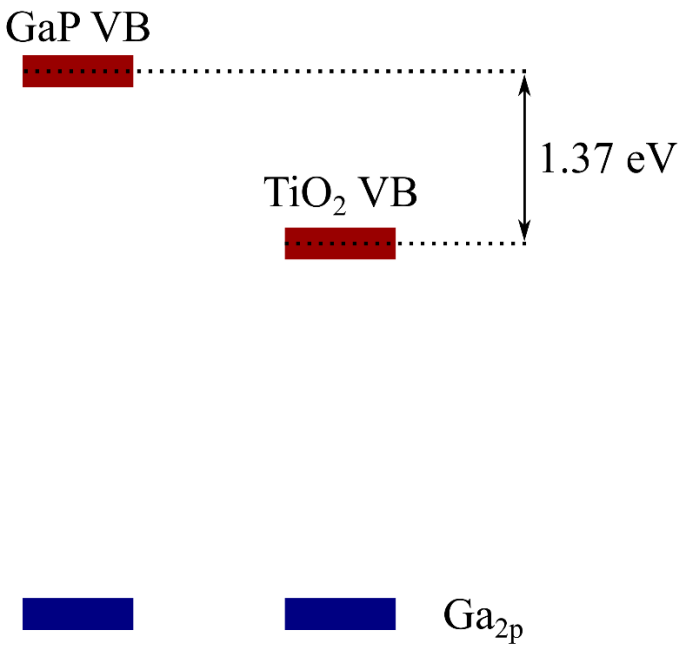


Figure 7.12. Simplified schematic representation of the valence band position (red) of the GaP (left side) and of the $TiO_2$ (right side). The Ga 2p level (blue) was used as a reference.

The difference obtained between the valence bands of GaP and $TiO_2$ appears as a major problem for the OER occurring at the photoanode interface. Indeed, as discussed in the chapter 1, the electrons travel from the electrolyte to the electrode. The valence band difference observed here then appears as detrimental for the reaction, blocking the electron-hole pairs at the GaP / $TiO_2$ interface. Therefore, these results could explain the major contribution of $TiO_2$ compared to GaP. In order to improve the cell efficiency, several paths arise. Indeed, the doping level of the GaP can be investigated as well as the $TiO_2$ protective shell.

## 7.4 Conclusion

In this chapter, GaAs- and GaP-based NW photoelectrodes were studied and their efficiency was investigated. The relevance of the NW geometry compared to the thin film was shown as the result of a strong reduction of the light reflected by the electrode. The photocatalytic activity of the GaAs photocathode was then enhanced as a result of the combination of a radial p–n junction in the NW and the deposition of Co NPs, acting as catalysts for the HER. These optimizations led to an increase of the photocurrent density up to 1.2 mA/cm² at 0 V vs RHE. Furthermore, the stability of the photocatalytic activity over time was improved with the deposition of a 10-nm thick layer of $TiO_2$ protective shell around the NWs, which increases the efficiency of the cells by a factor 3 after 13 hours. On the other hand, GaP (core) / $TiO_2$ (shell) NW-based photoanodes showed a major contribution of the $TiO_2$ shell over the GaP core, mainly due to an inappropriate band alignment. Further investigations have to be performed on the GaP doping level and on the oxide used to protect the GaP photoanodes to better understand the contribution of each compounds. Furthermore, the stability of the protective shell of this electrode still has to be improved to avoid any degradation of the NW core.

## 7.5 References

1. Lewis, N. S. Developing a scalable artificial photosynthesis technology through nanomaterials by design. *Nature Nanotech* **11**, 1010–1019 (2016).

2. Hwang, Y. J., Boukai, A. & Yang, P. High Density n-Si/n-TiO $_2$ Core/Shell Nanowire Arrays with Enhanced Photoactivity. *Nano Lett.* **9**, 410–415 (2009).

3. Liu, S., Han, C., Tang, Z.-R. & Xu, Y.-J. Heterostructured semiconductor nanowire arrays for artificial photosynthesis. *Mater. Horiz.* **3**, 270–282 (2016).

4. Wang, S., Liu, G. & Wang, L. Crystal Facet Engineering of Photoelectrodes for Photoelectrochemical Water Splitting. *Chem. Rev.* **119**, 5192–5247 (2019).

5. Deng, J. *et al.* Nanowire Photoelectrochemistry. *Chem. Rev.* **119**, 9221–9259 (2019).

6. Chen, H. *et al.* 3D InGaN nanowire arrays on oblique pyramid-textured Si (311) for light trapping and solar water splitting enhancement. *Nano Energy* **83**, 105768 (2021).

7. Han, S. *et al.* Highly Efficient Photoelectrochemical Water Splitting Using GaN-Nanowire Photoanode with Tungsten Sulfides. *ACS Appl. Mater. Interfaces* **12**, 58028–58037 (2020).

8. Standing, A. *et al.* Efficient water reduction with gallium phosphide nanowires. *Nat Commun* **6**, 7824 (2015).

9. Kornienko, N. *et al.* Growth and Photoelectrochemical Energy Conversion of Wurtzite Indium Phosphide Nanowire Arrays. *ACS Nano* **10**, 5525–5535 (2016).

10. Cui, F. *et al.* Robust Protection of III–V Nanowires in Water Splitting by a Thin Compact TiO $_2$ Layer. *ACS Appl. Mater. Interfaces* **13**, 30950–30958 (2021).

11. Xie, G. *et al.* GaP/GaPN core/shell nanowire array on silicon for enhanced photoelectrochemical hydrogen production. *Chinese Journal of Catalysis* **41**, 2–8 (2020).

12. Vanka, S. *et al.* InGaN/Si Double-Junction Photocathode for Unassisted Solar Water Splitting. *ACS Energy Lett.* **5**, 3741–3751 (2020).

13. Kibria, M. G. *et al.* Tuning the surface Fermi level on p-type gallium nitride nanowires for efficient overall water splitting. *Nat Commun* **5**, 3825 (2014).

14. Kamimura, J., Bogdanoff, P., Ramsteiner, M., Geelhaar, L. & Riechert, H. Photoelectrochemical properties of InN nanowire photoelectrodes for solar water splitting. *Semicond. Sci. Technol.* **31**, 074001 (2016).

15. Varadhan, P. *et al.* Surface Passivation of GaN Nanowires for Enhanced Photoelectrochemical Water-Splitting. *Nano Lett.* **17**, 1520–1528 (2017).

16. Fountaine, K. T., Cheng, W.-H., Bukowsky, C. R. & Atwater, H. A. Near-Unity Unselective Absorption in Sparse InP Nanowire Arrays. *ACS Photonics* **3**, 1826–1832 (2016).

17. Gao, L. *et al.* High-Efficiency InP-Based Photocathode for Hydrogen Production by Interface Energetics Design and Photon Management. *Adv. Funct. Mater.* **26**, 679–686 (2016).

18. Gerthsen, D., Ponce, F. A., Anderson, G. B. & Chung, H. F. Lattice Mismatch Effects in Gaas Epitaxy on Si and GaP. *MRS Proc.* **122**, 21 (1988).

19. Lee, M. H. *et al.* p-Type InP Nanopillar Photocathodes for Efficient Solar-Driven Hydrogen Production. *Angew. Chem. Int. Ed.* **51**, 10760–10764 (2012).

20. Cobo, S. *et al.* A Janus cobalt-based catalytic material for electro-splitting of water. *Nature Mater* **11**, 802–807 (2012).

21. Yang, J., Wang, D., Han, H. & Li, C. Roles of Cocatalysts in Photocatalysis and Photoelectrocatalysis. *Acc. Chem. Res.* **46**, 1900–1909 (2013).

22. Chandrasekaran, S. *et al.* A robust ALD-protected silicon-based hybrid photoelectrode for hydrogen evolution under aqueous conditions. *Chem. Sci.* **10**, 4469–4475 (2019).

23. Toupin, J. *et al.* Engineering n-p junction for photo-electrochemical hydrogen production. *Phys. Chem. Chem. Phys.* **19**, 30675–30682 (2017).

24. Gu, J. *et al.* Water reduction by a p-GaInP2 photoelectrode stabilized by an amorphous TiO2 coating and a molecular cobalt catalyst. *Nature Mater* **15**, 456–460 (2016).

25. Hu, S. *et al.* Amorphous $TiO_2$ coatings stabilize Si, GaAs, and GaP photoanodes for efficient water oxidation. *Science* **344**, 1005–1009 (2014).

26. Moehl, T., Suh, J., Sévery, L., Wick-Joliat, R. & Tilley, S. D. Investigation of (Leaky) ALD $TiO_2$ Protection Layers for Water-Splitting Photoelectrodes. *ACS Appl. Mater. Interfaces* **9**, 43614–43622 (2017).

# Conclusion and perspectives

III-V semiconductor NWs attracted many interests in the last decades due to their remarkable properties, combining the advantageous properties of the III-V semiconductor with the one-dimensionality of the NW geometry. Hence, their integration for optical or energy harvesting applications appears as really promising. This thesis was focused on the growth of self-assisted GaAs NWs by MBE, from the control of their crystalline structure to their integration as PEC for light-driven water splitting.

Firstly, the growth mechanisms implied in the NW synthesis were studied. The morphology and the structure of GaAs NWs were investigated and optimized with an adjustment of the different growth parameters used during their fabrication. A very homogeneous morphology of the NWs has been obtained on 2 inches-large Si(111) wafers. Furthermore, the possibility to track the formation of the ZB and WZ structures through the indexation of the diffraction spots observed in a RHEED pattern recorded *in situ* during the growth allowed a real-time control of the ZB and WZ phases' formation. Numerical simulations were then used to provide a set of growth parameters intended to reach a WZ phase growth regime, which allows the synthesis of a 1.3 µm long WZ-pure segment in self-assisted VLS growth mode. These results were supported by high-resolution HAADF-STEM and DF-TEM imaging as well as *in situ* RHEED analysis. The ability to control on demand the MBE growth of the cubic or hexagonal structure in self-assisted GaAs NWs appears possible.

The growth of WZ-pure segment of self-assisted GaAs NWs could possibly be achieved by constantly tuning the As flux over time, controlled through a RHEED feedback loop in order to compensate the variation of the amount of Ga supplied to the droplet during the transient regime. This possibility to grow WZ-pure self-assisted GaAs NWs is of major interest to tune the properties of III – V nanostructures on demand, and particularly to fabricate semiconducting heterostructures with novel functionalities, such as the growth of hexagonal SiGe with direct bandgap by MBE.

The lattice parameters of the ZB and WZ structure of an individual GaAs NW were measured using synchrotron X-ray nano-diffraction, leading to the observation of a mismatch of about 0.04% with respect to the theoretical lattice parameter of the ZB structure, as well as a mismatch of 0.05% and 0.1% for the *a* and *c* parameters of the WZ structure. These results, combined with high-resolution HAADF-STEM and DF-TEM analysis, revealed the existence of strain at the nanoscale, which was strongly correlated with the alternation of the cubic and hexagonal phases along the NW long axis, and was responsible of the slight lattice parameters variations. The existence of torsion and bending was also further observed and seemed

correlated with the presence of the ZB and WZ structures. However, the influence of the crystal structure on torsion and bending remains an open question. Furthermore, a possible correlation between the bending/torsion and the light emission of the NW could be investigated by cathodoluminescence.

Finally, GaAs and GaP NWs were used as photocathodes and photoanodes for the water reduction and oxidation. The NWs were protected by a 10-nm thick $TiO_2$ passivation shell, deposited by ALD. The influence of the morphology of the NWs as well as the impact of a $TiO_2$ protective shell were investigated by PEC characterizations. In this work, the relevance of the NW geometry over the thin film material has been showed, improving the light absorption ($400\ nm < \lambda < 870\ nm$) of the electrodes by a factor 4. On the one hand, co-catalyst Co nanoparticles were electrodeposited on the GaAs NW photocathode to improve the water reduction reaction. Photocurrent of about 1.0-1.5 $mA/cm^2$ were obtained, revealing the high potential of such photoelectrodes. However, the effect of the $TiO_2$ passivation layer is still to be investigated as well as the influence of the NW doping on the photoactivity. On the other hand, co-catalyst Ni nanoparticles were used to enhance the water oxidation reaction of the GaP (core)/$TiO_2$ (shell) photoanodes, reaching a photocurrent of about 0.8-1.0 $mA/cm^2$. However, PEC characterizations performed on the GaP (core)/$TiO_2$ (shell) photoanodes revealed a major contribution of the 10-nm thick $TiO_2$ shell over the GaP core on the PEC activity, and were explained by an alignment of the valence bands detrimental to the charge transport through the semiconductor / oxide interface.

Investigations still could be performed to determine the GaP core doping level and the oxide thickness used to protect the NWs and evaluate their influence on the generated photocurrent. These parameters could be optimized in order to maximize the impact of the GaP core on the PEC activity while reducing the contribution of the $TiO_2$ shell on the generated photocurrent. The impact of the WZ and ZB crystal structure on the PEC activity was not studied in this work, nonetheless, the photocurrent generated by pure-ZB and pure-WZ GaAs NWs-based photocathodes could be investigated to highlight a potential role of the crystal phase on the photocatalytic activity. Furthermore, the photocathode and photoanode activity using different NW components, such as InP, could be compared to identify the ideal elements for PEC. Finally, a tandem PEC combining the optimized GaAs photocathode and GaP photoanode could be studied to monitor the complete water splitting process of such NW based PEC.

# Résumé

Parallèlement au développement des sociétés industrialisées, l'utilisation comme sources d'énergie primaires de combustibles fossiles tels que le gaz naturel, le pétrole et le charbon a considérablement augmenté au cours du siècle dernier, menant à des rejets toujours plus importants de $CO_2$, reconnu partiellement comme un des acteurs majeurs de la crise de réchauffement climatique actuelle. De par la nature évidente des problèmes environnementaux causés par l'utilisation généralisée de sources d'énergie non renouvelables, l'exploration de stratégies alternatives pour fournir de l'énergie verte à grande échelle est devenue un enjeu crucial pour la communauté scientifique. Parmi toutes ces alternatives, des efforts intenses ont été portés au développement de cellules photoelectrochimique (PEC) capable de produire une photosynthèse neutre en carbone, en utilisant l'énergie solaire pour convertir d'abondantes ressources comme $H_2O$ ou $CO_2$ en $H_2$, $CH_3OH$ ou $NH_3$, composés stables et pouvant être stockés et distribués facilement.

Les dispositifs photoelectrochimique pour la photoélectrolyse de l'eau sont typiquement composés d'une anode où les molécules d'eau sont oxydées en $O_2$ et $H^+$ et par une cathode dans laquelle les protons sont réduit en $H_2$. La première photoanode efficace pour la photoélectrolyse de l'eau a été rapportée en 1972 par A. Fujishima et K. Honda. La photoanode de $TiO_2$ proposée dans ces travaux a ensuite été à l'origine d'intenses efforts de la part de la communauté scientifique afin d'améliorer l'efficacité des processus solaire-hydrogène. Cependant, le bandgap de ce matériau est une limite pour l'efficacité des dispositifs à base de $TiO_2$. En effet, le gap de 3,2 eV du $TiO_2$ restreint la lumière absorbée à une faible fraction du spectre solaire. Afin de contourner cette difficulté, les semiconducteurs III-V comme le GaAs ou le GaP ont émergé comme composés avantageux, grâce à leurs gaps plus faibles, permettant ainsi une plus large collection du spectre solaire. De ce fait, les semiconducteurs III-V apparaissent comme des matériaux prometteurs pour la fabrication de photoelectrodes pour les applications d'énergie solaire.

Dans ce contexte, les photoelectrodes à base de nanofils (NFs) sont particulièrement attractives pour augmenter l'efficacité des PEC pour la photoélectrolyse de l'eau. En effet, les réactions d'oxydation et de réduction ayant lieu à l'interface entre l'électrode et l'électrolyte, maximiser la surface efficace en contact avec le milieu aqueux grâce au rapport d'aspect important de la géométrie NF peut permettre une augmentation de l'efficacité de la cellule. De plus, une des caractéristiques importantes de la géométrie NF est sa capacité à fortement réduire les pertes d'absorption. Une partie des photons entrants peut être réfléchie

sur la surface du semiconducteur, ou transmise à travers le semiconducteur, empêchant ainsi la séparation des charges. Se concentrer sur certains types de semiconducteurs (comme le GaN, GaAs, GaP ou InP) permet ainsi de fournir une réduction drastique de la lumière réfléchie. Les réseaux aléatoires de NFs crûs sur un substrat peuvent permettre de réduire les pertes d'absorption.

Malgré leur potentiel élevé pour la photoélectrolyse de l'eau, les photoelectrodes à base de NFs de semiconducteur III-V souffrent d'une forte corrosion en milieu aqueux, empêchant toute utilisation. Cependant, des couches d'oxyde métallique de passivation ont été développées sous forme de coquilles minces de protection pour les semiconducteurs, compatibles avec le transfert de charge, chimiquement stables dans un liquide et transparentes à la lumière visible. De nombreux oxydes apparaissent comme des candidats efficaces pour éviter la dégradation des semiconducteurs III-V, tels que $TiO_2$, $NiO_x$, $CoO_x$, $SnO_2$, $Al_2O_3$, $BaTiO_3$, ou le $SrTiO_3$.

L'intégration de ces NFs de semiconducteurs III-V sur substrats de silicium a été réalisée en 2004 par le groupe de L. Samuelson, ouvrant la voie à des dispositifs nouveaux et complexes. Ainsi, l'intégration de semiconducteurs à gap directe, tels que le GaAs, dans l'industrie déjà bien établie du silicium offre de nombreuses opportunités pour les applications optoélectroniques telles que les cellules solaires à haut rendement. De plus, l'intégration de semiconducteurs III-V peut apporter de nouvelles propriétés d'émission de lumière à des matériaux tels que Si ou Ge. En effet, E.M.T. Fadaly *et al.* ont récemment démontré qu'un tel matériau pouvait être utilisé comme point de départ pour la fabrication d'alliages SiGe hexagonal à gap direct.

De nos jours, les semiconducteurs III-V sont utilisés comme matériaux de base pour de nombreux appareils électroniques et optoélectroniques commerciaux et haut de gamme. L'intégration de matériaux à haute efficacité tels que le GaAs sur du silicium à faible coût apparaît alors comme une étape importante pour les applications, et a été intensivement étudiée au cours des dernières décennies. Cependant, la présence d'une différence de maille dans le réseau cristallin entre le silicium et les semiconducteurs III-V représente un facteur limitant pour la fabrication et les performances de telles hétérostructures. En effet, une réduction des propriétés de luminescence des couches 2D de GaAs sur silicium, induite par une différence de maille de 4,1%, a été mise en évidence par Gerthsen *et al*. en 1988.

Pour surmonter les conséquences de l'inadéquation du réseau, Mårtensson *et al*. ont d'abord rapporté la fabrication de NFs de semiconducteurs III-V par croissance épitaxiale sur des substrats de silicium, montrant une luminescence à température ambiante. En effet, l'échelle nanométrique et la géométrie de ces nano-objets induisent une relaxation élastique à leur surface, minimisant ainsi les contraintes dues au désalignement du réseau. Les NFs III-V peuvent être synthétisés par épitaxie par jets moléculaires (EJM ou MBE pour molecular beam epitaxy). La méthode la plus couramment utilisée est le mécanisme vapeur-liquide-solide (VLS). Les sources d'éléments utilisées pour la croissance sont chauffées dans des cellules d'effusion rattachées au réacteur MBE, produisant chacune un flux de vapeur.

Les NFs de semiconducteurs III-V peuvent présenter deux structures cristallines différentes : une phase cubique blende de zinc (ZB) et une phase hexagonale wurtzite (WZ). Depuis l'établissement du modèle

fondamental proposé par l'équipe de F. Glas en 2007 sur la nucléation des phases ZB et WZ se produisant lors de la croissance de NFs de GaAs catalysés Au, et la première croissance de NFs de GaAs ZB auto-assistée réalisée par l'équipe de A. Fontcuberta i Morral en 2008, un large intérêt a été porté sur l'observation en temps réel de la nucléation de ces phases afin de contrôler leur formation dans les NFs, qui présentent différentes propriétés électroniques, optiques, mécaniques, thermoélectriques et piézoélectriques. Ces propriétés physiques, modulables grâce au contrôle des structures cristallines ZB et WZ des NFs de GaAs auto-assistés, ouvrent ainsi la voie au développement d'une large gamme de NFs hétérostructurés sans éléments tiers, ce qui est particulièrement attractif pour la fabrication de dispositifs.

Cependant, aussi prometteurs que puissent être ces matériaux, les rapports actuels font face à une limitation de la mise à niveau des prototypes vers les dispositifs appliqués. En effet, les NFs de GaAs en phase WZ sont obtenus en utilisant la croissance catalysée par de l'or, incompatible avec l'industrie du silicium. La croissance auto-assistée apparaît alors comme la solution optimale pour pallier à la contamination d'or des NFs. Ainsi, des prototypes de réacteurs de croissance ont récemment été utilisés pour mettre en évidence le mécanisme de nucléation des différentes structures cristallines et pour contrôler la phase sur un seul NF de GaAs auto-assisté. La croissance étendue de la structure WZ des NFs de GaAs auto-assistés par MBE n'a cependant été étudiée que dans des études récentes.

Dans notre groupe, nous avons ainsi démontré l'applicabilité du RHEED dans le contrôle des structures cristallines des NFs de GaAs auto-assistés, donnant accès au suivi en temps réel de l'évolution de la phase cristalline au cours de la croissance. Il a été possible d'ajuster les paramètres de croissance, tels que le flux de Ga et As, et de forcer la nucléation de segments WZ hexagonaux.

Le travail rapporté dans ce manuscrit fait partie du projet financé par l'ANR (Agence Nationale de la Recherche) BEEP (Ingénierie d'électrodes à base de nanofils pour la photocatalyse), dont la portée finale est d'intégrer des NFs de semiconducteurs III-V dans des photocathodes et photoanodes combinées au sein d'une cellule tandem pour la photocatalyse de l'eau. Ce projet a impliqué plusieurs laboratoires académiques tels que l'INL (CNRS), MATEIS (CNRS), ICJ (CNRS), ainsi que deux laboratoires du Commissariat à l'énergie atomique et alternative (CEA) SPEC (CEA-Saclay) et LCBM (CEA-Grenoble).

Cette thèse a été consacrée à la croissance et à la caractérisation de NFs de GaAs et GaP crûs par MBE sur des substrats de silicium, utilisés comme PEC pour la photocatalyse de l'eau. Par conséquent, les croissances par MBE en mode VLS de NFs de GaAs auto-assistés et de NFs de GaP catalysés par gouttes d'or ont été étudiées en parallèle. La géométrie et la morphologie de ces objets ont été optimisées en modifiant les paramètres de croissance. De plus, une forte homogénéité de la morphologie des NFs sur un large substrat a été obtenue. L'influence de la géométrie et de la morphologie des NFs sur l'activité des PEC a été étudiée, ainsi que le rôle d'une coquille protectrice de $TiO_2$ déposée par atomic layer deposition (ALD). Des analyses structurales et chimiques ont été réalisées sur les NFs pour étudier le vieillissement et l'impact de la réaction sur les NFs.

Les aspects fondamentaux du mécanisme de croissance de la structure cristalline de tels NFs ont également été étudiés et des caractérisations approfondies ont été réalisées pour comprendre les phénomènes

de croissance et contrôler la nucléation. Par exemple, une partie importante de ce travail a été consacrée au contrôle à la demande de la formation des structures hexagonales ou cubiques, pour concevoir des phases cristallines de NFs de GaAs auto-assistées lors de la croissance VLS. Des analyses structurelles à l'aide d'outils avancés tels que la microscopie électronique en transmission à balayage avec correction d'aberrations et la diffraction par nano-faisceaux issue de rayonnement synchrotron ont été effectuées sur les NFs pour étudier leur phase cristalline ainsi que leur déformation grâce à une haute résolution spatiale.

Le plan de ce manuscrit est le suivant : le fonctionnement des principaux montages expérimentaux utilisés au cours de cette thèse est expliqué au chapitre 2. Les bases et les concepts de la croissance des NFs de GaAs auto-assistés et leurs structures cristallines seront abordés au chapitre 3. Dans les chapitres 4 et 5, mes travaux concernant le contrôle de la croissance de NFs de GaAs auto-assistés à l'aide d'outils de caractérisation *in situ* sont discutés, tandis que le chapitre 6 est consacré à leurs caractérisations *post mortem* avancée. Enfin, la fiabilité d'un tel matériau appliqué à la photocatalyse de l'eau est discutée au chapitre 7.

Les résultats obtenus au cours de ces trois années de travaux expérimentaux sont ainsi rapportés dans cette thèse en 7 chapitres :

**1 Introduction** :

Une présentation détaillée sur l'utilisation des semiconducteurs III-V appliqués à la photocatalyse de l'eau, développant les principes fondamentaux impliqués dans les réactions d'oxydation et de réduction des molécules d'eau. Dans une seconde partie, les bénéfices apportés par la géométrie nanofil sont exposés.

**2 Techniques expérimentales de synthèse et de caractérisation** :

Ce deuxième chapitre est dédié à l'épitaxie par jet moléculaire ainsi qu'aux dispositifs utilisés durant cette thèse. Dans une première partie, le dispositif de croissance MBE y es présenté, ainsi que le système de caractérisation par diffraction des électrons de haute énergie en incidence rasante (RHEED, pour reflective high energy electron diffraction) utilisé pour calibrer les flux d'éléments III et V ainsi qui pour suivre les croissances *in situ*. Dans une seconde partie, les outils utilisés pour caractériser les NFs après croissance sont détaillés, présentant les dispositifs de caractérisation photoelectrochimique, ainsi que les techniques de caractérisations par rayon X. Enfin, les instruments de microscopie utilisés pour la caractérisation des NFs (microscope électronique à balayage et microscope électronique en transmission à balayage) sont présentés dans la fin de ce chapitre.

**3 Croissance épitaxiale par jets moléculaire de nanofils de GaAs** :

Les bases fondamentales de la croissance des NFs de GaAs sur substrat de silicium sont présentées dans ce chapitre. Le mode de croissance VLS utilisé durant cette thèse pour la synthèse des NFs de GaAs est exposé en détail, présentant ainsi l'utilisation d'un catalyseur liquide de Ga pour amorcer la croissance. La présence des structures cristalline cubique (ZB) et hexagonale (WZ) observées dans un NF est également introduite dans ce chapitre, présentant le modèle théorique établie dans la littérature et introduisant ainsi le rôle de l'angle de mouillage du catalyseur. Enfin, l'influence des différents paramètres de croissance, tel

que la température de croissance et les étapes de pré-dépôt, ainsi que l'impact de la thermique du substrat sur l'homogénéité de l'échantillon sont traités dans la deuxième partie de ce chapitre.

**4 Le suivi de la phase cristalline dans la croissance auto-assistée de nanofils de GaAs par RHEED *in situ*** :

Dans ce quatrième chapitre, les travaux expérimentaux effectués durant cette thèse prouvant la fiabilité du système RHEED dans le suivi *in situ* de l'évolution de la phase cristalline des NFs de GaAs pendant la croissance par MBE sont présentés. Ainsi, l'évolution du diagramme de diffraction obtenu durant la croissance a été analysée, révélant la possibilité de déterminer les phases cristallines en cours de croissance grâce au rapport d'intensité entre les spots de diffraction induit par les structures ZB et WZ. Des segments de WZ au sein de NFs en phase ZB ont ainsi été réalisés. La présence des segments souhaités a par la suite été confirmée par microscopie électronique à transmission. Enfin une simulation numérique (réalisée dans notre groupe par A. Danescu) a été utilisée afin de valider les angles de mouillages rapportés dans la littérature, auxquels des changements de phases sont observés.

**5 La croissance d'un segment de WZ pure dans les nanofils auto-assistés de GaAs** :

Les travaux visant à maintenir les conditions de croissance menant à la formation de la phase WZ dans les NFs auto-assistés de GaAs sont discutés dans ce chapitre. La première partie est dédiée à l'explication des simulations numériques (réalisé dans notre groupe par A. Danescu) utilisées pour fournir des paramètres de croissance menant à un maintien de la nucléation de la phase hexagonale pendant la croissance auto-assistée de NFs de GaAs. Dans une seconde partie, il est montré qu'il a été possible d'ajuster les paramètres de croissance, tels que le flux Ga et As, afin de forcer la nucléation des segments hexagonaux. Dans ce chapitre, la croissance de NFs GaAs auto-assistés, conduisant à un segment étendu de WZ pure de 1,3 µm de long est présentée et discutée. Cette croissance a été contrôlée par RHEED *in situ* et appuyée par des simulations numériques, et a fait l'objet d'une publication.

**6 STEM à correction d'aberration combinée à de la nano-diffraction synchrotron pour l'ingénierie de la phase cristalline dans les nanofils de GaAs** :

Dans ce chapitre, nous avons étudié les mécanismes de relaxation et de déformation impliqués dans un NF présentant différentes structures cristallines, en utilisant la haute résolution dans l'espace réciproque de la nano-diffraction synchrotron. Ces caractérisations ont été combinées avec une analyse par microscopie électronique en transmission à balayage et par microscopie électronique à transmission en champs sombre à haute résolution, effectuée sur le même NF individuel, en utilisant les mêmes taches de diffraction que pour la nano-diffraction. Enfin, un modèle d'élasticité linéaire a été utilisé pour simuler la relaxation de la distance inter-réticulaire induite par le changement de phase le long du NF.

**7 Fabrication de photoelectrodes à base de nanofils pour les réactions d'oxydation et de réduction de l'eau** :

Ce chapitre est divisé en deux parties distinctes. Tout d'abord, le développement et la caractérisation des photocathodes à base de NFs de GaAs sont discutés, exposant la géométrie avantageuse des NFs en comparaison avec les films minces. L'influence de la morphologie et du dopage est discutée à la fin de cette première partie. Dans un second temps, des études analogues réalisées sur des photoanodes à base de NFs de GaP sont présentées, avec pour objectif final la fabrication d'une cellule tandem regroupant photocathode et photoanode, afin de réaliser la photocatalyse de l'eau complète.

# Abstract

The objectives of this thesis was to grow and characterize GaAs and GaP nanowires (NWs) grown by molecular beam epitaxy (MBE) on silicon substrates used as photoelectrochemical cells (PEC) for light-driven water splitting. The vapor-liquid-solid (VLS) growths of self-assisted GaAs NWs and gold-catalyzed GaP NWs by MBE were studied in parallel. The geometry and the morphology of these objects were optimized by changing the parameters of the growth. Moreover, high homogeneity of the NW morphology on large substrate was achieved. The influence of the geometry and morphology on the PEC activity was investigated, as well as the role of a $TiO_2$ protective shell deposited by atomic layer deposition. Structural and chemical analysis were performed on the NWs to study the aging and the impact of the reaction on the NWs.

The fundamental aspects of the crystal structure growth mechanism of such NWs were also investigated, and in depth characterizations were performed to understand the growth phenomena and to control the nucleation. Hence, a significant part of this thesis was devoted to control the formation of the hexagonal or cubic structures on demand, to engineer self-assisted GaAs NWs crystal phases during the VLS growth. Structural analyses using advanced tools such as aberration-corrected scanning transmission electron microscopy and synchrotron radiation nano-beam diffraction were performed on NWs to study their crystal phase as well as their strain at high spatial resolution.



**Key words:** Self-assisted GaAs nanowires, polytypism, water-splitting, photoelectrochemical cell, core/shell nanowires



# Résumé

Les objectifs de cette thèse étaient de développer et de caractériser des nanofils (NFs) GaAs et GaP développés par épitaxie par jet moléculaire (EJM) sur des substrats de silicium utilisés comme cellules photoélectrochimiques (CPE) pour la séparation de l'eau par la lumière. Les croissances vapeur-liquide-solide (VLS) des NFs de GaAs auto-assistés et des NFs de GaP catalysés par l'or par EJM ont été étudiées en parallèle. La géométrie et la morphologie de ces objets ont été optimisées en changeant les paramètres de la croissance. De plus, une grande homogénéité de la morphologie des NFs sur un grand substrat a été obtenue. L'influence de la géométrie et de la morphologie sur l'activité des CPE a été étudiée, ainsi que le rôle d'une coquille de $TiO_2$ de protection déposée par dépôt de couche atomique. Des analyses structurales et chimiques ont été réalisées pour étudier le vieillissement et l'impact de la réaction sur les NFs.

Les aspects fondamentaux du mécanisme de croissance de la structure cristalline de tels NFs ont également été étudiés et des caractérisations approfondies ont été réalisées pour comprendre les phénomènes de croissance et contrôler la nucléation. Par conséquent, une partie importante de cette thèse a été consacrée au contrôle de la formation des structures hexagonales ou cubiques à la demande lors de la croissance VLS des NFs de GaAs auto-assistées. Des analyses structurelles à l'aide d'outils avancés tels que la microscopie électronique à transmission à balayage avec correction d'aberrations et la diffraction de nano-faisceaux issue de rayonnement synchrotron ont été effectuées sur les NW pour étudier leur phase cristalline ainsi que leur déformation grâce à une haute résolution spatiale.



**Mots-clés :** Nanofils de GaAs auto-assistés, polytypisme, photocatalyse de l'eau, cellule photoelectrochimique, nanofils cœur/coquille